DUNE Far Detector Task Force Preliminary Report

September 30, 2016

Contents

1 Introduction

The DUNE Far Detector Task Force was formed in September 2015 and charged to:

- develop a full far detector (FD) simulation and reconstruction chain (Section 2);
- produce detector optimization studies, for example, 3 mm vs 5 mm wire pitch, wire angle and the efficiency of the light readout system for different configurations (Section 6);
- produce a first update the DUNE long-baseline physics sensitivity studies using full simulation and event reconstruction (Section 5);
- develop the simulation and reconstruction for SNB and nucleon decay physics (Section 4);
- take into account both reference (single-phase TPC) and alternate (dual-phase TPC) FD designs in the studies (Section 3).

These goals were motivated by the status of DUNE's simulation and reconstruction tools and physics sensitivity studies at the time the task force was formed. The long-baseline oscillation sensitivity studies up until that time had been performed with GLoBES [1, 2]. GLoBES

is not a full Monte Carlo (MC) simulation, but takes neutrino beam fluxes, cross sections, and detector-response parameterization as inputs to produce simulated energy spectra that are used in a fit for oscillation parameters. Simulations of neutrino beam events in DUNE had been performed, but reconstruction tools were still in the very early stage of development. Tools to simulate nucleon decay, atmospheric neutrinos, and supernova neutrinos had not yet been incorporated into the software. A full simulation and reconstruction chain is needed to study how changes in detector design affect the final sensitivities. The goal of this task force is to develop simulation and reconstruction tools necessary to study the effect of detector design on physics performance. We have selected a few particular detector design questions to address, but we expect detector optimization studies to continue after the conclusion of the task force.

This document represents the preliminary report on the findings of the Far Detector Task Force. A final report will be presented in March 2017.

2 Simulation and Reconstruction Chain

In this section, we summarize the latest development of the simulation and reconstruction tools that are being used by the DUNE 35t prototype, far detector, and protoDUNE. The adoption of the common framework LArSoft [3] by several liquid argon time projection chamber (LArTPC) experiments helps people exchange ideas and test algorithms on real data. This work has been focused on single-phase TPCs. The progress on implementing dual-phase TPC simulation and reconstruction in LArSoft will be described in Section 3.

2.1 Monte Carlo Challenge

We produce large samples of Monte Carlo events (Monte Carlo Challenge - MCC) on a regular basis. The purpose is to test the latest simulation and reconstruction chain as well as the grid job submission tools and sam/tape interfaces and provide standard samples for various physics working groups to analyze. All the MCC samples are produced using the batch tool larbatch [4]. MCC1.0 was produced in January 2015 with three 35t samples. We include far detector and protoDUNE samples in later MCCs and incorporate more sophisticated detector simulation and reconstruction software. The latest MC production MCC6.0, which was produced in May 2016, consists of 50 samples using the 35t, far detector and protoDUNE single-phase geometries. MCC6.0 was produced using LArSoft v05_09_01. The locations of the samples can be found in Ref [5].

In MCC6.0, we simulated 3 types of beam neutrinos (unoscillated ν_μ's, fully-oscillated ν_e's and fully-oscillated ν_τ's), atmospheric neutrinos, supernova neutrinos, proton decays and cosmogenic events in the far detector. In order to save processing time, all the far detector samples except the cosmogenics sample were simulated using a smaller version of the full 10 kt far detector geometry. This geometry is 13.9 m long, 12 m high and 13.3 m wide, which consists of 12 APAs and 24 TPCs. In the default configuration, the TPC wire spacing is 5 mm, the wire angle is 36° and the neutrino beam is parallel to the wire planes. We also generated special samples where the wire spacing is 3 mm or the wire angle is 45° or the neutrino beam is perpendicular to the wire planes for the detector optimization studies.

2.2 Simulation Chain

Each sample is simulated in 3 steps: generation (gen), GEANT4 tracking (g4) and digitization (detsim). The first step is unique for each sample while the second and the third steps are common for all samples.

2.2.1 Generation

Both the beam neutrinos and atmospheric neutrinos were simulated using GENIE v2_10_6. The beam neutrinos were simulated using the reference flux. We simulated unoscillated samples in both the neutrino and antineutrino modes. We also simulated fully oscillated samples where we convert all ν_μ's in the beam to either ν_e's or ν_τ's.

The atmospheric neutrinos were simulated using the Bartol flux for the Soudan site [6]. There is a plan to use the Honda flux for the Homestake site [7] when the GENIE flux interface is updated.

The proton decay events were simulated using standalone GENIE v2_10_6 after a bug in the kaon final state interaction simulation was identified and fixed. Only the decay mode $p \rightarrow \bar{\nu} + K^+$ was simulated. The output files were converted to the LArSoft format for further processing.

The supernova neutrino events were generated using custom code wrapped in a LArSoft module (also described in Section 4.1.3). This code simulates charged-current ν_e-^{40}Ar interactions. For each electron neutrino it calculates probabilities to produce a ^{40}K nucleus in different excited states (using a model from [8]), randomly selects one, and (with energy levels from [9]) produces several de-excitation γs and an electron carrying the remaining energy. All particles are produced isotropically, there is no delay between the electron and corresponding de-excitation γs (in this model the ^{40}K nucleus de-excites instantaneously) and they share a vertex, which is simulated with equal probability anywhere in the active volume. The primary neutrino energy distribution used in these samples is the cross-section-weighted energy spectrum obtained from SNOwGLoBES [10] (using the "GKVM" flux [11]). The supernova neutrino generator also allows to simulate a Poisson-distributed random number of neutrino interactions per event. These samples were simulated with, on average, 2 or 20 neutrinos. In addition, one of the samples was generated with 1.01 Bq/kg of ^{39}Ar background.

Cosmogenic events at depth were generated using MUSIC (Muon Simulation Code) [12] and MUSUN (Muon Simulations Underground) [13]. MUSIC first propagates a set of muons through a medium with user-specified parameters (e.g. density, elemental composition), given initial parameters of energy, position and direction cosines. It takes muons of energies ranging from 10^2 to 10^7 GeV and stores their energy distribution at between 100 and 15000 meters-water-equivalent (mwe). MUSUN then generates a muon energy spectrum and angular distribution appropriate for an underground location using the output of MUSIC as well as details about the local surface profile. This information is used to calculate the total amount of rock a muon would traverse through given its inclination. The particles passed to GEANT4 are then sampled on the surface of a box surrounding the detector and containing a few meters of rock. The average energy of the muons simulated is 284 GeV.

2.2.2 GEANT4 Tracking

The truth particles generated in the event generator step are passed to a GEANT4 v4_10_1_p03 based detector simulation. In this step, each primary particle from the generator and its decay or interaction daughter particles are tracked when they traverse liquid argon. The energy deposition is converted to ionization electrons and scintillation photons. Some electrons are recombined with the positive ions [14, 15] while the rest of the electrons are drifted towards the wire planes. The number of electrons is further reduced due to the existence of impurities in the liquid argon, which is commonly parameterized as the electron lifetime. The default electron lifetime is 3 ms in the simulation. The longitudinal diffusion smears the arrival time of the electrons at the wires and the transverse diffusion smears the electron location among neighboring wires. More details regarding the recent measurements of diffusion coefficients can be found in Ref. [16, 17].

When ionization is calculated, the amount of scintillation light is also calculated. The response of the photon detectors is simulated using a 'photon library,' a pre-generated table giving the likelihood that photons produced within a voxel in the detector volume will reach any of the photon detectors. The photon library is generated using GEANT4's photon transport simulation, including 66 cm scattering length, 20 m attenuation length, and reflections off of the interior surface detectors. The library also incorporates the response vs. location of the photon detectors, capturing the attenuation between the initial conversion location of the photon and the SiPMs.

2.2.3 Digitization

The electrons on each wire are converted into raw wire signal (ADC vs Time) by convolution with the field response and electronics response. The field response on each wire plane is simulated with Garfield [18] while the ASIC electronics response was simulated with the BNL SPICE [19] simulation. Currently, the signal on each wire can only be produced from the ionization electrons going through the wire. The improvement upon this approximation is ongoing. This in particular is important for the induction wire planes, where the induction signal depends on the local ionization charge distribution [20]. For most samples, the ASIC gain was set to 14 mV/fC and the shaping time was set to 2 μs. For the samples generated with 3 mm wire spacing, the ASIC gain was set to 25 mV/fC. The noise level was set to 2.5 ADC RMS. In the current simulation, the electronic noise is assumed to be white, which is a uniform distribution in the frequency domain. The implementation of a more realistic electronics noise model is ongoing. Figures 1 and 2 show the expected electronics shaping functions and simulated field response for the closest wire, respectively.

The photon detector electronics simulation separately generates waveforms for each channel (SiPM) of a photon detector that has been hit by photons. Every photon that has been detected appears as a single photoelectron pulse (with the shape taken from [21]) on a randomly selected channel (belonging to the photon detector in which the photon was registered). Then dark noise (with the rate of 10 Hz) and line noise (Gaussian noise with the RMS of 2.6 ADC counts) are added. Each photon (or a dark-noise pulse) has a probability of appearing as 2 photoelectrons on a waveform (the cross-talk probability is 16.5 %). The final step of the digitization process is recording only fragments of the full simulated waveforms

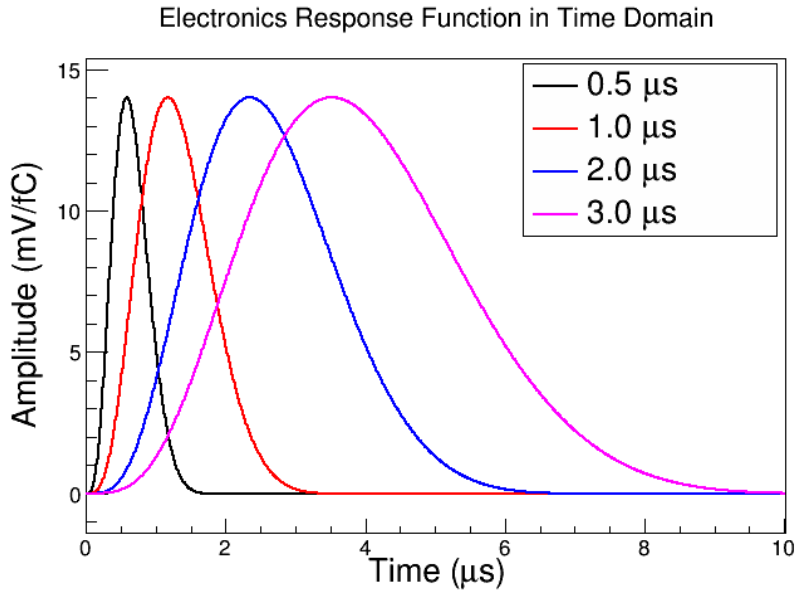

Figure 1: ASIC's electronics shaping functions are shown for four shaping time settings at 14 mV/fC gain.

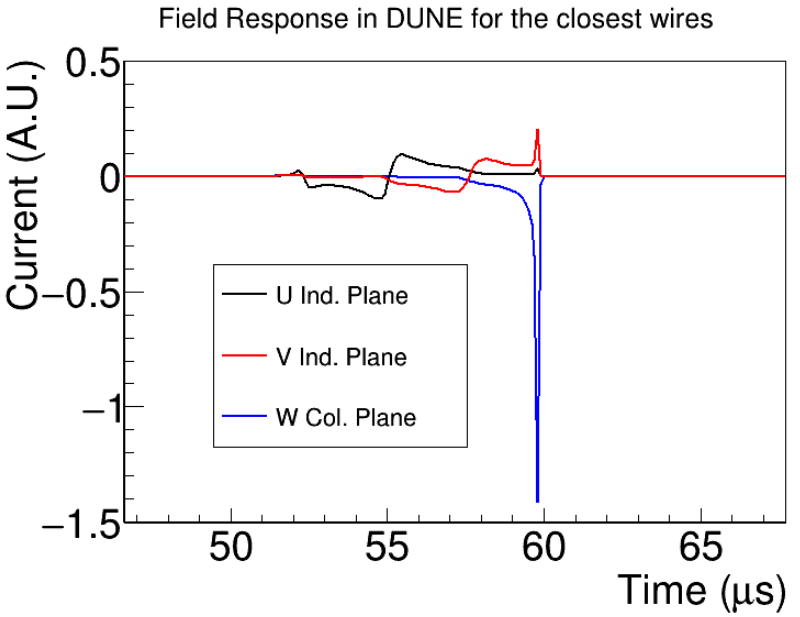

Figure 2: Field response simulated with Garfield program is shown for two induction and one collection planes.

that have a signal in them. That is accomplished by passing the waveforms through a hit finder described in Section 2.3.11 and storing parts of the waveforms corresponding to the hits found.

2.3 Reconstruction Chain

In this section, we describe various reconstruction algorithms used to reconstruct events in the far detector TPC.

2.3.1 Signal Processing

The raw data are in the format of ADC counts as a function of TPC ticks on each wire. The signal can have a unipolar shape if it is on a collection wire or a bipolar shape if it is on an induction wire. The first step in the reconstruction is to convert the raw signal from each wire to a standard shape such as a Gaussian shape. This is achieved by passing the raw data through a calibrated deconvolution algorithm. In real detectors, excess noises may exist and need to be properly dealt with through a dedicated noise filter [22]. There is currently no such complication in the simulation.

The deconvolution technique was introduced to LArTPC signal processing by Bruce Baller in the context of ArgoNeuT data analysis. The goal of the deconvolution [23] is to "remove" the impact of field and electronics responses from the measured signal to recover the number of ionized electrons. This technique has the advantages of being robust and fast and is an essential step in the overall drifted-charge profiling process.

Deconvolution is a mathematical technique to extract a *real signal* $S(t)$ from a *measured signal* $M(t_0)$. The measured signal is modeled as a convolution integral over the real signal $S(t)$ and a given detector *response function* $R(t, t_0)$ which gives the instantaneous portion of the measured signal at some time t_0 due to an element of real signal at time t:

$$M(t_0) = \int_{-\infty}^{\infty} R(t, t_0) \cdot S(t) \cdot dt. \tag{1}$$

If the detector response function only depends on the relative time difference between t and t_0,

$$R(t, t_0) \equiv R(t - t_0), \tag{2}$$

we can solve the above equation by doing a Fourier transformation on both sides of the equation:

$$M(\omega) = R(\omega) \cdot S(\omega), \tag{3}$$

where ω is the frequency. In this case, we can derive the signal in the frequency domain by taking the ratio of measured signal and the given response function:

$$S(\omega) = \frac{M(\omega)}{R(\omega)}. \tag{4}$$

The real signal in the time domain can then be obtained by applying the inverse Fourier transformation from the frequency domain.

The response function $R(\omega)$ does not address contributions to the measured signal which are due to real world sources of electrical *noise* from thermal and unwanted transmitting sources or the approximation in the digitization. Such contributions to $M(\omega)$ will not be removed by the deconvolution. Worse, because the response function becomes small at low frequencies for the induction planes and at high frequencies for all planes, the noise components in these frequencies will be enhanced by the deconvolution.

To address the issue of noise, a *filter function* $F(\omega)$ is introduced. Its purpose is to attenuate the problematic noise. The addition of this function can be considered an augmentation to the response function. The two functions are kept distinct for clarity in the notation here. Equation (4) is then updated to become

$$S(\omega) = \frac{M(\omega)}{R(\omega)} \cdot F(\omega). \tag{5}$$

With a suitable noise filtering model an improved estimator for the signal $S(t)$ in the time domain can then be found by applying an inverse Fourier transform to $S(\omega)$. Essentially, the deconvolution replaces the real field and electronics response function with an effective software filter response function. The advantage of this procedure is more pronounced on the induction plane where the irregular bipolar field response function is replaced by a regular uni-polar response function through the inclusion of the software filter.

Since the current simulation only simulates induced current on the closest wire to the ionization electrons, the aforementioned 1-D deconvolution technique is sufficient to process the TPC signal. However, the induction signal in a real detector is expected to strongly depend on the local ionization charge distribution. In this case, the 1-D deconvolution is not enough to recover the number of ionization electrons. A 2-D deconvolution technique, which includes both the time and wire dimensions, has been developed in MicroBooNE to deal with the complicated induction plane signal. Details can be found in Ref. [20].

2.3.2 Gaussian Hit Finder

GausHitFinder is a hit-finding algorithm that works starting from deconvolved signals on wires and defining areas above threshold as "pulses". Once a pulse is found, an 'n' Gaussian hypothesis is applied where 'n' is defined by the number of peaks initially identified within the pulse. Based on the outcome of the fit an object known as a "hit" is formed and stored in the event.

2.3.3 Disambiguation

The induction plane wires are wrapped in the DUNE TPC design in order to save cost on electronics and minimize dead region between APAs. The consequence is that multiple induction wire segments will be read out by the same electronic channel. We need to determine which wire segment corresponds to the energy deposited by the particle in the TPC. This process is called disambiguation.

The current disambiguation algorithm was developed for the 35t geometry. It relies on the fact that the collection plane wires are not wrapped and the wire angles are slightly different for the two inductions views (44.3° vs 45.7°) so that any three wires from the three

planes read out by the same three channels will never cross twice. The algorithm uses gaushit as input. All the collection plane hits are unambiguous. Each induction plane hit has one channel ID and several possible wire IDs corresponding to various wire segments read out by the same channel. We need to determine which wire ID is the correct one for each induction plane hit.

The disambiguation algorithm first loops over all collection plane hits. For each collection plane hit, it loops over all induction plane hits and looks for one hit on each of the two induction planes that are in time with the collection plane hit. Once the triplet of hits is found (one on each plane with a common time), the algorithm checks all possible wire IDs and looks for three wires that intersect. Once one and only one intersection is identified, the two induction wire IDs are assigned to the two induction plane hits and the ambiguity is resolved. Finally the algorithm loops over all unresolved induction plane hits. For each hit, it loops over all possible wire segments for that channel and chooses the wire segment that is closest to a resolved induction hit as the correct wire segment.

The same disambiguation algorithm also works for the far detector and protoDUNE.

2.3.4 Line Cluster

The intent of the Line Cluster algorithm is to construct two-dimensional line-like clusters using local information. The algorithm was originally known as Cluster Crawler. The "Crawler" name is derived from the similarity of this technique to "gliders" in 2D cellular automata. The concept is to construct a short line-like "seed" cluster of proximate hits in an area of low hit density where hit proximity is a good indication that the hits are indeed associated with each other. Additional nearby hits are attached to the leading edge of the cluster if they are similar to the hits already attached to it. The conditions are that the impact parameter between a prospective hit and the cluster projection is similar to those previously added and the hit charge is similar as well. These conditions are moderated to include high charge hits that are produced by large dE/dx fluctuations and the rapid increase in dE/dx at the end of stopping tracks while rejecting large charge hits from δ-rays. Seed clusters are formed at one end of the hit collection so that crawling in only one direction is sufficient. Line Cluster uses disambiguated gaushits as input and produces a new set of refined hits. More details on the Line Cluster algorithm can be found in Ref [24].

2.3.5 Blurred Cluster

The Blurred Cluster reconstruction method aims to construct two-dimensional shower-like clusters from deposits left in the detector by showers. It specializes in shower reconstruction, especially in the separation of nearby showers in the reconstruction of, e.g., π^0 decay. The algorithm first applies a weighted 2D Gaussian smearing to the hit map in order to introduce 'fake hits' and distribute the charge deposited in the detector more realistically. This proceeds by convolution of a Gaussian kernel, uniquely applied for each hit given information such as rough directionality of the showering particles and the width of the reconstructed hits in time in order to introduce the most accurate blurring possible. Clustering follows by grouping neighboring hits within the blurred region before removing any artificial hits and forming output clusters from the remaining hit collections. BlurredCluster uses disam-

biguated gaushit as input and the output clusters are in turn used as input to the EMShower algorithm (see Sec. 2.3.8). More details and discussion are available in Ref [25].

2.3.6 Pandora

The Pandora Software Development Kit [26] was created to address the problem of identifying energy deposits from individual particles in fine-granularity detectors. It promotes the idea of a multi-algorithm approach to solving pattern-recognition problems. In this approach, the input building-blocks (Hits) describing the pattern-recognition problem are considered by large numbers of decoupled algorithms. Each algorithm targets a specific event topology and controls operations such as collecting Hits together in Clusters, merging or splitting Clusters, or collecting Clusters in order to build Particles. The output from the chain of over 70 algorithms is a hierarchy of reconstructed 3D Particles, each with an identified particle type, vertex and direction.

2.3.7 Projection Matching Algorithm

Projection Matching Algorithm (PMA) was primarily developed as a technique of 3D reconstruction of individual particle trajectories (trajectory fit) Ref [27]. PMA was designed to address a challenging issue of transformation from a set of independently reconstructed 2D projections of objects into a 3D representation. Reconstructed 3D objects are also providing basic physics quantities like particle directions and dE/dx evolution along the trajectories. PMA uses as its input the output from 2D pattern recognition: clusters of hits. For the purposes of the DUNE reconstruction chain the Line Cluster algorithm (2.3.4) is used as input to PMA; however the use of hit clusters prepared with other algorithms may be configured as well. As a result of 2D pattern recognition, particles may be broken in 2D projections into several clusters, fractions of particles may be missing in individual projections and clusters obtained from complementary projections are not guaranteed to cover corresponding sections of trajectories. Such behavior is expected since ambiguous configurations of trajectories can be resolved only if the information from multiple 2D projections is used. Searching for the best matching combinations of clusters from all 2D projections was introduced with PMA implementation in the LArSoft framework. The algorithm attempts also to correct assignments of hits to clusters using properties of 3D reconstructed objects. In this sense PMA is also a pattern recognition algorithm.

The PMA underlying idea is to build and optimize objects in 3D space (formed as polygonal lines with iteratively increased number of segments) by minimizing the cost function calculated simultaneously in all available 2D projections. The cost function consists of 2D distance of hits to the optimized object 2D projections, penalty of tracks curvature, and 3D distance of various feature points to the optimized object (used e.g. to improve performance for tracks with isochronous orientation). The track can be reconstructed using clusters from two projections while the distance of hits to the track projection in the third plane is used to validate correct association of clusters. This method is used to score 3D track candidates in the three-plane TPC configurations, like single-phase DUNE and MicroBooNE detectors and prototypes. Clusters from all planes are used in this scenario in the fine tuning of the selected candidates. In the two-plane configurations (dual-phase TPC detectors, single-phase

LArIAT and ArgoNeut detectors) the track candidates are scored by the value of cost function, which is significantly increased if the trajectory fit is being optimized to spuriously associated clusters (this is also a second-level criterion for the three-plane configurations if the validation method shows no significant difference for track candidates).

The approach of constructing entire objects in 3D allows us to avoid the requirement of finding associations between 2D planes on the level of individual hits. Such associations are especially problematic if several hits on a single trajectory can be found with a similar drift time value, or, if due to a low signal (or any other reason) hits are missed in one of projections. Unambiguous 3D position is calculated for each 2D hit, independently from other hits in the trajectory. Such 3D positions are more accurate than found with the "standard" calculation of a single 3D point using multiple 2D hits matched by drift time values, leading to the more accurate dE/dx estimation. It also allows us to build 3D objects using the detector data from 2D planes directly, without an intermediate step of 3D points calculation which are subsequently used to obtain the final trajectory fit. Another advantage of the approach is the capability of estimating the direction of small, few-hit tracks, or estimating the 3D PC axis of shower-like objects.

Several features were developed in LArSoft's PMA implementation in order to address detector-specific issues like stitching the particle fragments found in different TPC's or an option for performing disambiguation at the 3D reconstruction stage. Since algorithms existing within the LArSoft framework or interfaced to it (see Sec. 2.3.6) can provide pattern reconstruction results which include the particle hierarchy description, the mode of applying PMA in order to calculate solely the trajectory fits was developed. In this mode the collections of clusters forming particles are taken from the "upstream" algorithm and also associations of hits to clusters are not changed.

Recent developments of PMA rely on the same principal ideas and allow us to build and optimize complex structures of 3D objects, i.e. multiple particle trajectories interconnected with interaction vertices. With such an approach it is possible to employ in the vertex position reconstruction the local information from several tracks simultaneously, leading also to an improved fit of each individual trajectory. The track-vertex structure is constructed after the individual trajectories are found and stitched across TPCs. Vertex candidates are found as regions of intersection of two or more tracks (including regions found beyond the track endpoints), with the threshold on the allowed region size. Tracks shorter than nn cm are treated separately; they can be associated to vertex candidates found using long tracks in the first pass of the algorithm or used to create vertex candidates in the second pass. Candidates are scored by the number of intersecting tracks, and if this number is equal for two candidates the maximum angle between intersecting tracks is used to select candidates and create a better defined vertex. The entire track-vertex structure with the newly created vertex is re-optimized using PMA principles in order to accommodate additional information in the trajectory fits. Since the new vertices may connect structures that already contain vertices, a set of rules for splitting and flipping tracks was developed to ensure that the resulting structure is always tree-like (i.e. does not contain loops). The resulting structure is described as a particle hierarchy using data products available in LArSoft.

Two important reconstruction features are currently under development in LArSoft's PMA implementation. The first is the integration of PMA input with the recognition of shower-like 2D objects (electromagnetic showers, electron tracks) and track-like objects

(hadron and muon tracks). Such recognition is a prerequisite of obtaining robust 3D tracking with PMA, since different fitting strategies should be applied to track and shower objects. The second feature under development is the detection of kinks and decay points missed at the 2D pattern recognition level. First attempts were made with the search for outliers in the distribution of angles in the trajectory fit. It was found that the dependence on the track orientation in 2D projection needs to be taken into account; also a potential integration with an algorithm based on 2D ADC image analysis will be explored.

2.3.8 EMShower

The EMShower reconstruction algorithm aims to find final 3D showers and all associated properties. It is intentionally high-level by design and relies heavily on previous reconstruction, specifically BlurredCluster (Sec. 2.3.5) and PMA (Sec. 2.3.7). The reconstruction proceeds in two general steps: first, the shower objects, including all associated hits in each of the views, are found; second, the properties of these showers, such as start point, direction, energy and initial dE/dx, are determined by multiple pattern recognition and calorimetric reconstruction algorithms.

The shower objects are created by simply matching the previously found, well-formed, shower-like clusters (provided by BlurredCluster) between the different views to form 3D objects with associated hits in each plane. This is achieved by associating hits between the 2D shower-like clusters and 3D tracks (provided by, e.g., PMA) in order to pull together clusters from different planes into one object. These shower hits are then analyzed by various successive algorithms in order to find relevant properties before the output shower objects are constructed for later use.

Further details and discussion can be found in Ref [28].

2.3.9 Calorimetric Energy Reconstruction and Particle Identification

As charged particles traverse a liquid argon volume, they deposit energy through ionization and scintillation. It is important to measure the energy deposition as it provides information on particle energy and species. The algorithm for reconstructing the ionization energy in LArSoft is optimized for line-like tracks and is being extended to more complicated event topology such as showers. The algorithm takes all the hits associated with a reconstructed track. For each hit, the hit area or amplitude, in ADC counts, is converted to the charge Q_{det}, in units of fC, on the wire using an ADC to fC conversion factor that was determined by muons or test stand measurements. To account for the charge loss along the drift due to impurities, a first correction is applied to Q_{det} to get the free charge after recombination $Q_{free} = Q_{det}/e^{-t/\tau_e}$, where t is the electron drift time for the hit and τ_e is the electron lifetime measured by the muons or purity monitors. The charge Q_{free} is divided by the track pitch dx, which is defined as wire spacing divided by the cosine of the angle between the track direction and the direction normal to the wire direction in the wire plane, to get the dQ_{free}/dx for the hit. Finally, to account for charge loss due to recombination, also known as "charge quenching", a second correction is applied to convert dQ_{free}/dx to dE/dx based on the modified Box's model [14] or the Birks's model[15]. The total energy deposition from

the track is obtained by summing the dE/dx from each hit: $\sum_{i}^{all\ hits} (dE/dx)_i \cdot dx_i$.

If the incident particle stops in the LArTPC active volume, the energy loss, dE/dx, as a function of the residual range (R), the path length to the end point of the track, is used as a powerful method for particle identification. There are two methods in LArSoft to determine particle species using calorimetric information. The first method calculates four χ^2 values for each track by comparing measured dE/dx versus R points to the proton, charged kaon, charged pion and muon hypotheses and identifies the track as the particle that gives the smallest χ^2 value. The second method calculates the quantity $PIDA =< A_i >=< (dE/dx)_i R_i^{0.42} >$ [14], which is defined to be the average of $A_i = (dE/dx)_i R_i^{0.42}$ over all track points where the residual range R_i is less than 30 cm. The particle species can be determined by making a selection on the $PIDA$ value.

2.3.10 WireCell

WireCell [29], which adopts a very different approach from the aforementioned algorithms, is a new reconstruction method under development. Instead of directly doing pattern recognition on each of the 2D views (drift time vs. wire number), the first step of the WireCell reconstruction is to perform 3D imaging with time, geometry, and charge information. The definition of "Hit" is based on signal strength after charge extraction in a 2 μs time slice. The usage of time information means that hits from different wire planes at different time slices cannot be associated. The usage of geometry information means that hits from wires that are not crossing each other cannot be associated together. The usage of charge information means that the hits from different wire planes with different signal strengths are unlikely to be associated together. The usage of the charge information is quite unique for a LArTPC, as each of the wire planes in principle detects the same amount of the ionization electrons. Figure 3 shows the performance of the WireCell 3D imaging. The large blue blob reflects the ambiguities due to wire readout for a track traveling parallel to the wire plane. (The 3D web-based display can be found at `http://www.phy.bnl.gov/wire-cell/bee/set/6/event/20/`.) In this case, a group of wires from each wire plane is fired simultaneously. Therefore, the time and geometry information will provide rather limited constraints on the hit associations. The advantage of the WireCell approach is that it utilizes full TPC information. The strong requirement of the time/geometry/charge information provides a natural way to suppress electronic noise at the cost of being more sensitive to the hit inefficiency. Since the track and shower hypotheses are not used, the 3D imaging works for any event topology. Once the 3D images are reconstructed, 3D pattern recognition is needed to identify the content inside the image. Figure 4 shows the performance of the currently available 3D pattern recognition inside WireCell. More developments on the WireCell pattern recognition are needed before calculation of physics quantities will be possible. At the moment, the development of WireCell relies on the improvement in the TPC signal processing as well as the 3D pattern recognition techniques.

In the following, we briefly describe the concept of the WireCell tomographic imaging step. Calibrated WireCell imaging determines the likely spatial distribution of activity in the detector volume which is consistent with the measured signals. The distribution is defined on a collection of voxels filling the volume. The voxels are shaped as polygonal, right-angled

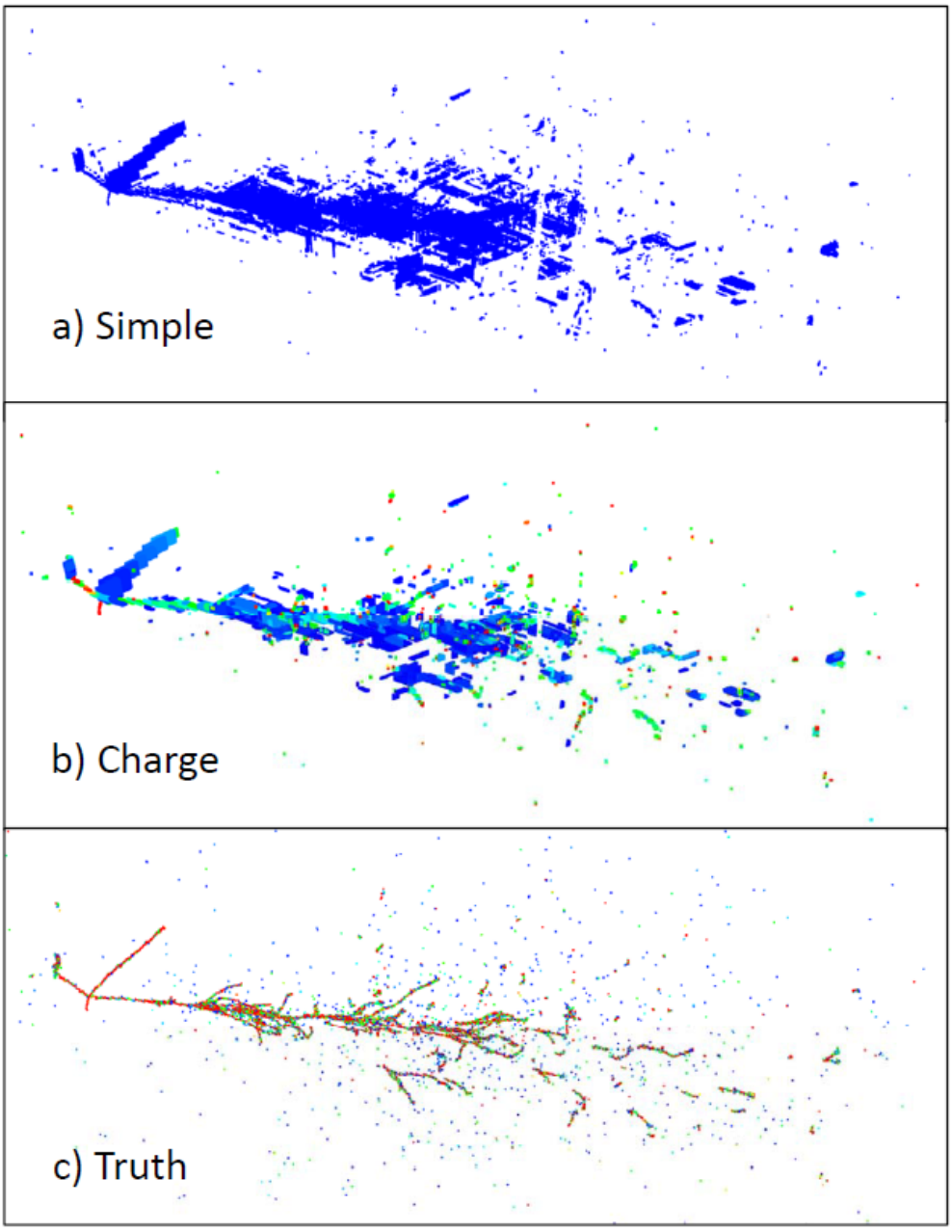

Figure 3: Comparison of imaging reconstruction qualities with and without the charge information.

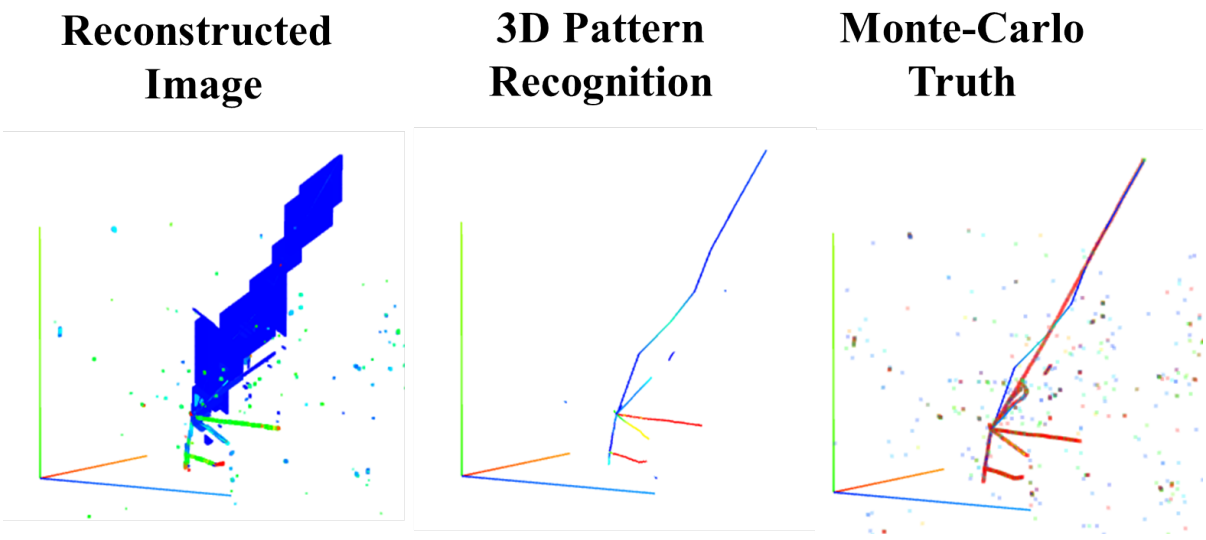

Figure 4: The reconstructed image is shown on the left panel for one neutrino interaction event. The image was passed through the 3D pattern recognition program with tracks identified (middle panel). The identified pattern is compared with Monte-Carlo truth (right panel).

extrusions. The two polygonal faces are called "cells" and are parallel to the wire planes.

A cell covers the region near a triple-overlap of one wire from each plane. Imagine a strip surrounding each wire with width $\pm\frac{1}{2}$ the wire pitch which runs parallel to the wire and in the wire plane. A cell is formed by the intersection of three such strips, one from a wire in each plane.

The sides of the voxels are parallel to the drift and extend to cover the distance electrons will drift during one "time slice" (chosen to be four time ticks due to expected timing resolution.).

The measured signal on a wire is subject to a threshold. For a given time slice, if the signal is above this threshold the wire is considered "hit". Likewise, for each time slice, any cell which has its three associated wires "hit" is itself considered "hit". [1] Given the time of the hit cell and external information about the initial interaction time (from the optical detector system), the cell can be projected into the detector volume along the drift path to provide the location of the voxel.

One of the unique features of the LArTPC is that each wire plane, be it induction or collection, provides a measure of the same distribution of ionization electrons. This feature is independent of the initial event topology (i.e. track angle, shower, vertex etc.). Therefore, this feature can be used to remove ambiguities made by using wire planes for the readout. Using the concept of wire and cell, we can thus write down the following charge equation:

$$B \cdot W = G \cdot C. \tag{6}$$

[1] In the real world case where some channels do not read out, the signal requirement is relaxed to consider the cell hit if at least two wires are hit and the third wire is a known dead channel. This leads to complications such as producing artificial cell hits ("ghosting").

Here, W represents a vector of charge measured in wires from all wire planes in a given time slice. B is a matrix connecting *merged wires* with single wires [2]. C is a vector representing the likely amount of ionization electrons in *merged cells* or *blobs* [3]. G is the geometry matrix connecting merged cells and the merged wires. This equation can be expanded into a chi-square function:

$$\chi^2 = (B \cdot W - G \cdot C)^T V_{BW}^{-1} (B \cdot W - G \cdot C), \tag{7}$$

which also takes into account the uncertainties of the measured charge in wires. In particular, $V_{BW} \equiv B \cdot V_W \cdot B^T$ is the covariance matrix describing the uncertainty in (merged) wire charges.

The minimum of the above chi-square function can be found by calculating the first derivative

$$\frac{\partial \chi^2}{\partial C} = 0 \rightarrow G^T V_{BW}^{-1} (B \cdot W - G \cdot C) + (B \cdot W - G \cdot C)^T V_{BW}^{-1} G = 0, \tag{8}$$

and the solution can be written as:

$$C = \left(G^T \cdot V_{BW}^{-1} \cdot G\right)^{-1} \cdot G^T \cdot V_{BW}^{-1} \cdot B \cdot W. \tag{9}$$

The core of the Eq. (9) is the inversion of the matrix $G^T \cdot V_{BW}^{-1} \cdot G$. When this matrix can be inverted, the charge of merged cells can be derived directly. For faked hits (merged cells without any ionization charge), the derived charge is likely to be close to zero. For real hits (merged cells with ionization charge), the derived charge is likely to be large and close to the actual true value. On the other hand, if this matrix can not be inverted, additional assumptions and more advanced techniques are needed to derive the solution. The details of these techniques are beyond the scope of this report, and will not be discussed here.

2.3.11 Optical Reconstruction

Optical Hit Finder

The first step of the DUNE optical reconstruction is reading individual waveforms from the simulated photon-detector electronics and finding optical hits – regions of the waveforms containing pulses. The optical hit contains the optical channel (SiPM) that the hit was found on, time corresponding to the hit, its width, area, amplitude, and number of photoelectrons.

The current DUNE optical-hit-finder algorithm searches for regions of the waveform exceeding a certain threshold (13 ADC counts), checking whether that region is wider than 10 optical TDC ticks, and, if it is, calculating the aforementioned optical-hit parameters for the region (including parts of the waveform around it that have ADC values greater than 1) and recording it as an optical hit. The number of photoelectrons is calculated by dividing

[2] A group of "merged wires" is formed by collecting together all neighboring hit wires in the time slice. This is done to reduce the rank of the matrix equation.

[3] "A group of "merged cells" is formed by collecting together all primitive cells which are hit and self-contiguous.

the full area of the hit by the area of a single-photoelectron pulse. The pedestal is assumed to be constant and is specified in the hit finder as 1500 ADC counts.

Optical Flash Finder

After optical hits are reconstructed, they are grouped into higher-level objects called optical flashes. The optical flash contains the time and time width of the flash, its approximate Y and Z coordinates (and spatial widths along those axes), its location and size in the wire planes, the distribution of photoelectrons across all photon detectors, and the total number of photoelectrons in the flash, among other parameters.

The flash-finding algorithm searches for an increase in photon-detector activity (the number of photoelectrons) in time using information from optical hits on all photon detectors. When a collection of hits with the total number of photoelectrons greater than or equal to 2 is found, the algorithm begins creating an optical flash. It starts with the largest hit and adds hits from the found hit collection that lie closer than 0.5 of the combined widths of the flash under construction and the hit being added to it. The flash is stored after no more hits can be added to it and if it has more than 2 photoelectrons.

The algorithm also estimates spatial parameters of the optical flash by calculating the number-of-photoelectron-weighted mean and root mean square of locations of the optical hits (defined as centers of photon detectors where those hits were detected) contained in the flash.

3 Dual Phase Simulation and Reconstruction Chain

Up until recently, LArSoft had only been used for simulation of single-phase TPCs. Software for dual-phase TPCs existed for the WA105 experiment, but had not been incorporated into LArSoft. This section describes the implementation of dual-phase simulation and reconstruction into the LArSoft framework for DUNE.

The design of the 10kt dual-phase (DP) detector module envisions a LArTPC with a fully active volume of $12 \times 12 \times 60$ m^3. Ionization charges produced in the active volume are drifted vertically upwards toward the liquid-gas boundary, extracted into the gaseous phase, amplified in the large electron multiplier (LEM), and collected on the anode with two orthogonal collection views having a pitch of 3.125 mm. The charge readout over the 12×60 m^2 area is accomplished with independent 3×3 m^2 modules containing the sandwiched LEM-anode tiles of 50×50 cm^2 and the grid for the charge extraction.

To model this segmentation of the charge readout plane (CRP) in the LArSoft simulation, one introduces independent TPC units with 12 m drift and readout area of 3×3 m^2 each. Fig.5 illustrates the implemented geometry in the case of 10 kt DP module. In the simulation the x-axis points in the direction of the electron drift, the y-axis is along the vertical, and z-axis is in the neutrino beam direction. Therefore, the charge readout is in xz-plane. It should be noted that while this orientation of the coordinate axes is unphysical (i.e., the Ar gas layer appears on the side of the detector instead of the top), it is necessary in order to make geometry compatible with:

- LArSoft requirement that the drift field is along $\pm x$,

- Definition of axis orientation already in use for geometry description of the single-phase TPC.

The origin of the coordinate system is set to be in the middle of the upstream face of the active volume similar to the geometry description of the single-phase detector option.

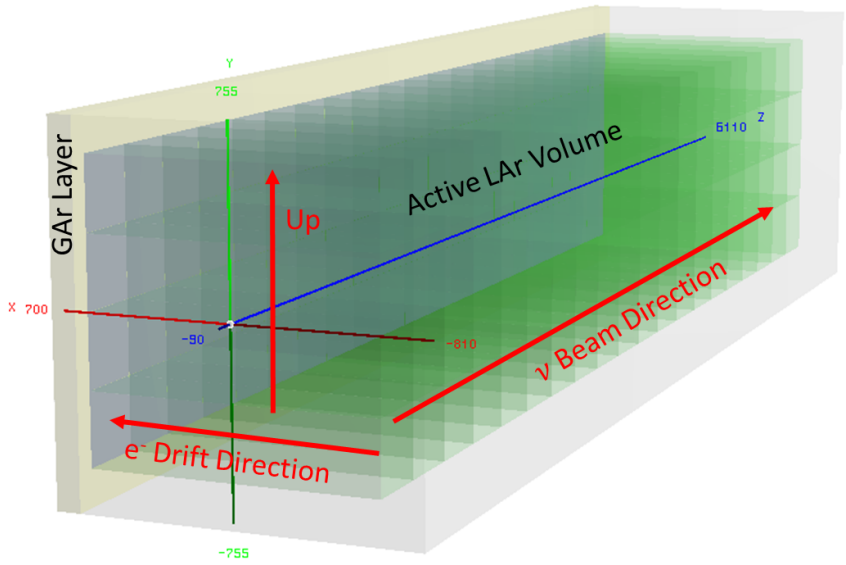

Figure 5: Illustration of the basic geometry for the 10kt DP TPC implemented in LArSoft. The active volume is in green and surrounding LAr buffer in light grey. The drift direction is along x, while the neutrino beam is in the z direction.

The overall dimensions of each CRP module in the simulation are set by the active area of each unit (3×3 m^2) plus the border. The latter is taken to be 5 mm based on the requirement for the CRP mechanical design. Such border width then results in a gap of 10 mm space between adjacent modules.

To simulate charge readout in LArSoft, the framework requires a consecutive collection of wire planes. This approach is well-suited for the description of single-phase detector, where the electron cloud is drifted in liquid argon across the induction views to the collection wires, but does not correspond to the case of the dual-phase detector, where the segmented anode collects charge simultaneously in two orthogonal views in the gaseous phase. To meet the framework requirements, however, the DP anode is modeled as a two thin "wire planes" 0.3 mm thick. A dummy electric field of 4.0 kV/cm ($v_{drift} \sim 3.5$ mm/μs in LAr), the maximal value for which the drift velocity calculation is valid in LArSoft, is applied between the two wire planes in order to allow drift of electrons from one collection plane to the other. This in effect introduces a small time difference between two collection views given by the electron drift time in the first wire plane:

$$\Delta t = t_{view1} - t_{view0} = \frac{0.3 \text{ mm}}{3.5 \text{ mm}/\mu\text{s}} = 86 \text{ ns}.$$

However, the offset is small compared 2.5 MHz ADC sampling rate (400 ns time bin) used by

the DP electronics and at most would correspond to 1 time tick difference in charge arrival times.

The charge amplification performed by the LEM is accomplished in the simulation by scaling true charge recorded on a given readout channel at a given time after taking into account electron lifetime and diffusion effects by the factor (*DPhaseSimChannelExtractService.DPGainPerView*) that parametrizes the expected gain per each collection view. After multiplying the collected charge by the gain factor the result is convoluted with the front-end amplifier response function, noise and pedestals are added, and the resultant signals are then quantized to generate expected raw ADC waveforms for each channel.

The basic checks of spatial and calorimetric reconstruction have been performed with the current implementation of dual-phase far detector geometry and detector simulation in LArSoft. The aim was to apply and validate the existing hit finding and hit fitting algorithms in LArSoft as a first step as these provide mandatory input to the higher level pattern recognition and 3D reconstruction (spatial and calorimetric).

Tests were performed using samples of 2 GeV/c muons simulated at different depths in the detector (drift distances), using the default value for the electron lifetime value of 3 ms. The aim was to reconstruct m.i.p. scale from relatively straight tracks that generate signals of different amplitudes and widths due to the charge attenuation by LAr impurities and diffusion of drifting electrons in LAr.

It was observed that the raw ADC waveforms of wire signals obtained with the default simulation parameters for the electron drift contained high fluctuations. This behavior was related to the procedure of diffusion simulation, where the spatial position and drift time of ionization electrons projected to wire planes is calculated for bunches (clusters) of electrons. The default number of electrons per cluster was too high for large drift distances giving a small number of clusters and thus resulting in a poor approximation of diffusion effects. Simply decreasing the number of electrons per cluster solves the issue but may lead to increase of computation time in case of busy events. Therefore a parameterized limit on the minimum number of clusters has been added to the LArSoft simulation code.

The standard hit reconstruction implemented in LArSoft consists of two steps:

- Deconvolution of the E-field and electronics response,
- Hit finding and fitting with the assumption of Gaussian shape of ionization signals.

While the deconvolution may include additional filters for the noise reduction, the implementation of deconvolution procedure itself acts as a sharp low-pass filter by removing frequencies at which electronics response or E-field response have too low an amplitude in the Fourier spectrum. The rationale is to avoid division by small values, which are likely estimated with high uncertainty. In practice such cuts lead to the removal of high frequency components leading to ringing oscillation artifacts around deconvolved signal pulses. Amplitudes of such oscillations at small drift distance are comparable to the signal peak amplitude at long drift distance making it difficult to reject these artifacts with a simple threshold cut during hit reconstruction. These oscillations can, however, be minimized with an additional filter. Fig. 6 shows the frequency spectrum of the electronics impulse response overlaid with the spectrum of the filter function adapted for the DP detector.

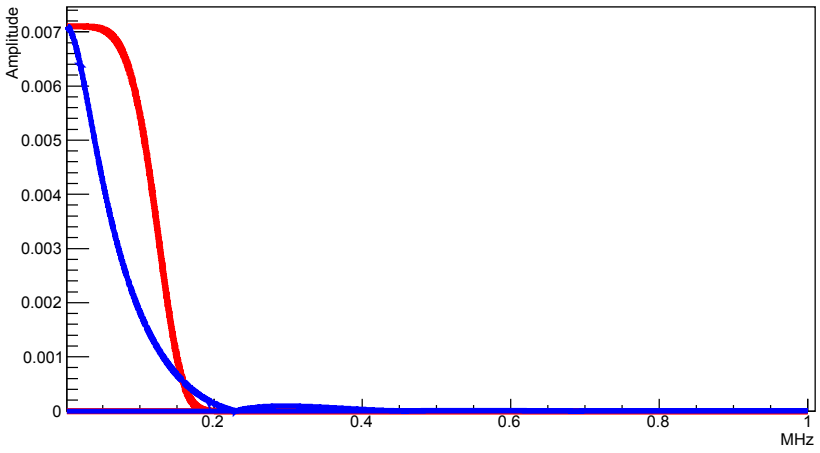

Figure 6: Fourier transform of the impulse response from DP electronics (blue) with filter response (red) overlaid.

One issue stemming from the deconvolution is to relate the estimated area under a reconstructed hit to the number of electrons. In principle, this calibration constant (*CalorimetryAlg.CalAreaConstants*) should be completely set by the readout chain (LEM gain, calibrated front-end electronics amplifier gain and response function). However, in the case of deconvolution, the required filtering leads to cuts in the frequency domain thus resulting in information loss. One, therefore, finds this calibration factor by tuning its value until the peak of the reconstructed dE/dx matches the m.i.p. expectation. Fig. 7 shows the reconstructed dE/dx for 2 GeV/c muons after the calibration constant is tuned to the m.i.p. scale.

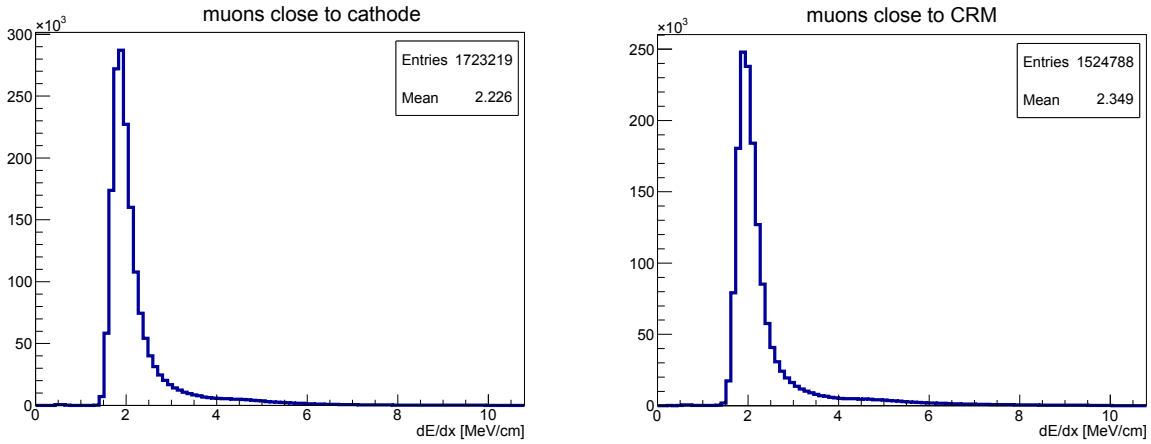

Figure 7: Reconstructed dE/dx from 2 GeV/c muons with electron lifetime of 3 ms. Left: tracks near to the cathode (large charge loss). Right: tracks near charge readout plane (small charge loss).

The use of the deconvolution for hit reconstruction is strongly motivated by bi-polar

nature in the response of induction planes in single-phase LAr TPC detectors (in general the bi-polar inductive response is also present in the collection view due to the signal induced on the neighboring strips/wires around a given collection channel; however, the effect is negligible). For the collection view an approach that relies on hit finding and fitting in the time domain (raw waveforms without deconvolution) is also suitable and could be used for the dual-phase detector since both views are collection views. The fit function in this case should include the signal shaping due to electronics response. An implementation of such algorithm has been proposed to be added to LArSoft hit reconstruction tool-kit and is currently under discussion.

Once the hit finding parameters are appropriately tuned the complete chain from the simulation up to 3D reconstruction can be run successfully with the dual-phase geometry. The reconstruction algorithms were tested on a sample of stopping muons (0.2 GeV/c) and protons (2 GeV/c). These samples contain several classes of low complexity topologies. Such topologies are expected to be reconstructed in detail, allowing analysis of interaction vertices and providing dE/dx evolution along the particle trajectories. The following reconstruction chain has been tested with the dual-phase detector simulation: Gauss hit fitting, linecluster serving as 2D pattern recognition to find objects in both planes, and Projection Matching Algorithm serving as 3D pattern recognition together with 3D trajectory fitting and vertex reconstruction. Fig. 8 shows the example of reconstruction output for a simulated event with a dual-phase detector geometry. Based on the experience with the same chain applied to single-phase simulation the results can be judged as comparable, however standard efficiency test were not applied at this stage. Some tuning of algorithms may be expected to accommodate differences in the two-point resolution or signal amplitudes over the long drift distances in dual-phase detector geometry.

4 Non-beam physics

This section describes the progress in implementing simulation tools in LArSoft and adapting the standard reconstruction for the DUNE physics not related to the neutrino beam.

4.1 Supernova and Low-Energy Neutrinos

4.1.1 Nature of the Signal and Reconstruction Challenge

The DUNE Supernova Burst and Low-Energy (SNB/LE) Neutrino Physics Working Group focuses on physics that can be done with neutrinos of less than about 100 MeV. This is physics enabled by the cosmogenically-quiet underground location of the detector. The primary physics topic is detection of the burst of neutrinos from a core-collapse supernova, with potentially very rich physics and astrophysics yield. The expected signal is a burst of neutrinos of all flavors in the few- to few-tens-of-MeV range within tens of seconds, of which the component detectable by the DUNE LArTPC is primarily ν_e.

The SNB/LE group also considers solar neutrinos (energies up to $\sim$ 15 MeV) and the diffuse supernova neutrino flux (DSNB) which should have roughly similar properties to the SNB flux, but much lower rate. For the latter two physics topics, the main issue is

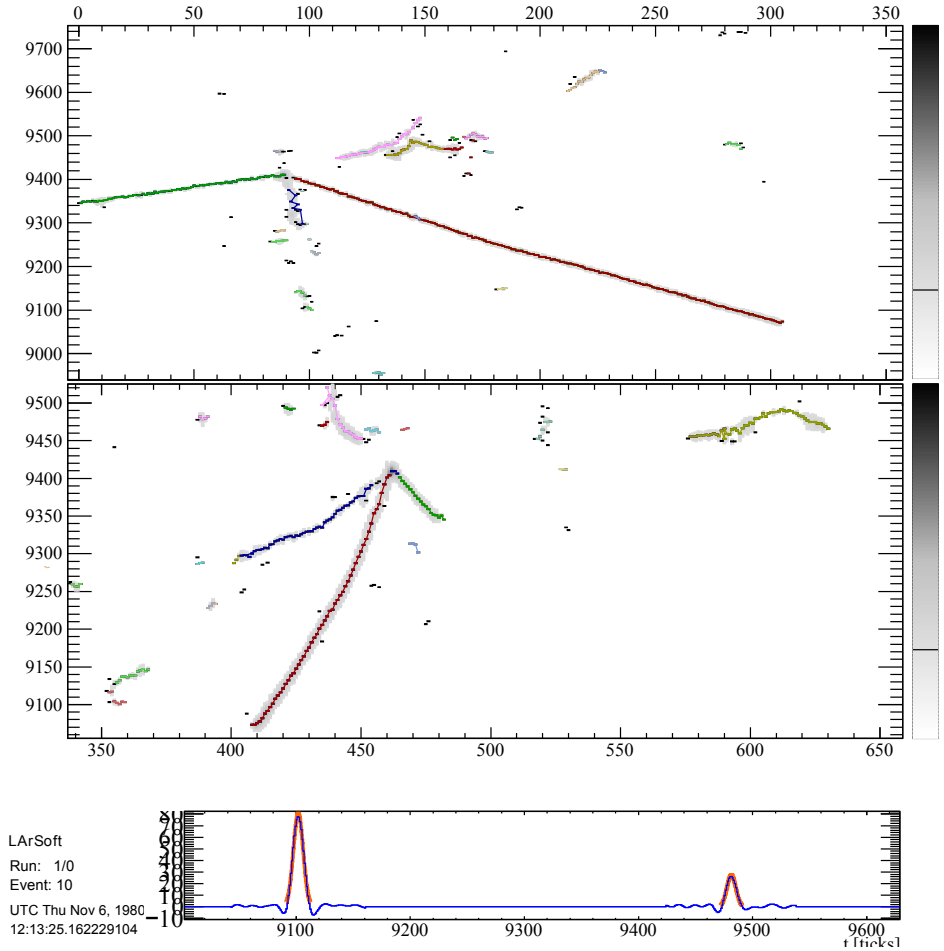

Figure 8: Example of the event reconstruction of a simulated proton with initial momentum of 2 GeV/c. The top two panels show event details in the channel number (x-axis) and time tick (y-axis) for two collection views. The bottom panel shows an example of the hit reconstruction on the channels.

background. If background is well enough understood for burst neutrinos, then we should have a handle on DNSB and solar neutrinos as well.

Supernova neutrino events, due to their low energies, will manifest themselves as small, perhaps few tens of cm, stub-like tracks from electrons (or positrons from the rarer $\bar{\nu}_e$ interactions). Events from ν_e charged-current interactions, $\nu_e + {}^{40}\mathrm{Ar} \rightarrow e^- + {}^{40}\mathrm{K}^*$, are likely to be accompanied by de-excitation products– gamma rays and/or ejected nucleons. Gamma-rays are in principle observable via energy deposition from Compton scattering, which will show up as small charge blips in the TPC. Ejected nucleons may result in loss of observed energy for the event. Elastic scattering on electrons will result in single scattered electrons, and single gamma rays may result from NC excitations of the argon nucleus. Each event category has, in principle, a distinctive signature.

As yet, far detector requirements (on argon purity, wire pitch, triggering, time resolution, photon collection, etc.) for supernova-neutrino detection are only roughly determined. Physics studies needed to determine these requirements require realistic simulations of signal and background and working reconstruction software.

The canonical reconstruction task is to identify the interaction channel, the neutrino flavor for CC events, and to determine the 4-momentum of the incoming neutrino; this overall task is the same for low-energy events as for high-energy ones. The challenge is to reconstruct the properties of the lepton (if present), and to the extent possible, to tag the interaction channel by the pattern of final-state particles.

So far, reconstruction algorithms for low-energy neutrinos in DUNE are poorly developed with respect to those for high-energy events. While some physics study and detector requirements work in the SNB/LE group uses a fast event-rate calculation tool called SNOwGLoBES, most activity is towards development of realistic and comprehensive simulation and reconstruction tools, from neutrino interaction event generators through full event reconstruction in both single and dual-phase detectors with LArSoft.

Understanding of backgrounds is also critical for understanding of how well we can reconstruct low energy events, and for setting detector requirements. Small single-hit blips from ${}^{39}\mathrm{Ar}$ or other impurities may fake de-excitation gammas and also affect triggering. Backgrounds may be especially important for photon detectors (which in turn may be important for energy resolution by correcting for attenuation of charge during drift)— see Section 4.1.7. Work on backgrounds is done in collaboration with the DUNE Radiopurity group.

4.1.2 SNOwGLoBES

Most supernova neutrino studies done for DUNE so far, including of the plots included in the CDR [30], have employed SNOwGLoBES[31], a fast event-rate computation tool. This uses GLoBES front-end software [1, 2] to convolve fluxes with cross-sections and detector parameters. The output is in the form of interaction rates for each channel as a function of neutrino energy, and "smeared" rates as a function of detected energy for each channel (*i.e.* the spectrum that actually be observed in a detector). The smearing (transfer) matrices incorporate both interaction product spectra for a given neutrino energy, and detector response. Time dependence in SNOwGLoBES can be straightforwardly handled by providing

multiple files with fluxes divided into different time bins. [4]

For default SNOwGLoBES, a detection threshold of 5 MeV in LAr is assumed as well as energy resolution from Ref. [32]. Furthermore, the current default detector response smearing for LAr in SNOwGLoBES assumes that all energy from de-excitation products is captured, which is likely a poor assumption. User-created transfer matrices have also been used for some studies [33, 34].

While SNOwGLoBES is, and will continue to be, a fast, useful tool, it has limitations with respect to a full simulation. One loses correlated event-by-event angular and energy information, for example. Ideally one does studies with high-statistics simulated data with realistic event generators and detector response. When full simulation studies are constrained by computational resources, one can update transfer matrices using improved simulation and still use SNOwGLoBES to draw useful conclusions.

4.1.3 Event Generators

We have developed two event generators for supernova neutrino events.

- `SNNueArCCGen` is a simple ν_eCC event generator written by AJ Roeth and Gleb Sinev [35]. This simulates ν_e charged-current interactions accompanied by de-excitation gammas. It calculates the cross section using a model based on measurements of ^{40}Ti β^+ decay to ^{40}Sc, which is a mirror of the ν_e+^{40}Ar CC interaction's ^{40}K final state. This model uses the beta-strengths to calculate the cross section and subsequently uses a 73-level gamma de-excitation Monte Carlo to simulate the gammas. This generator is now incorporated into LArSoft and samples from a cross-section weighted GKVM [31] spectrum by default. It does not take into account Ar excitations above 7 MeV, nor final-state de-excitations via nucleons. However for some purposes, such as DAQ simulations, this event generator should be satisfactory. This generator has been used to produce samples for the MCC.

- MARLEY (Model of Argon Reaction Low Energy Yields), developed by Steven Gardiner and the UC Davis group, supersedes `SNnueArCCgen` in physics modeling accuracy. MARLEY simulates tens-of-MeV neutrino-nucleus interactions in liquid argon. Currently, MARLEY can only simulate charged-current ν_e scattering on ^{40}Ar, but other reaction channels will be added in the future.

  MARLEY weights the incident neutrino spectrum, selects an initial excited state of the residual ^{40}K* nucleus, and samples an outgoing electron direction using the allowed approximation for the ν_e CC differential cross section.[5] MARLEY computes this cross

[4] Note that SNOwGLoBES is *not* a Monte-Carlo code— it calculates mean event rates using a transfer matrix to convert neutrino spectra to observed spectra.

[5] That is, the zero momentum transfer and zero nucleon velocity limit of the tree-level ν_e CC differential cross section, which may be written as

$$\frac{d\sigma}{d\cos\theta} = \frac{G_F^2 |V_{ud}|^2}{2\pi} |\mathbf{p}_e| \, E_e \, F(Z_f, \beta_e) \left[(1 + \beta_e \cos\theta) B(F) + \left(\frac{3 - \beta_e \cos\theta}{3} \right) B(GT) \right].$$

In this expression, θ is the angle between the incident neutrino and the outgoing electron, G_F is the Fermi constant, V_{ud} is the quark mixing matrix element, $F(Z_f, \beta_e)$ is the Fermi function, and $|\mathbf{p}_e|$, E_e, and β_e are

section using a table of Fermi and Gamow-Teller nuclear matrix elements. Their values are taken from experimental measurements at low excitation energies and a quasiparticle random phase approximation (QRPA) calculation at high excitation energies. As the code develops, a more sophisticated treatment of this cross section will likely be included.

After simulating the initial two-body $^{40}\mathrm{Ar}(\nu_e,\ e^-)^{40}\mathrm{K}^*$ reaction for an event, MARLEY also handles the subsequent nuclear de-excitation. For bound nuclear states, the de-excitation γ-rays are sampled using tables of experimental branching ratios. These tables are supplemented with theoretical estimates when experimental data are unavailable. For particle-unbound nuclear states, MARLEY simulates the competition between γ-ray and nuclear fragment[6] emission using the Hauser-Feshbach statistical model.

Although many refinements remain to be made, MARLEY's treatment of high-lying Gamow-Teller strength and nuclear de-excitations represents a significant improvement over existing tools for simulating supernova ν_e CC events. An early version of MARLEY has been incorporated into the LArSoft code base and will soon be distributed in official LArSoft releases.

4.1.4 Report from Hack Days

On July 25-27, 2016, the SNB/LE working group held a "Hack Days" event at Fermilab, with the purpose of making progress on reconstruction tasks, and also to get group members trained on LArSoft and other software tools. This was very successful. Members signed up for several tasks; some completed some shorter tasks and others were launched on longer-term projects [36].

Table 4.1.4 lists some tasks and status. At the time of this report, most of the projects are not complete. However we expect many to be completed, or significant progress made, on the timescale of a few months.

We plan to hold another Hack Days before the January 2017 collaboration meeting.

4.1.5 Reconstruction Progress

One very fruitful outcome of the Hack Days was development of a set of tweaks to the reconstruction in order to successfully reconstruct electrons with energies less than 20 MeV. The changes were suggested by Tingjun Yang and have been incorporated in the latest `larreco` version. Figure 9 shows efficiency for reconstructing 3D space points before and after these changes.

This first-order reconstruction of low-energy events is enabling many studies to go forward. However, we have yet to test effectiveness for reconstructing more complicated event topologies; identifying "blips" from secondaries will likely require additional algorithms.

---

the outgoing electron's three momentum, total energy, and velocity, respectively. $B(F)$ and $B(GT)$ are the Fermi and Gamow-Teller matrix elements.

[6] Nucleons and light nuclei up to ^{4}He are considered.

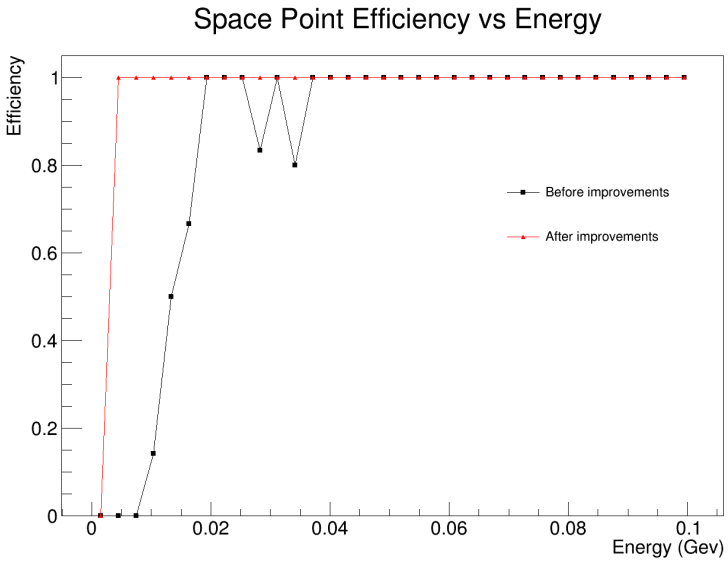

Figure 9: Efficiency for finding space points, defined as fraction of events with at least one 3D space point reconstructed, as a function of electron energy, for single electrons in the 10 kt workspace geometry (fixed vertex and direction). The black line represents "out-of-the-box" LArSoft and the red line shows efficiency after improvements.

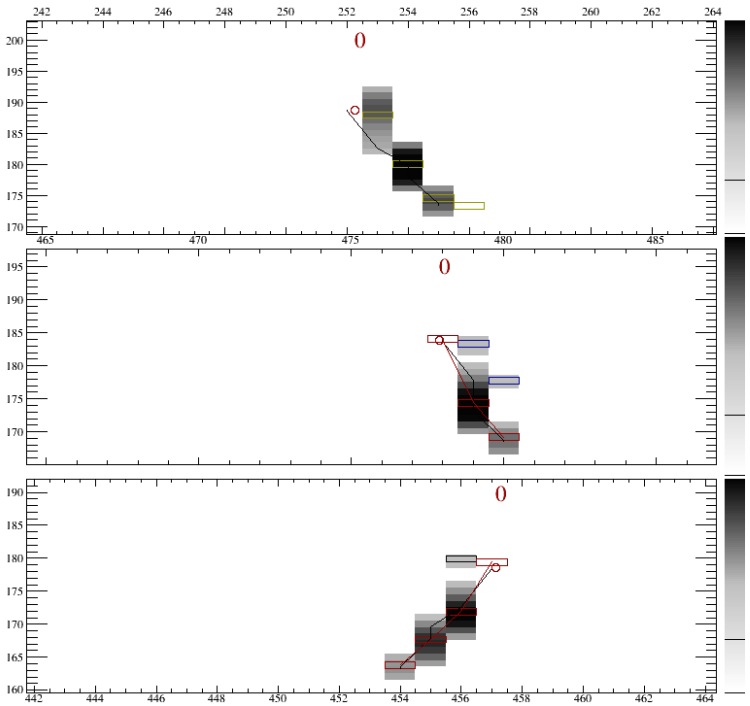

Figure 10: Example of reconstructed 10 MeV electron.

Person	Task	Status
C. Backhouse	Study of photon detectors to improve energy reconstruction	Complete
E. Conley	Study of bremsstrahlung vs de-excitation gammas	Partially complete
S. Gardiner	MARLEY development	LArSoft integration complete, studies underway
A. Habig J. Vasel	Port of NOvA GENIE-based SN event generator	Partially complete
D. Navas	Event reconstruction with MARLEY, single vs dual phase studies	Partially complete
C. Lastoria	Angular resolution for ES channel	Partially complete
AJ Roeth	Develop algorithm to select 10-MeV NC gammas	Reconstruction accomplished, selection complete
K. Scholberg	New smearing matrices for SNOwGLoBES using realistic event generators	Partially complete
J. Stock	Tl-208 impurity map	Partially complete
E. Stewart A. Weinstein	Simulated event production for DAQ development	Partially complete
D. Whittington	New efficiency maps for determining t0 from photons for low-energy events	Preliminary maps created

4.1.6 DAQ and Triggering Progress

A key challenge for supernova detection will be to devise a way to trigger efficiently on the burst and retain all relevant information. This is not trivial given that there is no beam trigger, and the burst events are low enough in energy that required thresholds are low enough that data rates without clever zero suppression will be required to avoid overwhelming data rates. Strategies involve looking for bursts of stub-like events in the TPC over a time-scale of 10 seconds, but in principle can incorporate also photon detector information.

The SNB/LE group is working with a subgroup of the DAQ working group (Georgia Karagiorgi, Amanda Weinstein, Michael Baird) to develop simulated data with characteristics suitable for trigger and DAQ studies. The short-term strategy is to use a fast and simple simulator independent of LArSoft that generates trigger primitives based on the expected energy and time profile of a supernova burst. A first such time-profile simulator is under development by Michael Baird, and improvements will be informed by more detailed simulation studies as they develop. Pile-up of burst signal events is not yet implemented but expected to be small for all but the closest supernovae.

4.1.7 Photon Studies for Low-Energy Events

Photon information will also be important for supernova burst events for improving energy resolution by allowing for correction of drift time via the vertex information available from fast photon timing. Furthermore they are in principle useful for triggering.

Preliminary simulation studies of photon detector efficiencies are shown in Fig. 11; in general improved efficiencies would be desirable at low energy.

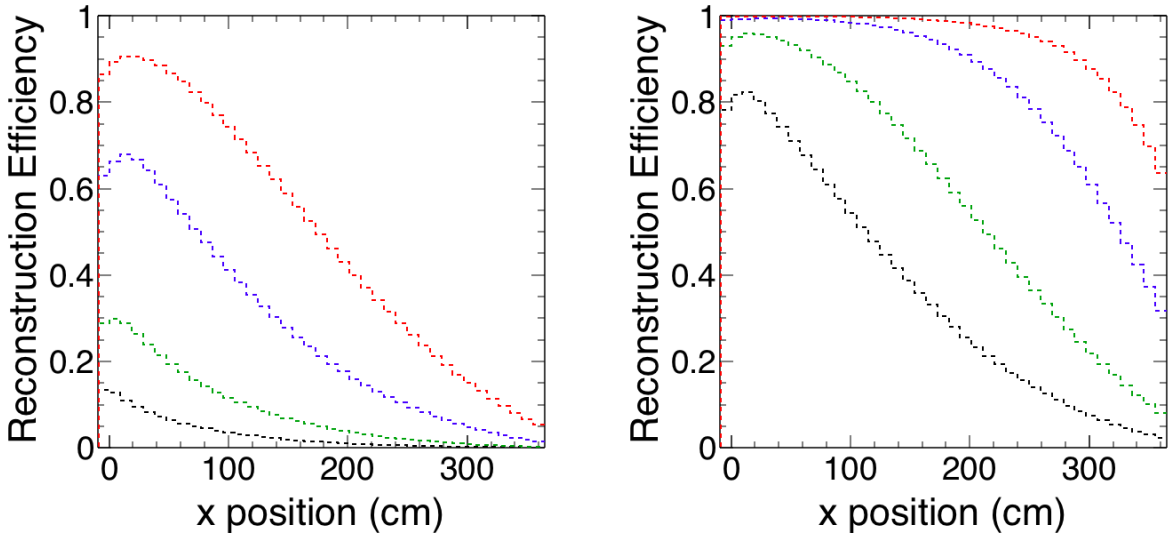

Figure 11: Left: photon simulation study result by Alex Himmel, evaluating efficiency of photon detection for different electron energies (red: 50 MeV, blue: 20 MeV, green: 10 MeV, black: 5 MeV) as a function of distance from light collection bar, for the DUNE reference design. Right: similar study for the alternate photon detector design.

So far, photon studies have included studies of energy resolution improvements. Fig. 12 shows an example study by Gleb Sinev, demonstrating the resolution improvement (from $\sim 22\%$ to $\sim 13\%$) using MC truth to correct for electron drift. A Hack Days study by Chris Backhouse demonstrated that a "realistic" correction using the photon simulation in place of MC truth was nearly as good as the MC truth correction.

In addition, in collaboration with the radiopurity group, studies are underway of the effect of ^{39}Ar, and other backgrounds such as radon, on trigger rates (e.g., [37]): see Fig. 13.

A Photon Detector Task Force (see Section 6.4) will be examining these issues more carefully in order to determine requirements for photon detectors, and will be working in close collaboration with the SNB/LE group.

4.2 Nucleon Decay Physics

The purpose of the DUNE Nucleon Decay (NDK) Physics WG is to evaluate and demonstrate the experimental sensitivity of DUNE to various nucleon decay modes and other baryon number non-conserving processes, such as neutron-antineutron oscillations. Sensitivity to

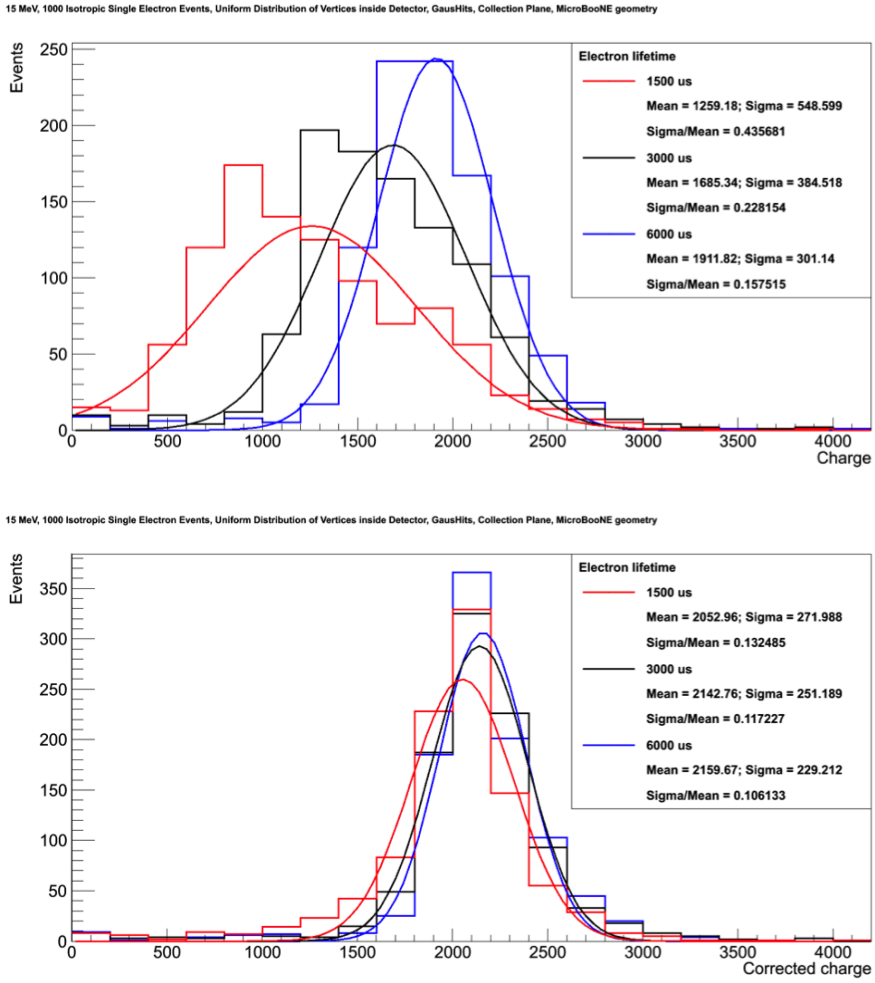

Figure 12: Studies by Gleb Sinev of energy resolution for 15-MeV electrons for different drift times, without (top) and with (bottom) drift correction using MC truth position.

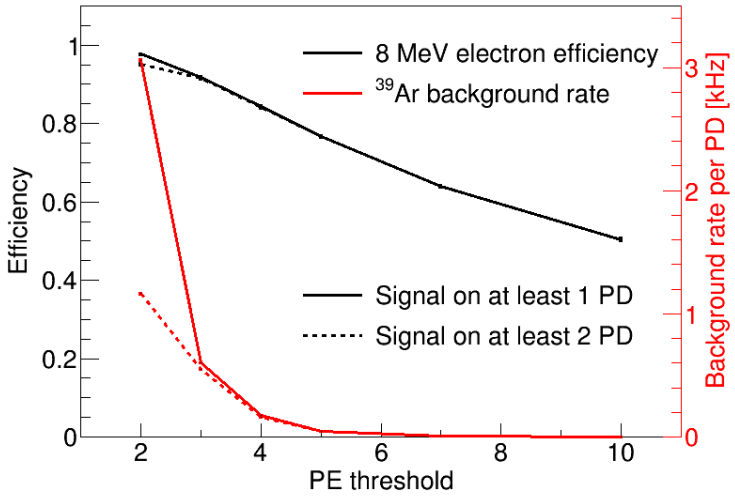

Figure 13: Study of ^{39}Ar background for photon triggering by Gleb Sinev, showing efficiencies and background rates for 8-MeV electrons, with simulated ^{39}Ar. The dashed lines show the effect of reduced background (with only modest decrease in efficiency) by requiring a 2-flash trigger.

a specific NDK mode is expressed in terms of the partial lifetime τ/B, where B is the branching fraction of the NDK mode being considered. Experimentally, the τ/B sensitivity can be written as:

$$\tau/B = n \cdot \varepsilon \cdot Mt/N_S \tag{10}$$

where n is the number of protons or neutrons (depending on the NDK mode) per unit mass, ε is the signal selection efficiency, Mt is the detector exposure, N_S is the largest number of signal events compatible with a background-only data sample. The lower the background rate, the lower N_S, and hence the higher the τ/B sensitivity. DUNE sensitivities reported in the CDR [30] for the $p \to \bar{\nu}K^+$ mode, as well as in earlier studies, assumed preliminary estimates for the signal efficiency and background rates [38]. An important goal of the NDK Physics WG, and of this Far Detector Task Force, is to refine these estimates via fully simulated and reconstructed event samples. Another important goal is to extend DUNE NDK studies to promising modes other than $p \to \bar{\nu}K^+$. This section focuses on recent progress toward full simulation, reconstruction, and analysis for NDK signal events. The focus will be on $p \to \bar{\nu}K^+$, but other modes will be discussed as well. Cosmogenic backgrounds to NDK are discussed in Sec. 4.4.

The simulation of NDK events includes the NDK event generation within GENIE [39, 40], the tracking of particles through the DUNE far detector geometry within GEANT4, and the hit-level simulation through LArSoft's detsim module. The last two steps are common to other physics measurements and searches, and are discussed elsewhere. We focus here on NDK event generation.

GENIE is used for generation of nucleon decay events, since the treatment of nuclear effects on the initial and final nuclear state are common with the modeling of neutrino interactions, GENIE's primary physics goal. During the last year, we have made major progress both

within GENIE, and concerning GENIE-LArSoft integration for NDK simulation. A summary of the GENIE and LArSoft-related tasks accomplished by the NDK working group is listed here:

1. **Upgraded GENIE to include the full 68 exclusive nucleon decay modes listed by the Particle Data Group**
   The current GENIE production release (v2.10) can only simulate 11 NDK modes, which are all $(B-L)$-conserving antilepton plus meson modes, see [39, 40]. However, the Particle Data Group reports experimental searches for as many as 68 exclusive modes [41]. These modes include 2, 3, or 5 particles in the final state. They include antilepton plus meson(s), lepton plus meson(s), antilepton plus photon(s), and three (or more) leptons decay modes. A GENIE Incubator Project to upgrade GENIE to include all such NDK channels has been created [42]. The code exists in a GENIE development branch and is under review by the GENIE team. The goal is to include this upgrade in the GENIE v2.12 production release.

2. **Improved the GENIE-LArSoft interface to allow seamless event generation without the awkward step that was previously required to bridge the two formerly-independent pieces of software via an ASCII file**
   Until recently, NDK event generation consisted of a LArSoft module reading GENIE event records in ASCII format, assigning decay vertices with the argon of the detector geometry being used. This approach had the disadvantage that it required running a stand-alone GENIE application. We are now able to simulate GENIE NDK events directly within the LArSoft module, through calls to the appropriate GENIE libraries, hence avoiding the need of a separate GENIE executable [43]. This greatly simplifies the production of NDK event samples as part of DUNE official Monte-Carlo productions.

3. **Identified and fixed a bug in GENIE related to kaon inelastic interactions**
   In GENIE (v2.10), kaon inelastic interactions have no particles in the final state for NDK-generated kaons, as in $p \to \bar{\nu}K^+$. This has now been fixed, resulting in only 0.2% of K^+ being lost within the Ar nucleus in $p \to \bar{\nu}K^+$ events, according to GENIE [44]. This is to be compared with the 3.2% number in Ref. [38], based on the FLUKA [45] modeling of $K^+ + n \to K^0 + p$ charge-exchange reactions within the Ar nucleus.

4. **Identified and fixed a bug in LArSoft in which NDK event vertices were incorrectly distributed through the argon volume**
   In LArSoft, NDK vertices were incorrectly assumed to follow a gaussian distribution within the Ar volume. This has now been changed to follow a uniform distribution [46]. Examples of fully simulated NDK events within the DUNE 1×2×6 far detector geometry are shown in Fig. 14. The left images in Fig. 14 show a $p \to \mu^+ K^0$ event, a promising mode whose study in DUNE has been enabled by the recent simulation upgrades, while the right images show a $p \to \bar{\nu}K^+$ "golden" mode event.

5. **Upgraded GENIE to simulate neutron-antineutron oscillation**
   A GENIE Incubator Project for neutron-antineutron oscillation simulation has been created [47]. This module is under review by the GENIE collaboration, and will also be included in a future GENIE production release.

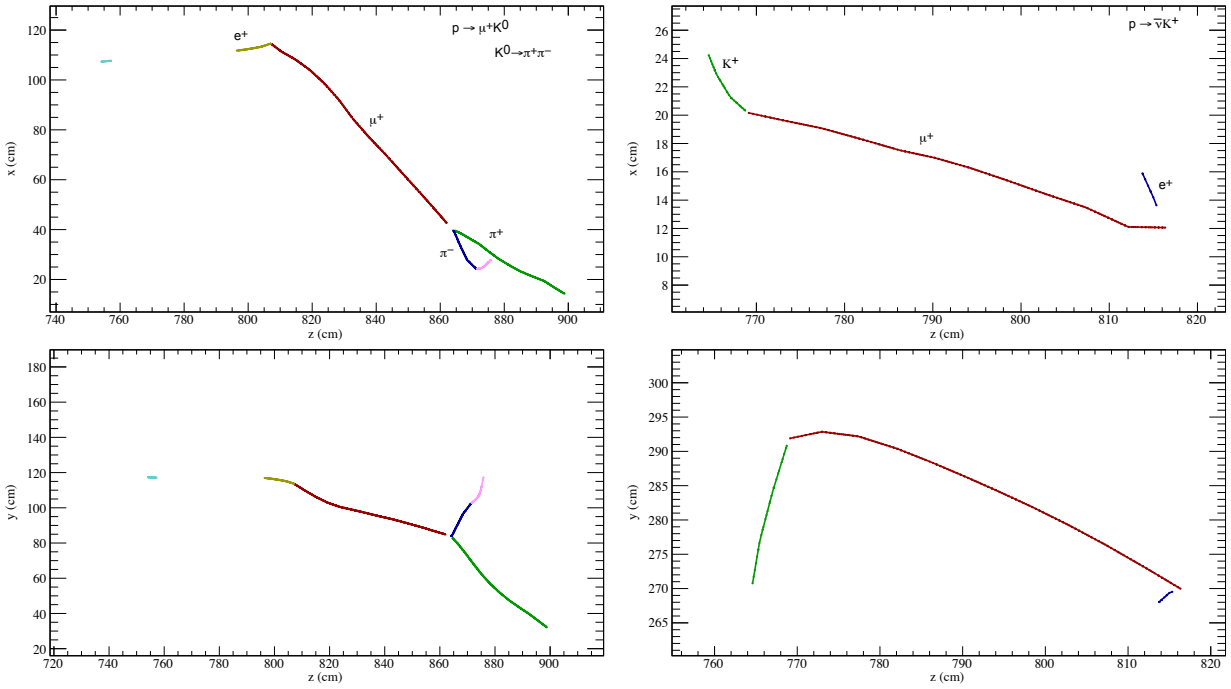

Figure 14: Left: Event display of a fully reconstructed $p \to \mu^+ K^0$ event simulated in DUNE, where $\mu^+ \to e^+ \nu_e \bar{\nu}_\mu$ and $K^0_S \to \pi^+ \pi^-$. From [49]. Right: Event display of a fully reconstructed $p \to \bar{\nu} K^+$ event simulated in DUNE, where $K^+ \to \mu^+ \nu_\mu$ and $\mu^+ \to e^+ \nu_e \bar{\nu}_\mu$. From [50].

Progress has also been made in validating and improving reconstruction for NDK events. In addition to high tracking efficiency, excellent particle identification though the measurement of the dE/dx profile of stopping particles is crucial for NDK physics. DUNE aims not only to efficiently reconstruct, but also to identify, all charged particles produced in NDK events. The NDK working group has made progress in the following topics related to event reconstruction and particle identification:

1. **Evaluating tracking efficiencies for particles produced in $p \to \bar{\nu}K^+$ events, using the Projection Matching Algorithm (PMA, [27])**
   For K^+'s, the default PMA algorithm used for long-baseline oscillation physics studies results in a 64% overall tracking efficiency for K^+'s [48]. The efficiency is highly momentum-dependent, with an efficiency exceeding 80% for > 0.3 GeV/c kaons, as shown in the left panel of Fig. 15. In $p \to \bar{\nu}K^+$ events, kaons are expected to have momenta distributed in the 0.1–0.5 GeV/c range, because although the decay produces a monoenergetic kaon, its momentum can be modified by Fermi momentum as the kaon escapes the nucleus. The efficiency for μ^+ and e^+ produced in $K^+ \to \mu^+\nu_\mu$ decays (63.6% branching fraction) is not shown here, but is somewhat higher. We expect that improvements can be made during the next months by customizing the reconstruction algorithms for better performance to relatively low momenta ($\sim$0.1 GeV/c). As an example, the left panel of Fig. 15 shows the results for K^+ tracking efficiency using an alternative cluster algorithm (TrajCluster module) compared to the standard algorithm for tracks (LineCluster module). Tracking performance is also being evaluated in terms of single-track momentum and direction resolution, and for invariant mass resolution for two-body decays of neutral mesons (π^0, K^0_S, ρ^0) [48, 49].

2. **Evaluating PID efficiencies and mis-ID rates for $e/\mu/\pi/K/p$ separation [49, 50]**
   Distributions from a particle identification algorithm (PIDA, [51]) applied to all reconstructed particles in simulated $p \to \bar{\nu}K^+$ events is shown in the right panel of Fig. 15. The algorithm is applied here only on the last 15 cm of the tracks. Studies are in progress to understand the current status and improve where possible. An important difference between beam and NDK events is that no preferred direction exists in the latter case, and detector-only information can be used to determine the track direction. We have verified with ($p \to \bar{\nu}K^+$, $K^+ \to \mu^+\nu_\mu$) events that the same dE/dx information along the track works very well also to determine the K^+ track direction, and hence the NDK vertex [50].

3. **Assessing photon detector performance in relation to NDK physics [52]**
   The photon detector system (PDS) is sensitive to the primary scintillation light from Ar de-excitation and electron-ion recombination. The PDS is particularly important to enable non-beam physics discussed here, especially to provide drift position determination and hence fiducial volume definition. About 10^3 photo-electrons (PEs) are expected on average for $p \to \bar{\nu}K^+$ events and the current PDS assumptions. The amount of detected light varies greatly with the distance between the NDK vertex and the APA plane where the PDS is installed. Figure 16 shows the efficiency to reconstruct a flash of light as a function of such distance, and for different PE thresholds for

Table 1: List of possible NDK modes where DUNE may have an early discovery potential. See text for details. The current limits for these modes are also shown in the table. Adapted from [53].

Mode	PDG ID	Current Limit (10^{33} yr)
$n \to e^+ K^-$	13	> 0.017
$p \to e^+ K^0$	13	> 1.0
$n \to \mu^+ K^-$	16	> 0.026
$p \to \mu^+ K^0$	16	> 1.6
$p \to e^+ K^{*0}$	21	> 0.084
$n \to e^- K^+$	34	> 0.032
$n \to \mu^- K^+$	35	> 0.057
$p \to e^- \pi^+ K^+$	40	> 0.075
$p \to \mu^- \pi^+ K^+$	41	> 0.245

the PDS (in the 2–20 PE range). The efficiency is satisfactory: it is greater than 97% for NDK vertex-APA distances lower than 340 cm. Fake associations between charge and light signals might be produced by light flashes from ^{39}Ar radioactive decays. The number of reconstructed ^{39}Ar flashes can be significant for few-PEs thresholds, as also shown in Fig. 16. In the future, the spatial reconstruction of the flash across several PDS elements will be studied to discriminate flashes of light between ^{39}Ar, NDK, atmospheric neutrino and cosmogenic events.

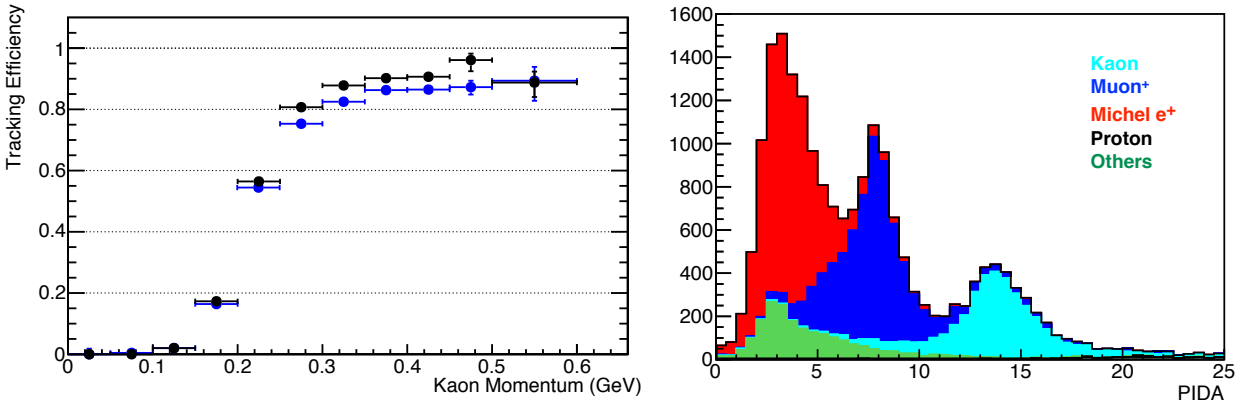

Figure 15: Left panel: K^+ tracking efficiency versus K^+ momentum in $p \to \bar{\nu} K^+$ events. Blue symbols: using standard 2D clustering algorithm (LineCluster) as tracking input. Black symbols: using alternative clustering (TrajCluster). Right panel: PIDA distribution for reconstructed particles in $p \to \bar{\nu} K^+$ events where $K^+ \to \mu^+ \nu_\mu$. PIDA is computed using the last 15 cm of the tracks. From [50].

As far as NDK analysis, the focus has been on:

1. **Identification of promising NDK modes**
   A comprehensive list of NDK modes where DUNE may have an early discovery potential has been produced [53], see Tab. 1. In this context, early discovery potential is

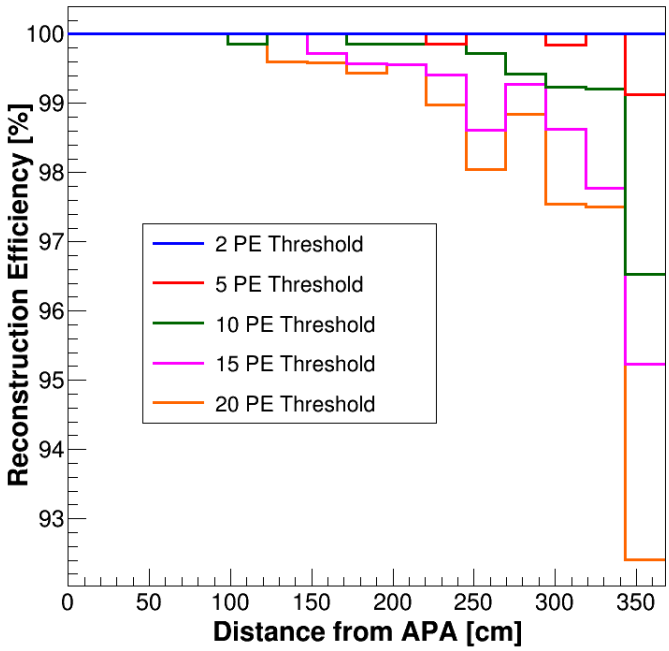

Threshold (PEs)	^{39}Ar flashes (#/APA/drift)
2	30
5	3
10	0.08
15	0.004
20	0.0003

Figure 16: Flash finding efficiency for $p \to \bar{\nu} K^+$ events, as a function of the flash distance from the closest APA and for different PE thresholds. The table at the right indicates the expected rate of ^{39}Ar flashes above threshold. From [52].

defined as DUNE having a sensitivity after a 40 kton·yr exposure that is potentially greater than the current limit and the Super-Kamiokande sensitivity extrapolated to the year 2025. The assumed DUNE sensitivities account for nuclear effects responsible for irreducible efficiency losses. However, they should be regarded as rough indications only, as they assume zero background and approximate reconstruction efficiencies. Nonetheless, they provide a useful subset of modes that are candidates for more realistic Monte-Carlo simulations. As the table shows, DUNE is expected to do well in NDK modes with charged or neutral kaons in the final state, or in multi-prong decays. Modes with neutrinos in the final state may also be promising. They are, however, not listed in Tab. 1, as reliable estimates for their relatively large backgrounds are particularly important in this case.

2. **Evaluating NDK signal efficiencies**
   A realistic estimate of NDK signal efficiencies for fully reconstructed $p \to \bar{\nu} K^+$, $p \to l^+ \rho^0$ and $p \to \mu^+ K^0$ events has just started [49, 50], and will continue to make progress in coming months.

3. **Evaluating NDK background rates**
   A realistic estimate of NDK backgrounds from both cosmogenically-induced events and from atmospheric neutrino events is a critical component of these analyses. Cosmogenic background studies are discussed in more detail Section 4.4. Studies of atmospheric neutrino backgrounds are just beginning.

4. **Evaluating NDK sensitivities**

Python-based scripts have been developed to evaluate DUNE sensitivities as a function of exposure, signal efficiency, and background rate assumptions. These are available to the collaboration [54].

The NDK working group has made good progress over the last year in each of the areas that is critical for the success of NDK searches in DUNE. Although there is still much work to be done, the forward motion over the past year is largely thanks to the efforts of our dedicated working group members.

4.3 Atmospheric Neutrino Physics

Atmospheric neutrino studies for LBNE and LAGUNA-LBNO relied on smeared truth-level quantities rather than full simulations and reconstruction. These previous studies focused on the neutrino mass hierarchy, determining the octant of θ_{23}, and observation of CP violation. In DUNE the focus of effort has been to continue the study of interesting physics signatures, and to move away from truth-level studies to full simulation and reconstruction.

Atmospheric Neutrino Simulation and Reconstruction: Within LArSoft, users can now generate and process atmospheric neutrino events through all of the necessary stages: event generation with GENIE, GEANT4 simulation of energy deposition, detector simulation, reconstruction, and analysis. The current LArSoft configurations allow one to simulate events using the Bartol atmospheric neutrino fluxes calculated at solar max or solar min [55]. Improvements have been made to numerous elements of this software stack, and areas where further work is necessary have been identified.

The generation stage brings together the detector mass model, an atmospheric neutrino flux calculation, and the neutrino interaction cross sections, using a piece of GENIE code known as the Event Generation Driver. Several groups world-wide carry out calculations of atmospheric neutrino fluxes [55, 56, 57], and the GENIE flux drivers have been extended so that they are able to use calculations from all of these groups. Most of these groups have now performed calculations for the geomagnetic location of the Homestake site, and we hope in the future to also have calculations which include the local topography [58]. The addition of the ATMNC flux [57] necessitated changes to the structure of the GENIE atmospheric event drivers, as this computation included additional information, such as the azimuthal-angle dependence of the flux, and direction-dependent production height tables, which were not included in previous flux calculations. Some additional work will be required to extend the GENIE output record in order to pass through needed flux-related information, such as the neutrino production height, for the purposes of downstream analyses. The existing drivers are rather slow - arising from the fact that atmospheric neutrinos have a broad and rapidly falling energy spectrum, and by default GENIE strobes neutrinos through the full detector in order to compute the probability of interaction (relative to the maximum probability which it also determines). This has not proved to be a bottleneck for analyses studies to date, but is an area where significant speedup is possible.

There has also been improvement on the cross section side of GENIE with the incorporation of the Athar et al. model for neutrino $\Delta S = 1$ scattering into GENIE release 2.10.0 [59, 60]. This model, which provides an improved description of $\Delta S = 1$ CC interactions up to 3 GeV, is not turned on by default, but is expected to be part of a comprehensively retuned

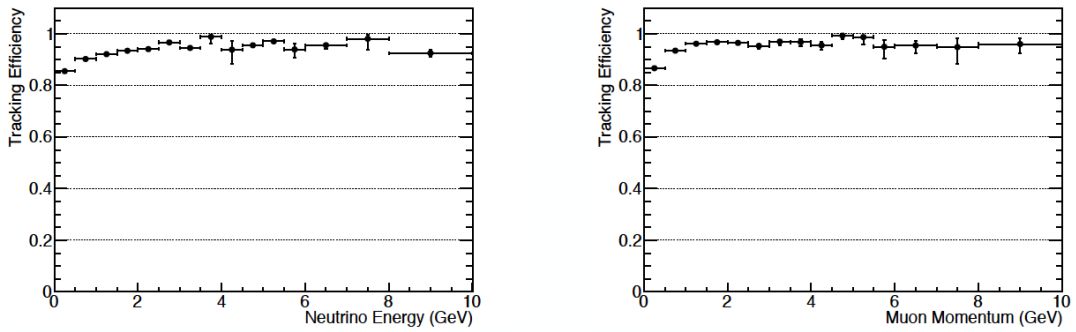

Figure 17: Muon tracking efficiency for atmospheric muon neutrino CC interactions as a function of neutrino energy (left) and muon momentum (right). From [48].

version of GENIE available in the future.

Atmospheric neutrino interactions have been carried through the entire simulation and analysis framework, and preliminary studies on how well the reconstruction works on these events have been performed [48]. Figure 17 shows the muon tracking efficiency for atmospheric muon neutrino CC interactions as a function of neutrino energy and muon momentum. Overall the muon tracking performance is found to be similar to that for beam neutrinos, with tracking failures most often occurring when muons are traveling parallel to the electron drift. As the atmospheric neutrino beam is arriving from all directions this particularly challenging orientation can be achieved for any muon (or neutrino) energy. Understanding the energy and angular dependence of these efficiency curves will be important for atmospheric neutrino studies which rely on resolving features of neutrino oscillograms.

The previous studies demonstrated that DUNEs excellent neutrino energy and pointing resolution can compensate for the relatively small fiducial volume, resulting in competitive physics sensitivities. The mass hierarchy sensitivity, for instance, relies primarily on measurement of neutrinos with energies from 1 to 10 GeV, an energy regime largely insensitive to some of the detector optimization decisions currently being debated. Over the past year we have therefore tried to encourage study of additional DUNE physics topics that might take advantage of these same strengths for lower energy interactions. Two examples are the study of matter effects using low energy atmospheric neutrinos [61], and the measurement of the neutrino azimuthal energy dependence [62]. The measurement of the azimuthal dependence of atmospheric neutrinos has been carried out by the Super-Kamiokande experiment [63], and a comparable measurement by DUNE could potentially be done with a significantly smaller data set and serve as a valuable early demonstration that the detector is capable of achieving high resolution measurements. This validation would be particularly important as more data is acquired and we attempt to discern other features from the measured flavor-energy-angle dependent oscillograms. For a particular bin of zenith angle, flavor, and energy, neutrino oscillation probabilities are independent of neutrino azimuthal angle, and flux calculations predict significant non-isotropies resulting from the geomagnetic shielding of low energy primaries. Figure 18 shows the ratio of Honda and Bartol flux predictions for muon neutrinos, as a function of zenith angle, azimuthal angle, and energy.

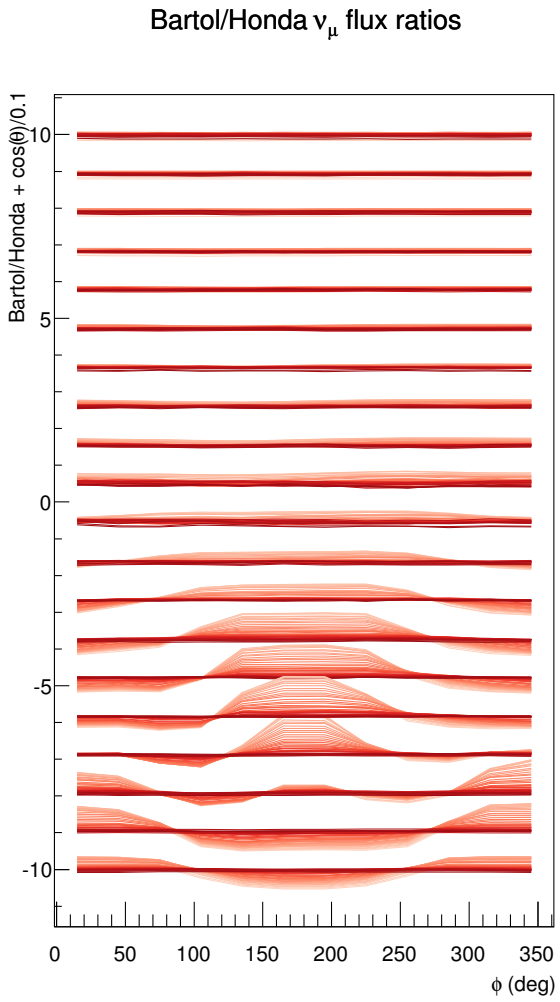

Figure 18: Ratio of the Honda to Bartol flux calculation for muon neutrinos. Each band corresponds to the flux in a zenith angle bin of $\cos(\theta) = 0.1$, with downgoing neutrinos in the top band. Within each band are ten colored lines corresponding to increasing neutrino energies in 1 GeV bins from 0 to 10 GeV. From [62].

In this calculation, the flux driver used for the Bartol flux did not include azimuthal information, so the flux was taken to be isotropic in azimuthal angle. The plot demonstrates several features the East/West asymmetry for incoming neutrinos, and the relatively large fluxes of low energy neutrinos arriving from the Earths polar regions (as seen from a detector at the Homestake site).

This results from the fact that the magnetic shielding of the Earth is smallest at the poles. Figure 19 shows the true azimuthal angle distribution for atmospheric neutrino interactions with $\cos(\theta) < -0.7$, a region covering the South pole, from a sample of 500k simulated atmospheric neutrino interactions. The black points correspond to events with $E_\nu < 0.5$ GeV, red to $E_\nu > 3$ GeV, clearly showing the large variation for low energy neutrinos. Figure 20 shows the expected DUNE azimuthal angle resolution for $E_\nu < 1$ GeV interactions, which is clearly sufficient for resolving these expected features in the atmospheric flux.

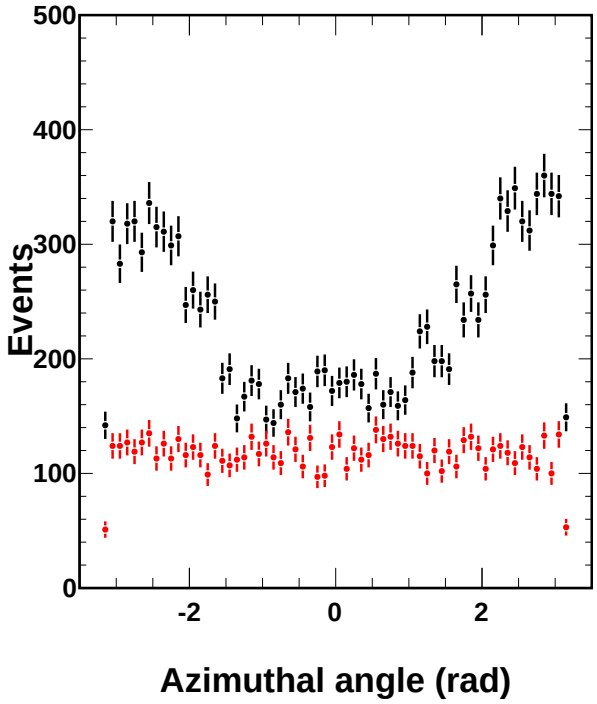

Figure 19: True azimuthal angle distribution for atmospheric neutrino interactions with $\cos(\theta) < -0.7$, from a sample of 500k simulated atmospheric neutrino interactions [64]. $E_\nu < 0.5$ GeV (black) and $E_\nu > 3$ GeV (red).

4.4 Cosmic Rays and Cosmogenics

4.4.1 Muon generator: MUSUN

The muon generator for the DUNE far detector (FD) is based on the well-known muon simulation code MUSUN (MUon Simulations UNderground) [65, 66]. The code uses the results

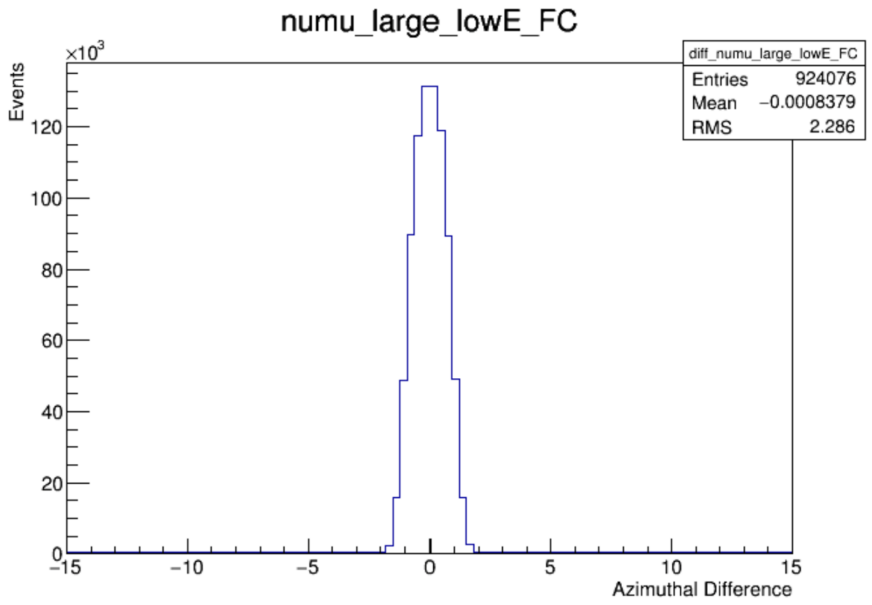

Figure 20: Azimuthal angle resolution for ν_μ CC interactions with $E_\nu < 1$ GeV [62].

of muon transport through rock carried out with the MUSIC code [67, 68, 65] convolved with the muon spectrum at sea level for different zenith angles. The MUSUN code, originally written as a standalone package in FORTRAN, has been converted into a module in LArSoft (written in C++) and tested with respect to the original code.

The MUSUN code, as currently adapted for DUNE, samples muons around an underground laboratory located near the Ross shaft and expected to host one of the 10 kt modules of the future DUNE experiment. The global coordinates of the location: latitude = 44°20′45.21" N, longitude = 103°45′16.13" W. The rock composition has been taken from Refs. [69, 70]. Many rock samples have been measured and the average rock composition has been calculated as $< Z >= 12.09$ and $< A >= 24.17$ [69, 70]. The average density of rock was assumed to be 2.70 g/cm^3 [70] in the MUSIC simulation for SURF. Other measurements suggest that the density may be larger (2.8-2.9 g/cm^3 [71, 72]). The density can be changed in the MUSUN muon generator if required. The slant depth distribution for the 4850 ft level at SURF was calculated from the CGIAR digital elevation model [73].

The measurement of the muon flux at SURF (in the Davis' campus near the Yates shaft) was performed by the active veto system of the Davis' experiment [74] giving the value of $(5.38\pm0.07)\times10^{-9}$ cm^{-2}s^{-1}sr^{-1} for the vertical flux (the measured fraction of multiple muons has been added to the single muon flux as given in Ref. [74], so the systematic uncertainty for this value may be of the order of a few %). The result agrees very well with the vertical flux calculated by MUSIC/MUSUN (in this case the coordinates for the Davis' campus were used to calculate the slant depth distribution for MUSUN): 5.18×10^{-9} cm^{-2}s^{-1}sr^{-1}. A recent measurement of muons in the Davis' campus has been carried out with the active veto system of the Majorana demonstrator [75] giving the value of $(5.04 \pm 0.16) \times 10^{-9}$ cm^{-2}s^{-1} for the total (not vertical) muon flux, in reasonable agreement with a calculation with MUSIC/MUSUN for a close location (also in Davis campus but LUX/LZ location rather than Majorana demonstrator hall): 6.16×10^{-9} cm^{-2}s^{-1}. Given a small difference between

the recent measurement and simulations (that can be due to different locations) we estimate the systematic uncertainty in calculating the muon flux in our model as 20%. We emphasize the need for an accurate measurement of the muon flux in the DUNE cavern(s) to normalize simulations.

Figure 21 (left) shows the profile of the surface above the proposed location of the far detector (center of the map). The lines drawn from the center divide each quadrant into 4 angles of equal size, 22.5°, to guide the eye. Muon azimuth angle distribution is plotted in Figure 21 (right). The vertical lines show approximately the division of quadrants on the left figure where the azimuth angle is calculated from East (pointing to the right on the left figure). Moving from East to North and further on counterclockwise on the map on the left, one can see how the dips and peaks on the surface profile correspond to peaks and dips in the number of muons on the graph on the right.

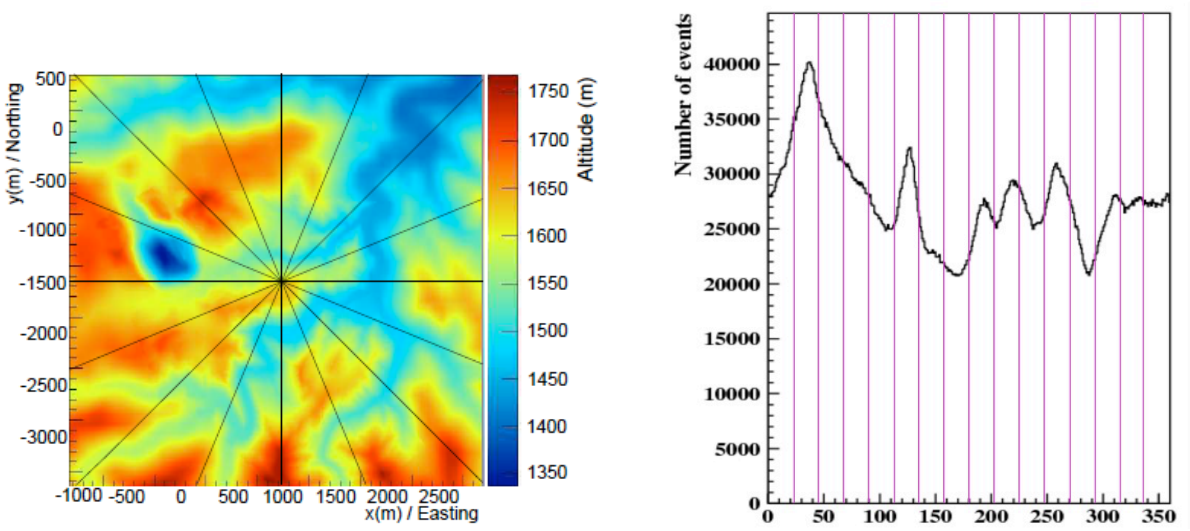

Figure 21: Left – surface profile above the proposed location for the far detector (center of the map). The lines drawn from the center divide each quadrant into 4 angles equal in size: 22.5° to guide the eye. Right – muon azimuth angle distribution. The vertical lines show the division of quadrants on the left figure where the azimuth angle is calculated from East (pointing to the right on the left figure). Moving from East to North and further on counterclockwise on the map on the left, you can see how the dips and peaks on the surface profile correspond to peaks and dips in the number of muons on the graph on the right.

The parameters of the muon flux are given in Table 2 for simulations carried out with MUSIC/MUSUN. These particular simulations did not include the cavern geometry and assumed spherical geometry for an imaginary detector.

The normalization of the muon flux or rate is done for a specific point underground where the slant depth distribution was calculated. This implies that the cavern/laboratory is relatively small and the muon flux is the same everywhere across the cavern (plus the rock where the box for muon sampling is extended to). For the cavern(s) where the far detector will be located the difference in muon intensities in different locations does not exceed 10%.

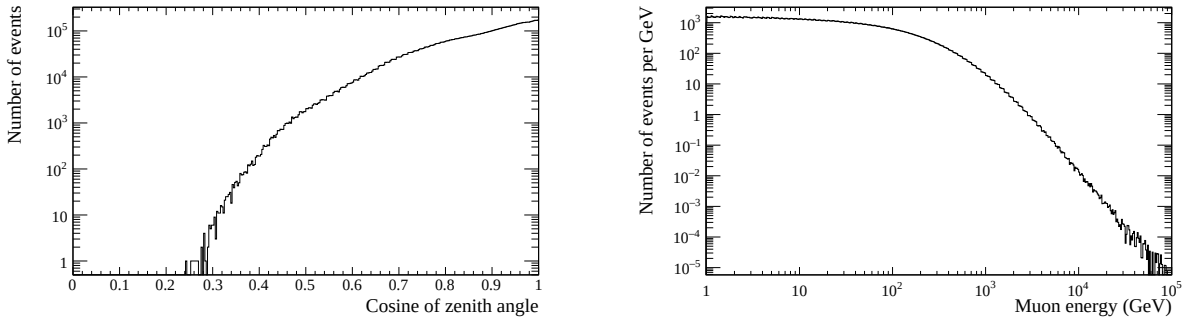

Figure 22: Left – zenith angle distribution of muons as simulated with the MUSUN muon generator for DUNE, right – energy spectrum of muons at the DUNE site.

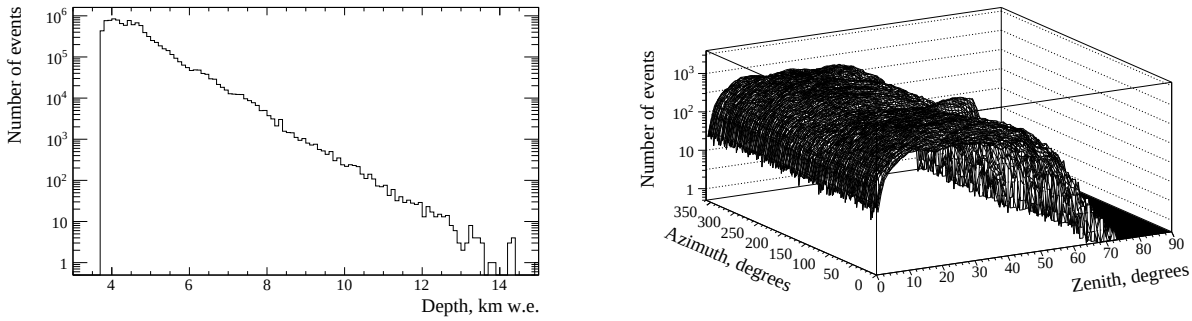

Figure 23: Left – distribution of muons according to the distance to the surface that they have travelled through, right – distribution of the number of muons as a function of zenith and azimuth angles.

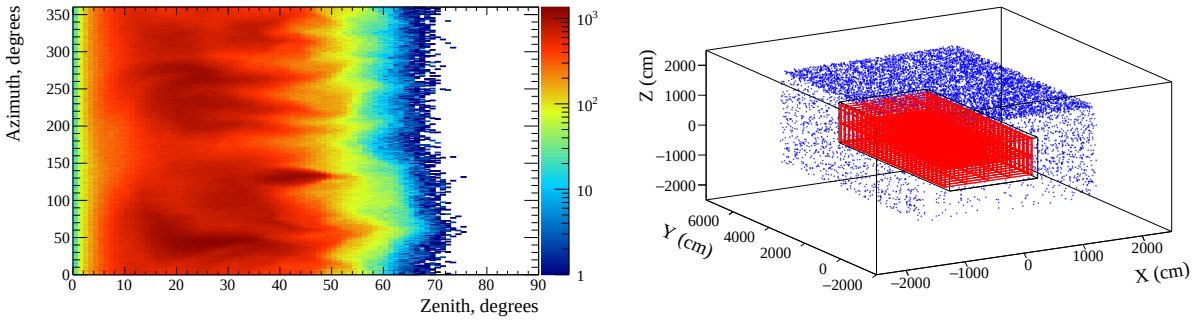

Figure 24: Left – Colour plot of the number of muons as a function of zenith and azimuthal angles, right – muon positions as sampled on the surface of the box around the cavern with the cryostat.

Table 2: Muon flux parameters as calculated with MUSIC/MUSUN.

Total flux, $cm^{-2}s^{-1}$	Mean E_μ, GeV	Mean slant depth, m w. e.	Mean θ, deg.
5.66×10^{-9}	283	4532	26

In the MUSUN generator for DUNE muons are sampled on a surface of a box that encompasses the lab, about 7 m of rock above the cavern and 5 m of rock beside and below the cavern. The rock is included to make sure that muon-induced cascades initiated above and around the cavern, have enough of space to fully develop and produce, in simulations, potentially dangerous secondaries, whereas the muon itself may not cross the active volume of argon. The size of the box is $74.43 \times 29.54 \times 30.18$ m^3 (length×width×height). The size of the cryostat has been assumed to be $61.62 \times 14.94 \times 13.58$ m^3 (length×width×height). Muons are sampled according to their energy spectrum for a particular zenith and azimuthal angles, sampled in its turn from the angular distribution obtained using the MUSIC code. The size of the box (the probability of a muon to cross a particular surface of the box) is taken into account when generating muons. All energy spectra and angular distributions are stored on disk and read during the initialization at the beginning of each simulation run. The generator is fully integrated into `larsim` (within the LArSoft built upon *art* framework) since `v04_24_00`. The module is located at `larsim/larsim/EventGenerator/MuonPropagation/MUSUN_module.cc`. The configuration fcl file is in the same directory and is called `MUSUN.fcl`. MUSUN is run with the fcl file `prodMUSUN_dune10kt.fcl`.

The muon rate through the surface of this box is 0.1579 Hz. This rate is used later to normalize the muon-induced background event rate in DUNE. (Note that the overall uncertainty in the muon flux is about 20%, see above.) The rate of muons passing through the active volume of liquid argon is 0.053 Hz so about 30% of muons generated on the surface of the box are passing through active argon (in fact having the track length of more than 1 m in the active volume.

Figures 22, 23 and 24 show various distributions of muons obtained with the MUSUN generator as incorporated into `larsim`.

4.4.2 Muon background for proton decay

There are a large number of proton decay modes where the sensitivity of DUNE may be comparable to or even exceeding that of Super-K/Hyper-K. The mode which is usually considered to be the 'golden' mode for the discovery at DUNE is: $p \to K^+\bar{\nu}$. This mode is dominant in most supersymmetric GUTs, many of which also favor other modes involving kaons in the final state. The decay modes with a charged kaon are unique for LAr experiments; since stopping kaons have a higher ionization density than pions or muons with the same momentum, a LArTPC could detect them with extremely high efficiency. In addition, many final states of K^+ decay would be fully reconstructable in a LArTPC. See Table 1 for a list of the promising nucleon decay modes.

The key signature for $p \to K^+\bar{\nu}$ is the presence of an isolated charged kaon (which would also be monochromatic for the case of free protons, with the momentum $p \approx 340$ MeV).

The kaon emerges intact from the nucleus with 97% probability. The kaon momentum is smeared by the proton's Fermi motion and shifted downward by re-scattering [76]. The kaon emerging from this process is below Cherenkov threshold in water, therefore a water Cherenkov detector would need to detect it after it stops, via its decay products. In LArTPC detectors, the K^+ can be tracked and identified via detailed analysis of its energy loss profile, and its kinetic energy measured by range. Additionally, all decay modes can be cleanly reconstructed and identified, including those with neutrinos, since the decaying proton is essentially at rest. With this level of detail, it is possible for a single event with an isolated kaon of the right momentum originating from a point within the fiducial volume, to provide overwhelming evidence for an observation of a proton decay.

The background for a proton decay search comes from atmospheric muons and neutrinos. If a muon passes through the detector, then the event can easily be reconstructed as a background muon-induced event and rejected. The current design of DUNE far detector suggests that the rate of muons passing through active LAr of a single module is about 0.05 Hz. Assuming a maximum drift time (∼few ms) for an event, rejecting all events with muons crossing the active volume of the TPC will result in less than 0.1% of dead time. Thus, only events with muons not crossing the active LAr volume may contribute to the background. Among these events the main danger comes from neutral kaons produced outside the TPC and undergoing inelastic scattering (primarily charge exchange) inside the TPC resulting in a single positive kaon detected. Figure 25 shows a schematic for such background event. Potential cosmogenic backgrounds with other particles mis-reconstructed as kaons have not yet been assessed, and are pending improvements in reconstruction algorithms.

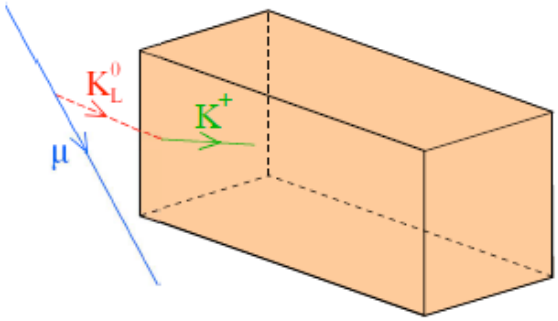

Figure 25: A schematic showing a potential background events with a muon evading the detector but producing a neutral kaon that produces a positive kaon in its turn via charge exchange reaction. Positive kaon decay products are not shown. Taken from [73].

We have carried out initial simulations of muon-induced background in one DUNE module with a fiducial mass of about 10.4 kt. By now (August 2016) 4×10^8 muons have been simulated and events in the detector analysed, corresponding to 80.32 years of live time of running one DUNE module. Only 'truth' parameters have been processed due to CPU time limitations and the full reconstruction chain not being fully ready for reconstructing large cosmic-ray events. We start by identifying potential backgrounds as events with a charged kaon in the TPC active volume (positive and negative kaons cannot easily be separated in

LAr) whereas a primary muon misses the detector. The following cuts have been applied to reject muon-induced events: (i) no muon is in the detector active volume (the track length of the initial muon is less than 20 cm), (ii) the K^+ is fully contained within the fiducial volume ($>$ 2 cm from any TPC wall, similarly no energy deposition with 2 cm from the walls), (iii) the energy deposition from the K^+ and its descendants (excluding decay products) is $<$ 250 MeV (this includes smearing of the energy deposition due to energy resolution and nuclear effects in proton decay), (iv) the total energy deposition from the K^+, its descendants and decay products is $<$ 1 GeV, (v) energy deposition from other particles in the muon-induced cascade (i.e. excluding the energy deposition from the positive kaon, its descendants and decay products) is $<$ 30 MeV (otherwise this additional energy deposition can be clearly identified as such and the event would be rejected as a background).

Figure 26 (left) shows the spectra of energy depositions from charged kaons after the discussed cuts are applied. The three events shown by a dashed blue histogram are rejected after the additional cut on the energy deposition from other particles is applied. Figure 26 (right) shows the scatter plot of the kaon energy deposition versus that of other particles (excluding kaon and its decay products) for background events. For a proton decay event the energy deposition of other particles (x-axis on this plot) should be 0 but we have allowed for some hits to be missed or attributed to radiogenic background, hence imposed an upper limit of 30 MeV on this energy deposition. The 3 events shown as red circles on the right plot (also shown as dashed blue histogram on the left plot) are rejected because the energy deposition from other particles exceeds 30 MeV. A few events inside the region of interest are rejected because of the energy deposition within 2 cm of the walls (particles are entering the active volume from outside). Note that rejecting some of these events require good timing resolution (light detection) to identify the correct start of the event. The study of the proton decay detection efficiency with a current design of the DUNE far detector is underway. Our previous studies with a simplified cylindrical geometry of the cryostat show that 10 cm cut around the walls reduce the detection efficiency by less than 2% [77]. As a result of the analysis no event survived all the above cuts, resulting in an upper limit (at 90% CL) on the muon-induced background rate of 0.0029 events/kt/year.

Figure 27 (left) shows the 2D-distribution of simulated events from proton decay mode $p \to K^+\bar{\nu}$. The x-axis shows the energy deposition from kaon decay products whereas the y-axis shows the energy deposition from the positive kaon. Almost all kaons deposit less than 250 MeV inside the active volume which justifies the choice of cuts for background events. Note that the energy deposition from other particles (excluding kaons and the products of their interactions and decays) should be zero for this mode of proton decay which serves as a good selection criterion to reject background events (currently required to be less than 30 MeV but can be tuned further). Figure 27 (right) shows a similar distribution for cosmogenic background before the discussed cuts are applied. The distribution is different from that for proton decay events due to the fact that background kaons are mostly entering the active volume from outside.

Simulated cosmic-ray events are stored on disk and can be analyzed to determine potential background for other nucleon decay modes. They will also be processed further through the whole data collection, track reconstruction and particle identification chain.

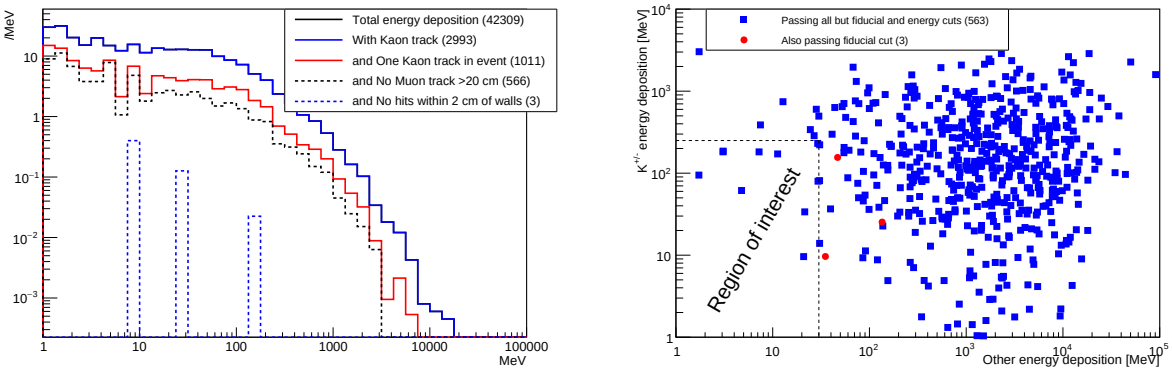

Figure 26: Left – spectra of energy depositions from kaons after various cuts, right – scatter plot of a kaon energy deposition vs energy deposition of other particles (excluding kaon and its decay products) for background events.

4.4.3 Cosmic-ray event reconstruction

Reconstruction in LArTPCs is a complex process requiring numerous steps from hit reconstruction to hit disambiguation, clustering and ultimately combining clusters into tracks. As the process has multiple steps there are a suite of options at each stage, for this study though the following modules have been used:

- Gaussian hit finder,
- Disambiguation algorithm tuned for the far detector,
- Line cluster, clustering algorithm,
- Projection matching tracking algorithm (PMTrack).

Many of the reconstruction algorithms were tuned and developed for significantly smaller detectors than the far detector, such as the 35 ton prototype. This means that tuning of the algorithms is required to achieve a high reconstruction efficiency. This tuning was achieved through a detailed study of 100 simulated muons using the MUSUN generator discussed above. Properties of the reconstruction to be improved were identified and the tuning required to do so is illustrated below.

Two views are shown for each event, one called 'Ortho3D' which has two dimensional representations of the detector in the XZ and YZ planes. Within each plane the TPCs are shown as regions contained within gray dashed lines. The reconstructed tracks are shown as bold colored lines, and are labeled with their reconstructed track number which increases from 0. The second view is that of the wire planes for a given TPC. The TPC number is shown on the left hand side of the image. Three wire planes are visible, which in descending order are the collection plane, the U induction plane and the V induction plane. The plot for each plane shows the wire number on the plane (increasing from 0) against TPC tick (in

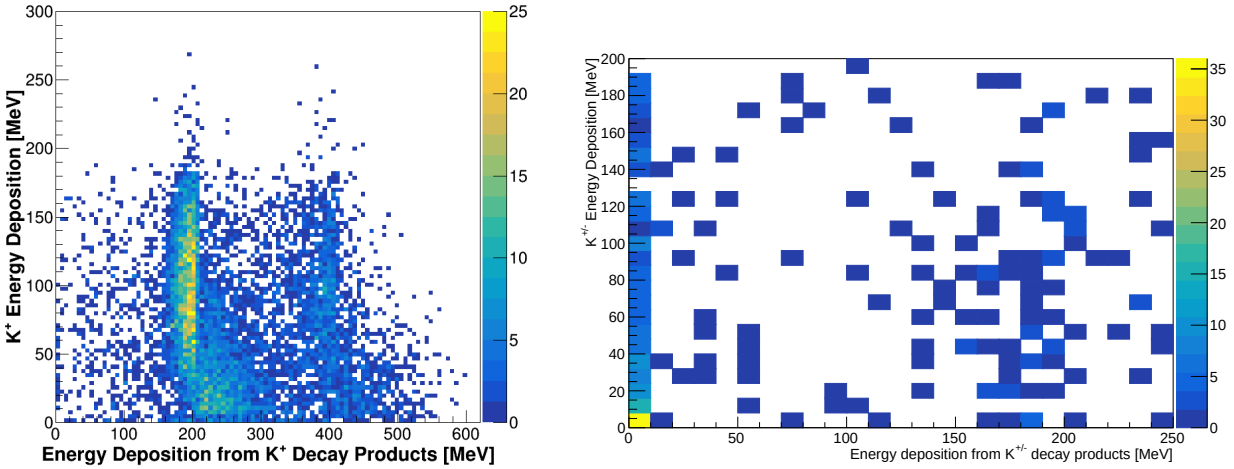

Figure 27: Distribution of simulated events from proton decay mode $p \to K^+\bar{\nu}$. The x-axis shows the energy deposition from kaon decay products whereas the y-axis shows the energy deposition from the positive kaon.

units of 500 ns). The charge deposited on a wire at a given time is shown using a color scale shown on the right of each plane. At the bottom of the image is a plot showing the charge deposited on a given wire for a range of times, the blue line shows the de-convoluted signal and the orange lines displays the reconstructed hits.

Many through-going muons were originally reconstructed as multiple tracks as opposed to a single track. These track separations regularly occurred as a muon crossed a TPC boundary, where there is an ∼5 cm area of un-instrumented LAr. This meant that the track sections were not merged into a single track. Upon allowing for tracks to be merged with larger separations many of the un-merged tracks are observed to be successfully merged. An example of a merged through-going muon is shown in Figure 28.

Another reason for split tracks is due to high energy delta-rays. These large energy depositions create additional large clusters to be reconstructed around the main track causing the track to be split. Further study is required to mitigate the effect of high-energy delta-rays, an example of which is shown in Figure 29.

High-energy muons can produce large showers. These large energy depositions cause many short ($\leq$10 cm) tracks to be reconstructed. The effect of this is that the reconstruction appears to perform badly due to a large excess of reconstructed tracks at short track lengths, however the through-going muon track is often fully reconstructed. An example of a high-energy shower is shown in Figure 30.

Occasionally hits within TPCs can be successfully reconstructed into clusters which are not merged to produce tracks. It was observed that this is due to one or more of the clusters

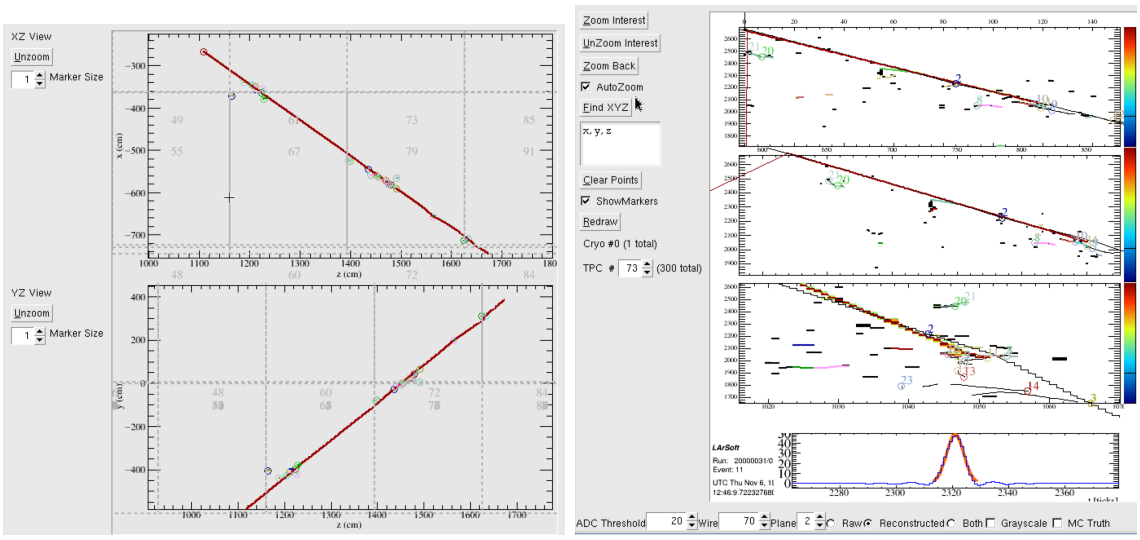

Figure 28: An example of a well reconstructed through going muon track. Left image shows the Ortho3D view, right image shows the LArSoft wire plane display.

being incorrectly identified as a delta-ray causing the track to be reconstructed outside the TPC and being discarded. The effect of this was greatly reduced by allowing for a greater variation in TPC containment, however occasional examples can still be found. An example of an un-merged track is shown in Figure 31.

Reconstruction of kaons of the energy which would be observed in proton decay is being studied by the reconstruction working group and is not considered in here.

4.4.4 Cosmogenics and Requirements for the Far Detector

Cosmic rays impose the following design requirements for the DUNE far detector modules:

1. Each 10 kton module will detect cosmic-ray muons at a rate of ∼0.05 Hz. The resulting signals are expected to dominate the data collected by the DUNE far detectors, and will therefore set requirements on the average data bandwidth and total data storage.

2. Cosmogenic backgrounds are of most concern to searches for nucleon decay. The work presented here investigates methods to reject these backgrounds. The study implies that good timing resolution for the start of each event, O(10 μs) or better, is necessary in order to properly define the fiducial volume for nucleon decay. Reducing potential dead volumes in the TPC is useful, although it is not as critical. A potential background from mis-reconstruction of cosmogenic backgrounds (without true kaons) as nucleon decay candidates requires additional study. Cosmogenic backgrounds for nucleon decay modes beyond the 'golden' mode ($p \to K^+\nu$) require further study.

3. Cosmic ray muons will likely serve a role in calibration of the DUNE far detectors, but it is not yet clear whether this imposes any addition detector design requirements beyond those already considered.

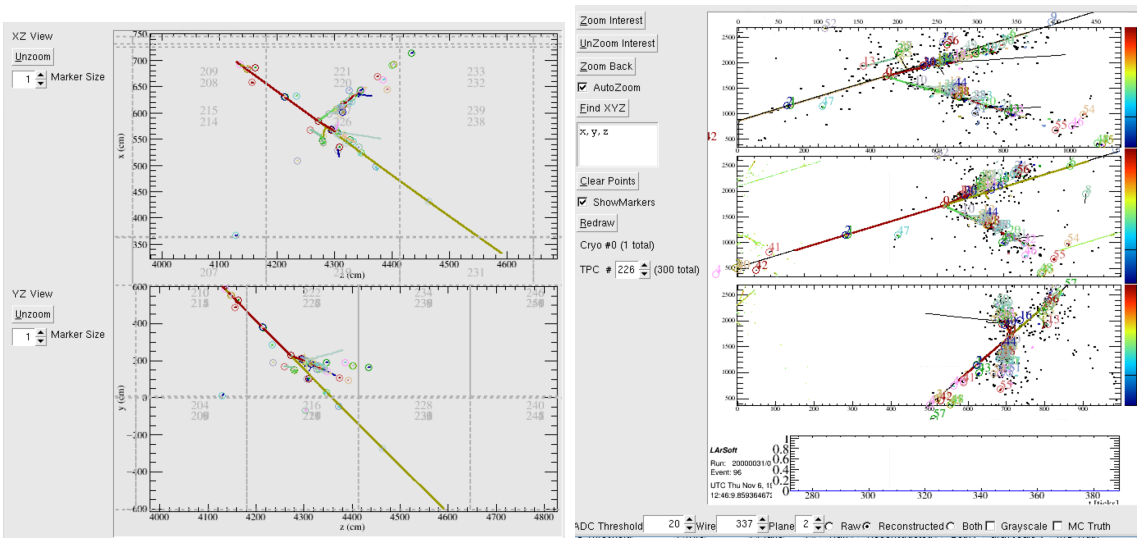

Figure 29: An example of a delta-ray causing a through-going muon to be split into two tracks. Left image shows the Ortho3D view, right image shows the wire plane display.

5 Long-baseline Physics Sensitivity Studies

5.1 Event Selection

A critical aspect of the long-baseline oscillation analysis is identification of the ν_μ and ν_e event samples. In the Fast Monte Carlo, which is currently used to determine the signal and background selection efficiencies used in GLoBES-based sensitivity calculations and as input to the DUNE oscillation fitters described below, the selection criteria are applied to reconstructed quantities, which are the result of applying a parameterized detector response to generator-level particles, at the individual particle level. For the full LArSoft Monte Carlo, a multivariate analysis has been developed to perform the ν_e and ν_μ signal selection using (mostly) reconstructed quantities.

The Fast MC event selection is fairly simple. Any event with a candidate muon, defined as a track longer than 2 m, is classified as ν_μ CC. Any event without a candidate muon, but with a candidate electron/positron, which is defined as an electromagnetic shower (EM) that is not consistent with a photon, is classified as a ν_e CC. An EM shower is classified as consistent with a photon if it begins 2 cm or more from the event vertex, or if it can be matched with another EM shower to reconstruct an invariant mass with 40 MeV of the π^0 mass. In a full analysis, the dE/dx of the initial portion of shower can discriminate between photon-like and electron-like showers; the efficiency for this selection is applied probabilistically in the Fast MC as a function of shower energy and hadronic-shower multiplicity, based on results from early Monte Carlo studies. Finally, to reduce background from neutral current and ν_τ in the ν_e CC-like sample, an additional discriminant is formed using reconstructed transverse momentum along with reconstructed neutrino and hadronic energy as inputs to a k-Nearest-Neighbor (kNN) machine-learning algorithm. Figure 5.1 shows the analysis sample detection times selection efficiencies for the various signal and background modes extracted from the Fast MC.

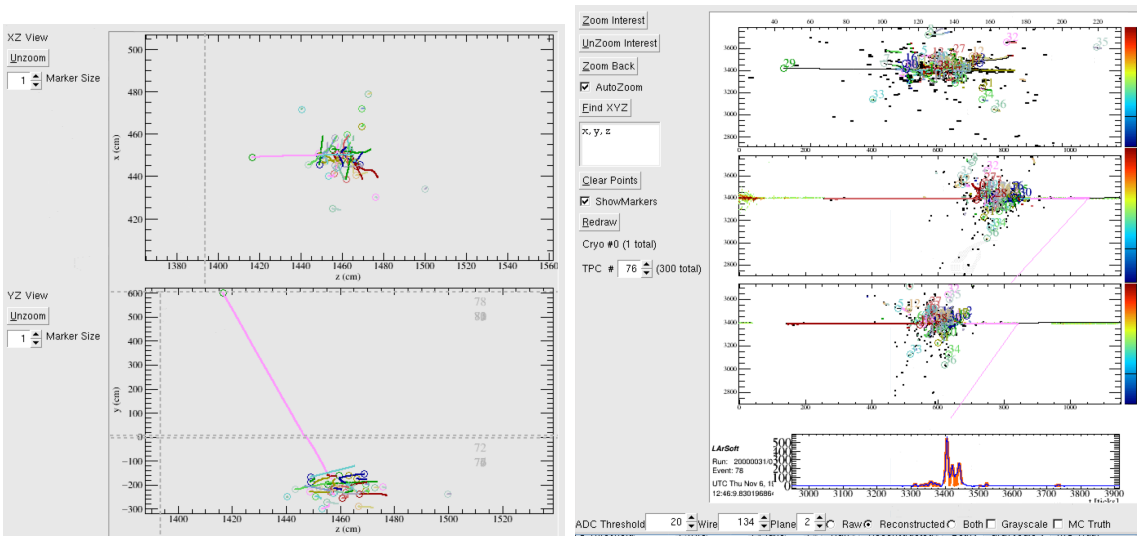

Figure 30: An example of a high-energy shower in the detector around a through going muon. Left image shows the Ortho3D view, right image shows the wire plane display.

To move beyond the probabilistic event selection used in the Fast MC, a multivariate analysis has been developed to perform ν_e and ν_μ event selection in LArSoft. ν_μ CC events are identified using a TMVA algorithm with input from the following variables: number of tracks, maximum track length, average track length, track dE/dx, signal fluctuation, transverse track profile, maximum fraction of charge in 5, 10, 50, and 100 wires, direction cosines of longest track, and fractional transverse energy. ν_e CC events are identified using a TMVA algorithm with input from the following variables: number of tracks, number of showers, maximum track length, average track length, track dE/dx, shower dE/dx, signal fluctuation, transverse track profile, maximum fraction of charge in 5, 10, 50 and 100 wires, direction cosines of the longest track and the highest energy shower, distance from neutrino vertex to shower vertex, fractional transverse energy, number of hits per wire in the shower, and shower length. The variables considered by the multivariate analyses are all extracted from automated reconstruction routines applied to DUNE LArSoft Monte Carlo, with the exception that "disambiguation cheating," which makes use of some truth information to perform the disambiguation, is used in the reconstruction. The left panel of Figure 5.1 shows the ROC curve for the ν_μ event selection and the right panel shows the ROC curve for the ν_e event selection. While this represents significant progress, the background rejection level has not yet reached the expectations set by the Fast MC studies described above. This is because the reconstruction is not sufficiently advanced to provide the expected discrimination; for example, shower dE/dx currently provides relatively poor discrimination against neutral current background for the ν_e CC event selection, even though this is expected to be a powerful discriminant. Work is ongoing to improve the reconstruction and re-evaluate the event selection.

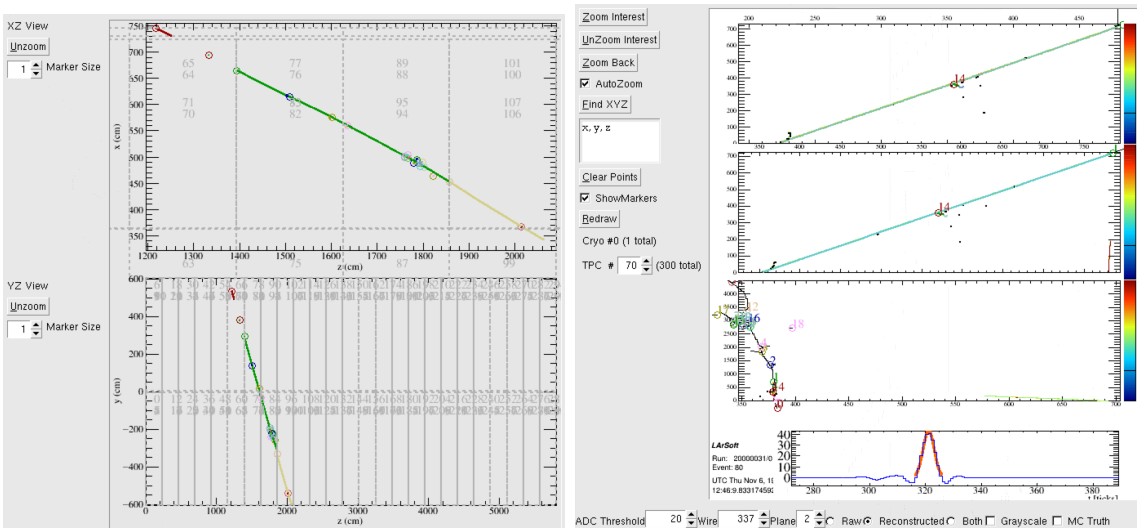

Figure 31: An example of an event where the merger of clusters has failed causing sections of track to be dropped. Left image shows the Ortho3D view, right image shows the wire plane display.

5.2 Oscillation Fits

Oscillation fitters are required to extracting measurements of physics parameters from the selected data sets. There are two oscillation fitters currently being developed for DUNE. VALOR, a neutrino fitting group first established in T2K, is able to perform fits to near detector data that provide constraints for other oscillation fitters and is also able to perform a joint fit to near and far detector data. The "Long-baseline Oscillation Analysis Fitter" (LOAF) fits far detector data and applies constraints based on separate near detector fits and/or external data.

5.2.1 VALOR

The current version of the VALOR DUNE fit is an intermediate step towards the implementation of the full joint ND-FD VALOR fit. It provides a constraint to the flux and cross-section systematic uncertainties, via the joint fit of neutrino flux and neutrino interaction parameters to Near Detector event samples. Eighteen samples are used in the fit, corresponding to nine final state topologies for forward horn current (FHC) and reverse horn current (RHC) modes. These samples are ν_μ CC broken down into 1-track QE enhanced, 2-track QE enhanced, $1\pi^+$, $1\pi^0$, $1\pi^+ + 1\pi^0$, and other, wrong-sign ν_μ CC inclusive, ν_e CC inclusive, and NC inclusive. This set of final-state topologies is not entirely aligned with generator-level event classifications. To compare these measurements with theory, one needs to build an ND event rate model. This model is built from the convolution of flux, interaction, and detector (acceptance) models, each of which have parameterized uncertainties. In VALOR, a simultaneous fit of neutrino flux and interaction parameters to ND samples is used to determine the values of these parameters, reduce their uncertainty, and obtain their correlations given the ND event rate constraint. In future revisions, the fully inclusive or other categories can be subdivided further to include neutrino-electron elastic scattering and

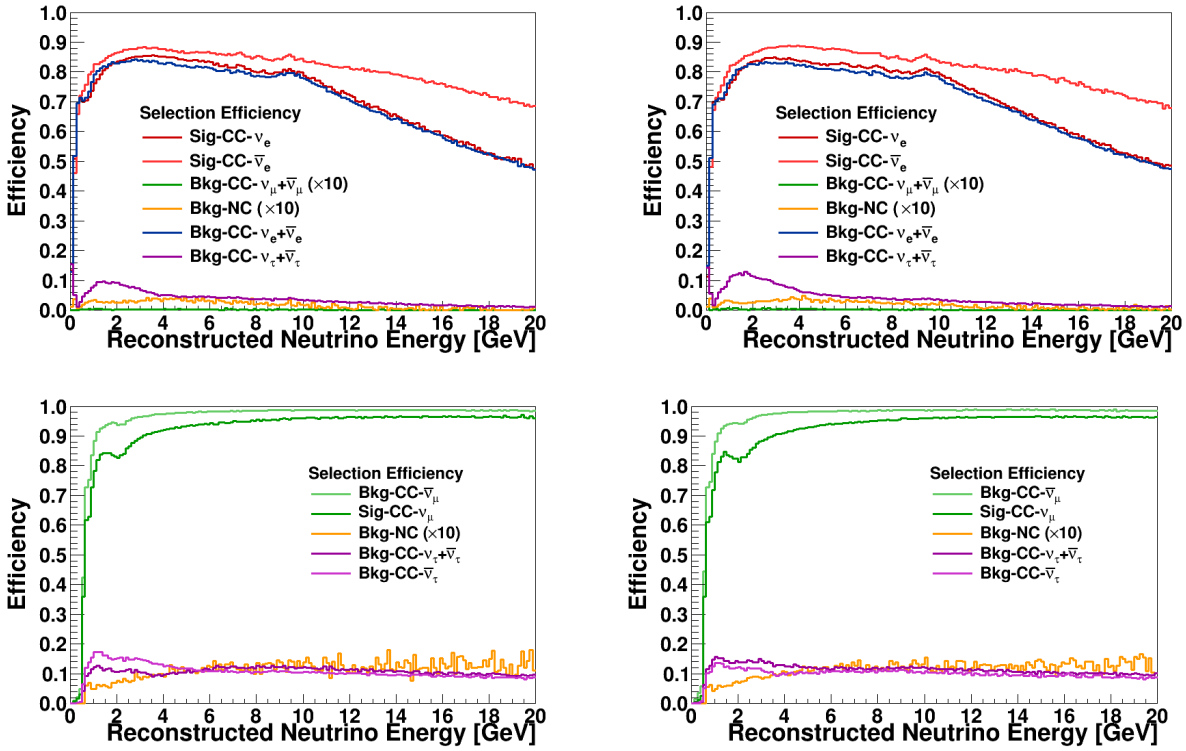

Figure 32: Analysis sample detection × selection efficiencies for the various signal and background modes extracted from the Fast MC and used as inputs to GLoBES. Top: Used in the ν_e appearance sample. Bottom: Used in the ν_μ disappearance sample. Left: Neutrino beam mode. Right: Antineutrino beam mode. The NC backgrounds (and ν_μ CC backgrounds for the appearance mode) have been increased by a factor of 10 for visibility.

inverse muon decay events, as well as 3-track Δ-enhanced, coherent pion and other samples that can provide degeneracy resolution and improve the sensitivity of this analysis.

Measurements of a set of physics parameters in the presence of systematic parameters are obtained by comparing the observed and expected reconstructed kinematic distributions for a series of samples. Two dimensions (E_{reco}, y_{reco}) are fit for the CC-like samples and one dimension (E_{vis}) is fit for the NC-like samples. Here, E_{reco} is the reconstructed neutrino energy, y_{reco} is the reconstructed inelasticity, and E_{vis} is the reconstructed visible energy. A binned likelihood-ratio method is typically used by VALOR. Most physics and systematic parameters in the VALOR fit come with prior constraints from external data; these constraints are applied using a Gaussian penalty term. In the current VALOR analysis, which provides a constraint of the prior flux and cross-section systematic uncertainties, near detector systematics are eliminated by profiling, as they are not correlated between the near and far detectors.

MC templates are binned in the same kinematic variables that are used for fitting. Separate templates are constructed for various true interaction modes; each template contains information on how the number of events, for each individual reconstructed bin, is distributed in a chosen space of true kinematic variables. In the current analysis, 52 MC templates cor-

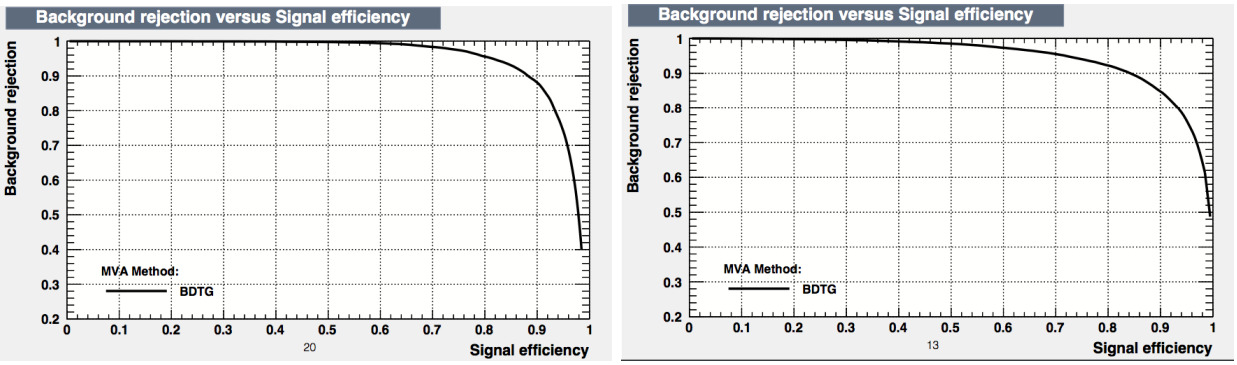

Figure 33: ROC curve, showing background rejection vs signal efficiency, for the ν_μ CC event selection (left) and the ν_e CC event selection (right).

Table 3: 52 Monte Carlo templates used by the VALOR fit to near detector data

1. ν_μ CC QE	14. $\bar{\nu}_\mu$ CC QE	27. ν_e CC QE	40. $\bar{\nu}_e$ CC QE
2. ν_μ CC MEC	15. $\bar{\nu}_\mu$ CC MEC	28. ν_e CC MEC	41. $\bar{\nu}_e$ CC MEC
3. ν_μ CC $1\pi^\pm$	16. $\bar{\nu}_\mu$ CC $1\pi^\pm$	29. ν_e CC $1\pi^\pm$	42. $\bar{\nu}_e$ CC $1\pi^\pm$
4. ν_μ CC $1\pi^0$	17. $\bar{\nu}_\mu$ CC $1\pi^0$	30. ν_e CC $1\pi^0$	43. $\bar{\nu}_e$ CC $1\pi^0$
5. ν_μ CC $2\pi^\pm$	18. $\bar{\nu}_\mu$ CC $2\pi^\pm$	31. ν_e CC $2\pi^\pm$	44. $\bar{\nu}_e$ CC $2\pi^\pm$
6. ν_μ CC $2\pi^)$	19. $\bar{\nu}_\mu$ CC $2\pi^0$	32. ν_e CC $2\pi^0$	45. $\bar{\nu}_e$ CC $2\pi^0$
7. ν_μ CC $1\pi^\pm + 1\pi^0$	20. $\bar{\nu}_\mu$ CC $1\pi^\pm + 1\pi^0$	33. ν_e CC $1\pi^\pm + 1\pi^0$	46. $\bar{\nu}_e$ CC $1\pi^\pm + 1\pi^0$
8. ν_μ CC coherent	21. $\bar{\nu}_\mu$ CC coherent	34. ν_e CC coherent	47. $\bar{\nu}_e$ CC coherent
9. ν_μ CC other	22. $\bar{\nu}_\mu$ CC other	35. ν_e CC other	48. $\bar{\nu}_e$ CC other
10. ν_μ NC $1\pi^\pm$	23. $\bar{\nu}_\mu$ NC $1\pi^\pm$	36. ν_e NC $1\pi^\pm$	49. $\bar{\nu}_e$ NC $1\pi^\pm$
11. ν_μ NC $1\pi^0$	24. $\bar{\nu}_\mu$ NC $1\pi^0$	37. ν_e NC $1\pi^0$	50. $\bar{\nu}_e$ NC $1\pi^0$
12. ν_μ NC coherent	25. $\bar{\nu}_\mu$ NC coherent	38. ν_e NC coherent	51. $\bar{\nu}_e$ NC coherent
13. ν_μ NC other	26. $\bar{\nu}_\mu$ NC other	39. ν_e NC other	52. $\bar{\nu}_e$ NC other

responding to the true interaction modes shown in Table 3 are constructed for each of the eighteen fit samples. The nominal predictions are varied using the parameterized uncertainties of the flux, neutrino interaction and detector model. The VALOR DUNE fit provides with best-fit values and correlations between all constrained parameters. Since the near detector provides an event rate constraint, constrained flux and cross-section parameters become anti-correlated. The main output of the current analysis is a 156×156 covariance matrix for each proposed DUNE near detector design, which is used to provide constraints for the far detector fit. Work on a full fit to combined near detector and far detector data is ongoing.

5.2.2 LOAF

The inputs to LOAF are far detector event spectra, flux and cross-section constraints from a VALOR fit to near detector data, and constraints on far-detector systematic uncertainties. The far detector spectra are taken either from a Fast Monte Carlo (Fast MC) or the full LArSoft simulation and analysis. Currently Fast MC inputs are used because reconstruction

of the full Monte Carlo is still under development, but care has been taken to define a common data format so that different types of simulation may be used interchangeably.

The LOAF fitter works by using prebuilt signal and background histograms combined with response functions which encode the information needed to alter those histograms given a particular set of fit parameter values. Since oscillation probabilities are a function of true neutrino energy and species, template histograms of true neutrino energy broken out by species are required as inputs. Smearing functions are used to convert the oscillated true neutrino energy spectra to reconstructed neutrino energy spectra. Systematics fluctuations are applied either to the true energy spectrum before smearing, in the case of flux, cross-section, and nuclear models uncertainties, or to the reconstructed energy spectra, in the case of reconstruction, efficiency, and other uncertainties from detector effects. These fluctuations are applied via response functions which provide the relevant spectral distortions as functions of systematics (fit) parameter changes. Parameter variations from nominal are used to determine penalty terms in the fit χ^2. The results of the VALOR ND fits are propagated to the LOAF fitter via a covariance matrix that gives the covariance of the ensemble of fit parameters that describe the uncertainty on the predicted event rate at the FD. Detector response systematics for the NDs have been marginalized and are not propagated. The constraints on the fit parameters are enforced through a penalty term calculated from the covariance matrix. Additional fit parameters are used to allow the best-fit value of each parameter to vary between samples. The statistical limit of the constraint on each parameter is estimated and used to set the allowed 1-sigma variation of that parameter in all other samples. Each parameter is also allowed to vary based on theoretical limits on uncertainty in the cross section ratios: ν_e/ν_μ, ν_τ/ν_μ, $\bar{\nu}/\nu$, and NC/CC.

The LOAF fit χ^2 assumes Poisson probability distributions for event counts and Gaussian probability distributions for the priors used in penalty terms. In the case of correlated priors a covariance matrix is used to determine the penalty term. The formulation is consistent with the one used in the VALOR ND fits. The χ^2 is minimized by the MIGRAD algorithm in MINUIT2 as implemented in ROOT or used by a Metropolis-Hasting algorithm in a Markov Chain Monte Carlo (MCMC) method, allowing comparison of results between the two approaches. In the minimization approach, the minimum χ^2 along with the set of best-fit parameters are reported.

For the purposes of a sensitivity study "mock data" must be generated. There are two classes of mock data used. The first is the most probable data, often referred to as the Asimov data set. This is created by taking the "true" value of each parameter is the nominal value from the simulation. This includes both systematic parameters and event rates. The second class of mock data are toy MC data sets in which the "true" values of each parameter are chosen at random based on the prior probability distributions. Again this applies for both systematic parameters and event rates, so takes into account statistical variations. In either case, since this is a hypothesis testing scheme, the parameter(s) of interest is set to a specific value which is different from than the nominal value, and not randomly generated. Asimov data set studies can be performed with a single fit; however special care must be taken to ensure correlations between data sets are properly considered. Toy MC data sets require a series of fits and the results are given by examining the ensemble of fit results.

The LOAF fitting framework is currently working and producing results that seem reasonable. Work is ongoing to validate the results against the GLoBES-based sensitivity studies

presented in the DUNE CDR. Remaining work includes implementation of detector systematics, implementation of uncertainty in the near/far flux ratio, implementation of correlations between oscillation parameter priors, technical details of the interface with VALOR, and comparisons between the MCMC and χ^2 minimization techniques.

6 Detector Optimization Studies

6.1 Wire Spacing and Wire Angle Studies

LArTPCs provide excellent spatial and calorimetric resolutions for measuring the properties of neutrino interactions above a few MeV. It is important to optimize the TPC design in order to maximize the physics sensitivities. In this section, we describe the Monte Carlo (MC) study of detector optimization, focusing on the impact of the TPC wire spacing and wire angle on the physics sensitivities.

The studies were done using the MC files produced in the MCC6.0 production [5]. The details of the simulation and reconstruction software using in this MC production can be found in Ref [78].

6.1.1 Tracking Efficiency

The detection and identification (ID) of particles is a critical component of DUNE's physics program, as it impacts the ability of reconstruct neutrino events and other interactions. In addition, a vast number of ID algorithms relay on track reconstruction for a given particle. In this section we will describe tracking efficiencies for charged particles from neutrino beam events. The simulation of such events follows the simulation chain; generation, its output is passed to a GEANT4 based detector simulation in which particles are tracked when they traverse in the LAr, the ionization electrons and scintillation photons are then digitized into raw signal (ADC) in the process known as detector simulation. Full details of the simulation process can be found in Ref. [78].

The reconstruction of events in the TPC is done by a series of reconstruction algorithms. First is the signal processing, then Gaussian hit finder, disambiguation (induction wires are wrapped in the TPC design), cluster formation (2D objects) and finally 3D track *(RS:) and vertex* reconstruction performed by the Projection Matching Algorithm (PMA). Full details of the reconstruction process can be found in Ref. [78]. Tracking efficiency studies were perform with `Neutrino_TrackingEff_module.cc` available at LArSoft/LArReco/ See [79].

Track reconstruction efficiency for a charged particle $x^{\pm}$ in *e.g.* neutrino beam interaction is defined as follows:

$$\epsilon_{x^{\pm}} = \frac{\text{CC events with a } x^{\pm} \text{ particle and with a reconstructed track}}{\text{CC events with a } x^{\pm} \text{ particle}}, \tag{11}$$

where $x^{\pm}$ can be a $\mu^{\pm}$, $\pi^{\pm}$, p, K^{+} and e^{-}, the last two cases are from proton decay events where $p \rightarrow K^{+} + \nu_{\mu}$. To be more specific, the denominator includes events where a $x^{\pm}$ particle was created and has deposited energy within any of the TPCs. The numerator includes events with a $x^{\pm}$ particle, and it has deposited energy within any of the TPCs with a reconstructed track associated to the $x^{\pm}$ particle. For cases where there is more than one

$\pi^{\pm}$ or protons, the leading particle will be used. The efficiency $\epsilon_{x^{\pm}}$ can be calculated as a function of energy, momentum, or angle. There are some cases when a charged particle has more than one track associated, which is caused by broken tracks. In order to choose the best track a metric called "completeness" is defined as

$$Completeness = \sum_{i}^{\text{track hits}} \frac{(\text{hit energy on track from a particle})_i}{\text{total hits energy from a particle}} \tag{12}$$

Another useful metric is track purity, which estimates the level of "hit contamination" from another particle; a metric called "purity" was defined as

$$Purity = \sum_{i}^{\text{track hits}} \frac{(\text{hit energy on track from a particle})_i}{\text{total hits energy on the tack}} \tag{13}$$

To calculate tracking efficiencies when there is more than one track associated to the same particle, the best track is chosen by choosing the track with the highest *Completeness*.

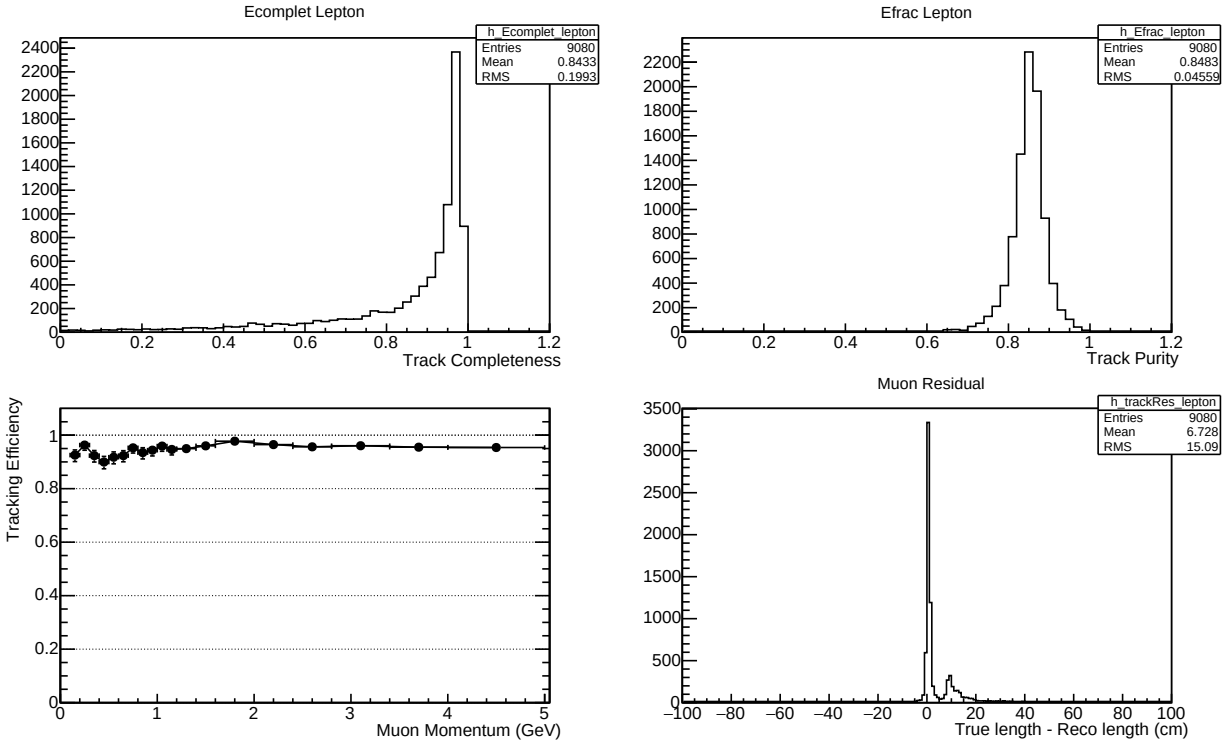

Figure 34: Track completeness (top left). Track purity (top right). Tracking efficiency (bottom left). Tracking residual (bottom right).

To test the tracking reconstruction in a isotropic way, we calculate the tracking efficiency for μ^- with uniform momentum distribution from 0.1 to 5.0 GeV, generated isotropically around the detector. The differences with a neutrino beam sample is that in the neutrino beam sample, most of the particles will travel forward due to the boost from the incoming

neutrino so the phase-space is reduced to mostly forward interactions. By using an isotropic sample we can test the reconstruction in all directions. Fig. 34 shows *Completeness*, *Purity*, tracking efficiency and track residual for μ^- using the particle cannon sample. The track residual is calculated using the particle length using only the trajectory points of the particle that are inside of a TPC (true length) and the reconstructed track length (reco length). the second peak in the residual is due to broken tracks either by delta rays or by the muon traversing through different TPCs. Looking at track completeness there are two main factors that can cause track completeness < 1: there are some cases where a muon traverses different TPCs and its track sometimes is not stitched properly so that it becomes two tracks (broken track); also delta rays can cause a track to be split. Both cases affect the residual and these examples appear in the residual as a second peak. In the case of track purity the peak is around $\sim$0.84; for most of these muon tracks there is 16% EM activity along the track, i.e. delta rays or Bremsstrahlung photons. Overall the tracking efficiency is 95.4%.

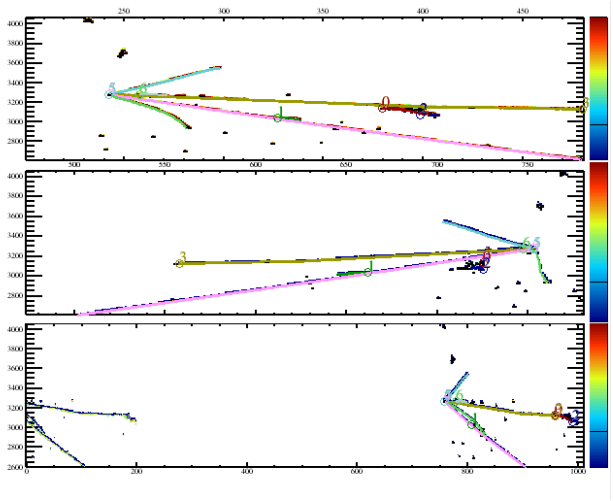

Figure 35: Event display for a CC ν_μ event in LAr (collection, induction1 and induction2 planes).

Figure 35 shows a fully reconstructed event produced in a CC ν_μ interaction in LAr. There are three panels (from top to bottom) collection plane, induction1 and induction2 plane. Figure 36 shows tracking efficiencies for μ^- produced in a CC ν_μ interaction in LAr. Tracking efficiencies are pretty much identical for beam and atmospheric events as well for neutrino and antineutrinos. In this document we will discussed only efficiencies for CC ν_μ interaction in LAr. Overall the tracking efficiency for muons is 98.2%, which is quite a remarkable performance from the pmttrack module. An interesting feature is that tracking efficiency drops at $\sim$ 70 degrees. This is mainly due to particles traveling almost parallel to the collection wires, causing one of the views to be missing in the reconstruction.

Figs. 37, 38 and 39 show π^-, π^+ and p tracking efficiencies and residuals respectively. In all cases the tracking efficiency drops at low momentum, more specifically, for protons at $\sim$70 MeV of kinetic energy and for pions at $\sim$ 100 MeV of kinetic energy. Due to the fact that LAr is a dense material, hadronic interactions make it more challenging to reconstruct

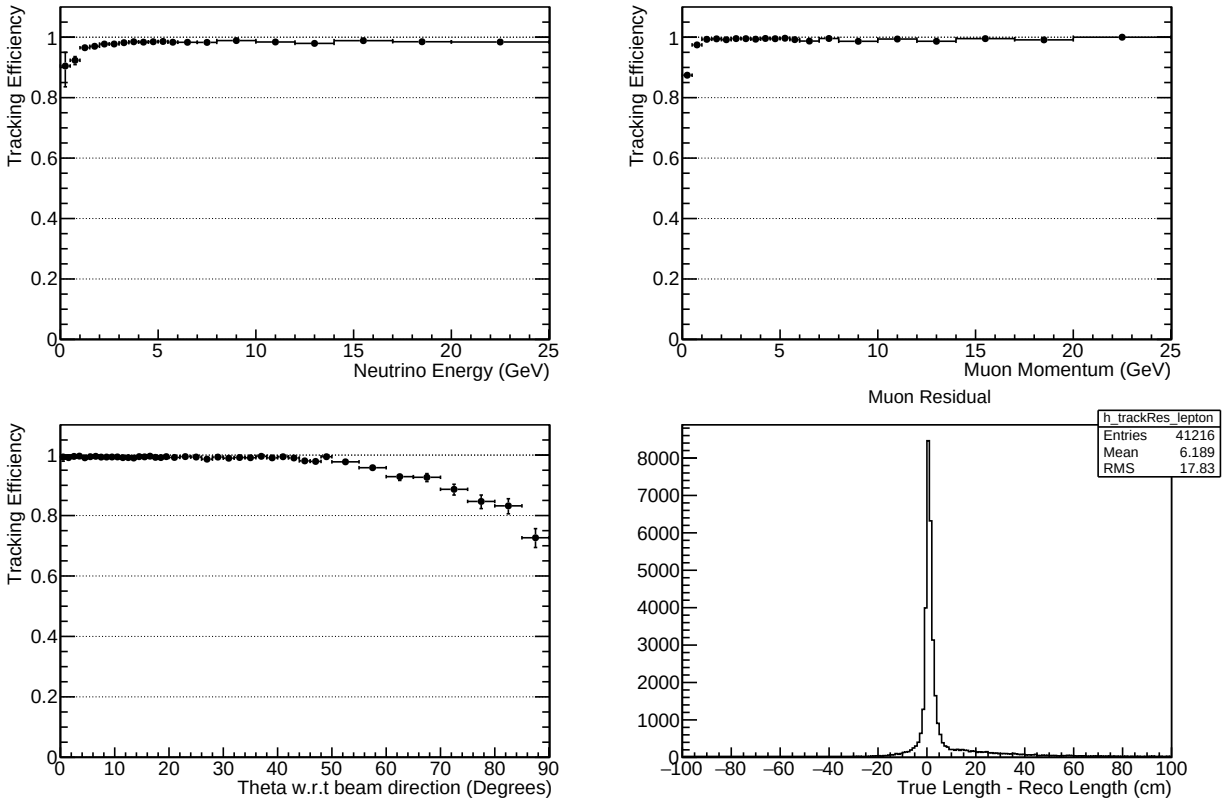

Figure 36: Tracking Efficiency for μ^- produced in a CC ν_μ interaction in LAr. (top left) as a function of incoming neutrino energy. (top right) as a function of muon momentum, (bottom left) as a function of the muon angle w.r.t. the incoming neutrino. (bottom right) track length residual

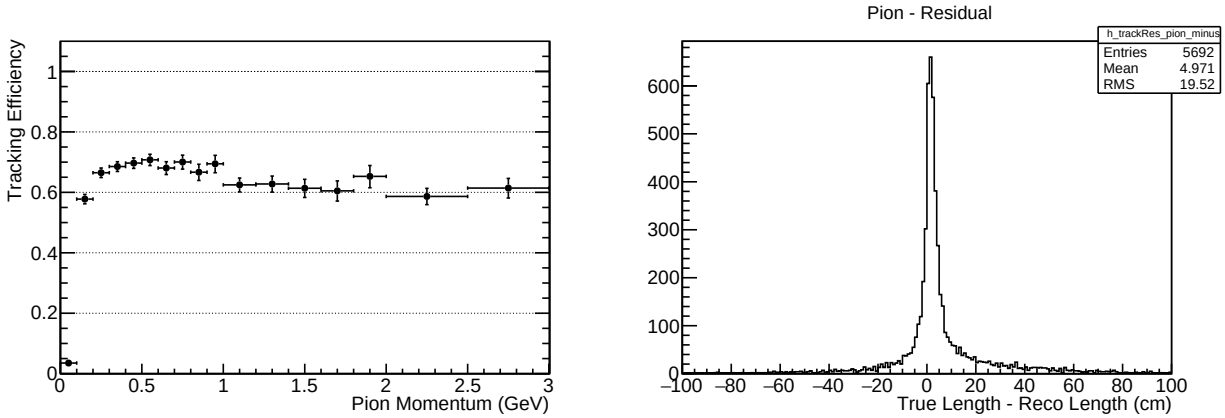

Figure 37: Tracking Efficiency of the leading π^- produced in a CC ν_μ interaction in LAr. (left) as a function of pion momentum, (right) track length residual

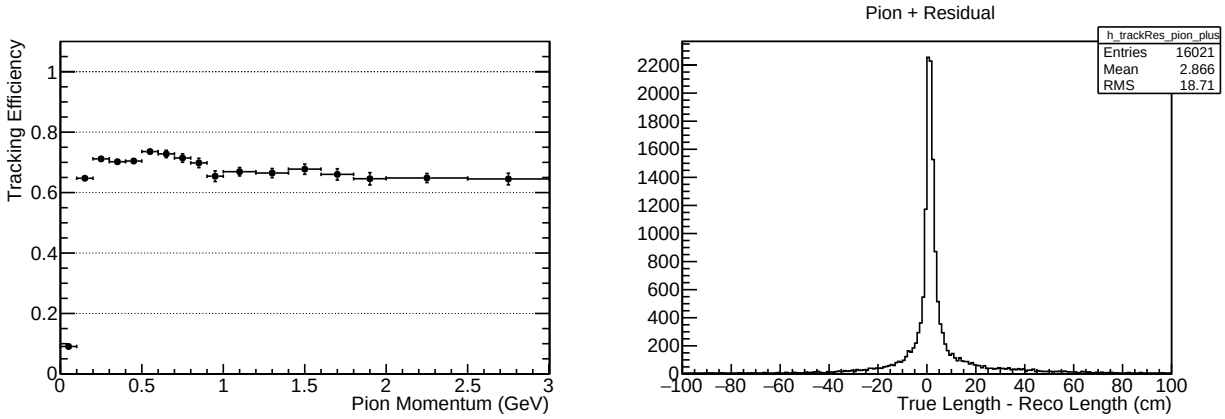

Figure 38: Tracking Efficiency of the leading π^+ produced in a CC ν_μ interaction in LAr. (left) as a function of pion momentum, (right) track length residual

the tracks for low momentum particles before they undergo a hadronic interaction.

Next we present tracking efficiency using various detector configurations with different wire spacing, wire angles and TPC orientations. What we call $Default$ geometry implies 5 mm wire pitch and 36 degree wire angle, $3mm$ is 3 mm wire pitch, $45Deg$ is 45 degree wire angle, and $r90$ Deg beam is a 90 degree rotation of the beam along the z-axis, mimicking a TPC rotation.

Results from the different geometries with different wire pitch and different angle are pretty similar. This can be understood because trajectory fits (tracks) use many data points, over much larger scales than wire pitch. For the case of r90Deg beam the drop in efficiency is due to low hit finding efficiency in this direction. A summary of tracking efficiencies can be found in Table 4. Figure 40 shows tracking efficiencies for the different geometries for μ^-, π^-, π^+ and p as a function of the true length. From the plots there is a 2.5 cm threshold for a 3D track reconstruction regardless of the particle. Overall, the $3mm$ configuration gives

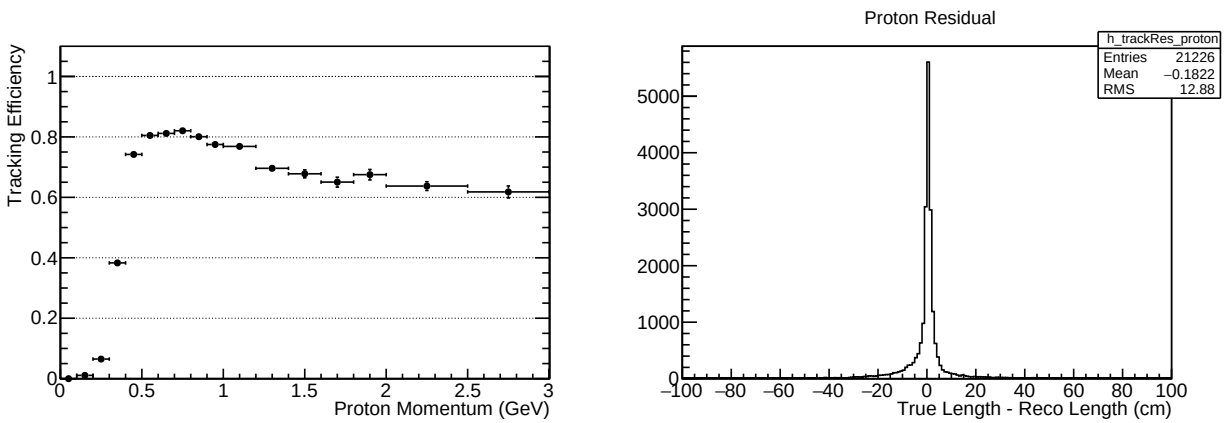

Figure 39: Tracking Efficiency of the leading p produced in a CC ν_μ interaction in LAr. (left) as a function of proton momentum, (right) track length residual

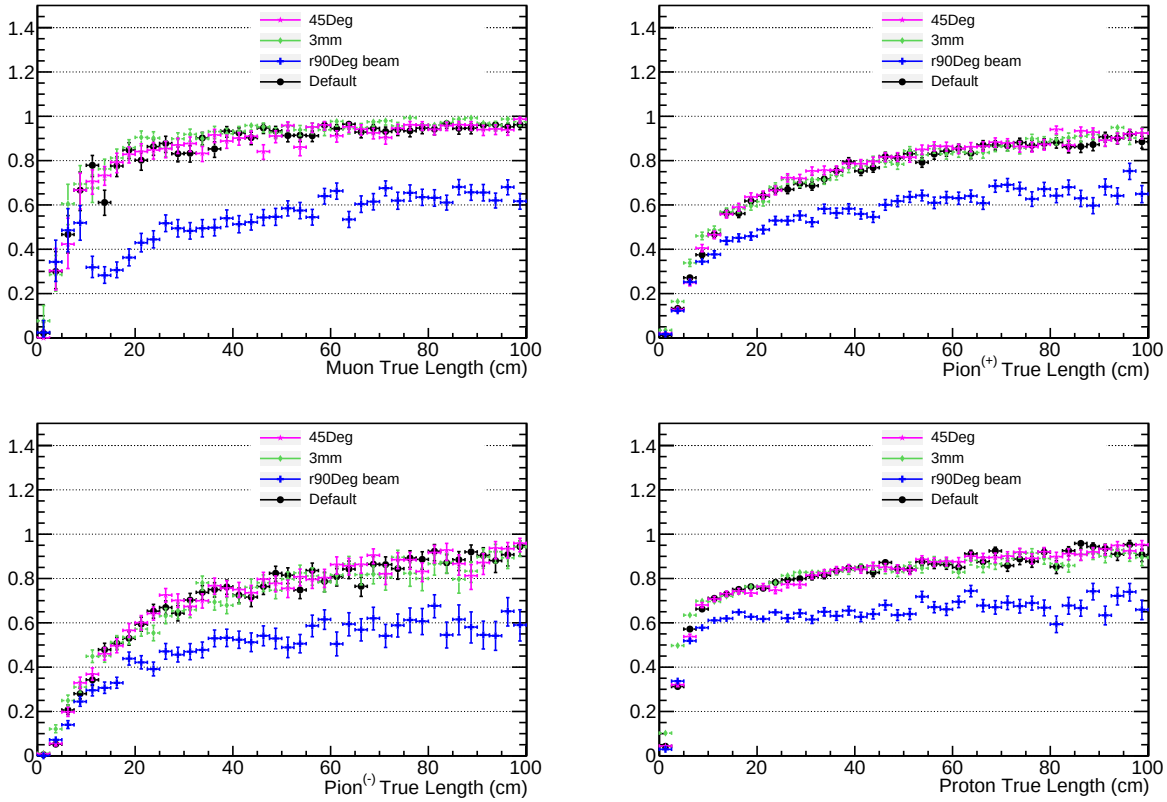

Figure 40: Tracking efficiency for μ^- and leading π^+, π^- and p produced in a CC ν_μ interaction in LAr as a true length.

the better results.

An important topic in DUNE's physics program is the search for proton decay. The

Table 4: Tracking Efficiencies for CC ν_μ events (statistical error only)

	Default (%)	3mm (%)	45Deg (%)	r90Deg beam (%)
Muon	98.2 ± 0.06	98.7 ± 0.06	98.0 ± 0.07	72.2 ± 0.21
Proton	61.0 ± 0.26	64.0 ± 0.26	60.8 ± 0.26	49.5 ± 0.26
Pion$^+$	65.8 ± 0.30	67.8 ± 0.31	67.5 ± 0.30	50.1 ± 0.31
Pion$^-$	61.8 ± 0.50	62.0 ± 0.52	62.2 ± 0.51	42.6 ± 0.51

detection of proton decay would represent experimental evidence for GUTs. With the world's largest particle detector deep underground, DUNE is the ideal detector to search for such a process. Here we present tracking studies of the so called "golden channel" $p \to K^+ + \bar{\nu}$. Thanks to the TPC design it's possible to reconstruct the products of the kaon decay, in specific for the mode $K^+ \to \mu^+ + \nu_\mu$ and also the muon decay $\mu^+ \to e^+ + \nu_e + \bar{\nu}_\mu$. Overall the tracking efficiency for kaons is 60.0%, and 68.3% for muon coming from the kaon decay and 63.1% for Michel electrons coming from the muon decay. Figure 41 shows a fully reconstructed proton decay event.

Another study was performed by looking at different detector configurations where two different reconstructions were applied: TrajCluster and LineCluster. We look at the results as efficiencies for K^+, μ^+, e^+. Overall there is an increase on the efficiency of 2% when using TrajCluster for K^+ and μ^+, and a 9.0% increase on the efficiency for the Michel electron e^+. In summary by using TrajCluster we can lower the threshold for 3D tracks to below 2.5 cm specifically for Michel electrons. Figure 42 shows the tracking efficiency for K^+, μ^+ and Michel electrons as a function of true length for the different detector configurations.

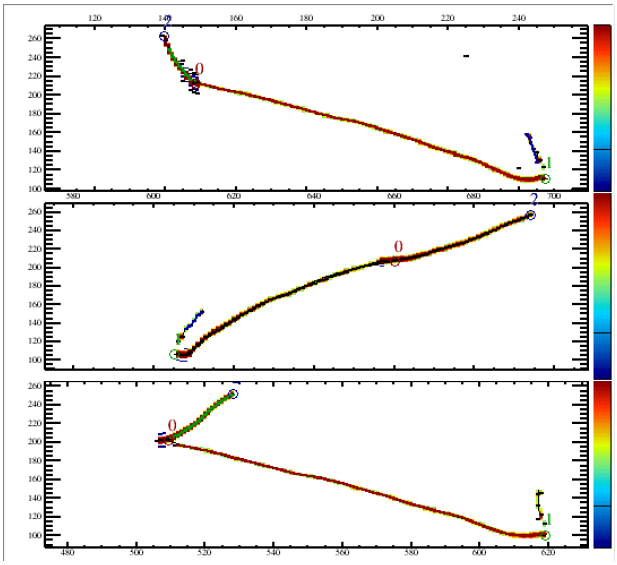

Figure 41: Event display for $p \to K^+ + \bar{\nu}$ event in LAr (collection, induction1 and induction2 planes).

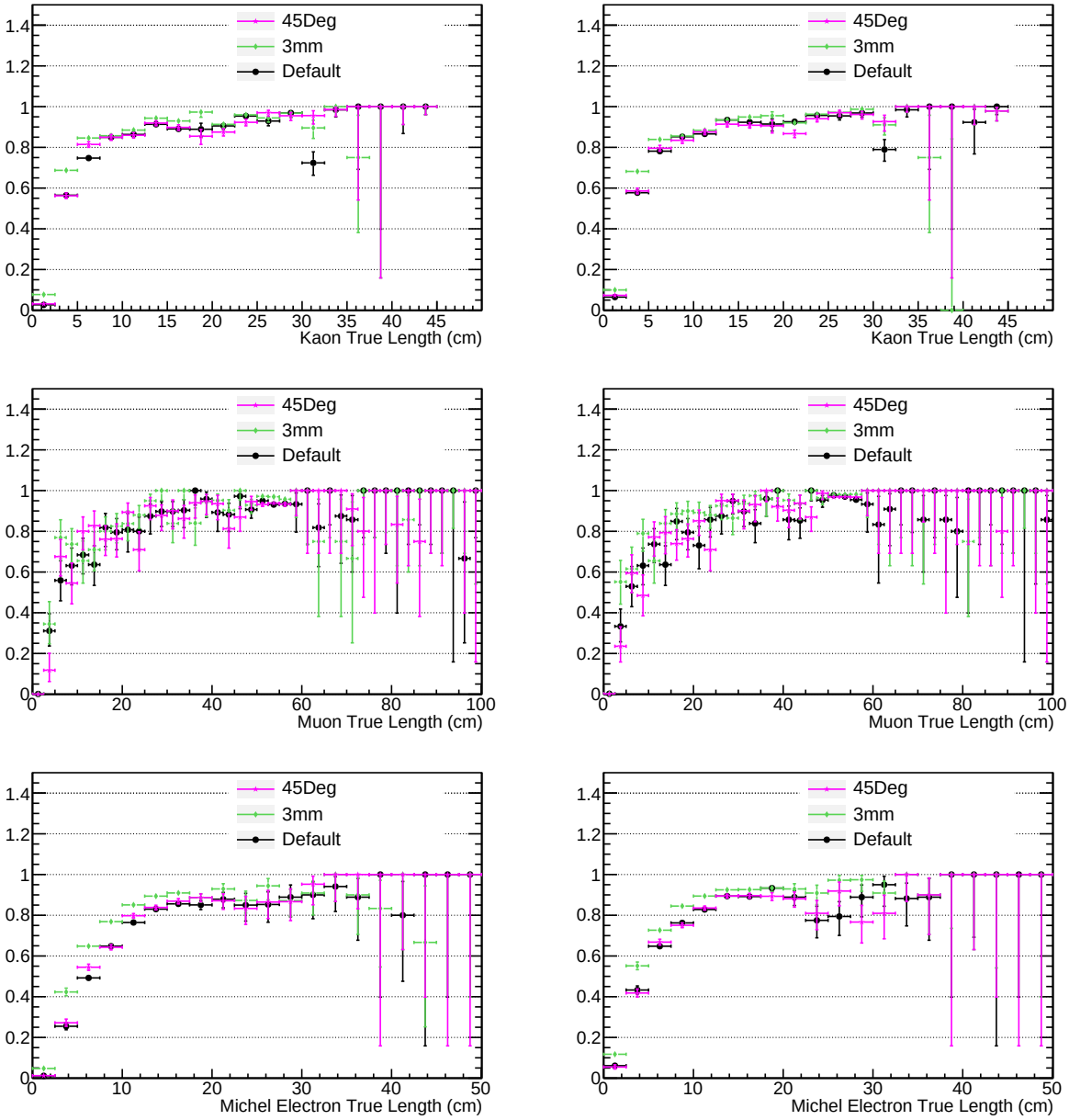

Figure 42: Tracking efficiency K^+, μ^+ and Michel electron (left is with LineClusters, right TrajCluster).

6.1.2 e/γ Separation

Neutrino oscillation analysis is based on the identification of the incident neutrino flavor and estimation of neutrino energy. Electron neutrino charged current (ν_eCC) interactions are to be found among charged and neutral current interactions of other flavors of neutrinos in the far detector data. Several features of the reconstructed events may be used as signatures of ν_eCC. In this chapter we describe potential of reconstruction of two such features which are

expected to be strongly discriminating between ν_eCC (signal) events and background events, namely the ionization density in the initial part of the electron candidate cascade (dE/dx) and detection of the displacement between the starting point of the electron candidate cascade and neutrino interaction vertex (gap). These two features should allow us to distinguish the single electron appearing in the ν_eCC interaction (single m.i.p. dE/dx, no gap detected) from gamma conversion induced cascades (double m.i.p. dE/dx, possible detection of the gap) originating from the decays of π^0's appearing in CC and NC interactions of neutrinos of any flavor. The gap and dE/dx may be reconstructed with different efficiency in various combinations of the detector design parameters. In this section we do not discuss ν_eCC selection inefficiency related to physics, e.g. energy dependent fraction of photons undergoing Compton scattering (thus producing single electron signal-like cascades).

Full event automatic reconstruction is under development. Most components of track reconstruction and particle hierarchy are in place but complete and efficient electromagnetic shower (EM shower) reconstruction and detailed pattern recognition of vertex region are still being developed. Therefore we used the combination of simulation and reconstruction to test potential combinations of detector parameters.

There are five pieces of reconstruction required for ν_e selection and related DUNE physics:

- Recognition of a shower-like object pointing to the neutrino interaction vertex.
- Identification of a visible starting point of the shower (point where the cascade starts to be separated from other tracks near the vertex region).
- Cascade direction reconstruction.
- Electron / photon identification.
- Shower energy reconstruction.

Fiducial volume cuts and corrections for non-containment which are required for the energy measurement have not been studied.

Pattern recognition may handle under some conditions showers which cross dead spaces. The minimum reasonable requirement to identify a shower is to have the initial track-like part and the showering part being visible within the same TPC volume. The radiation length of 14 cm is in the agreement with the observation of about 20 cm along the shower axis that is needed for good reconstruction results. Taking into account the distribution of the angle between the electron and neutrino direction (less than 10% of events above 40 degrees and practically no events above 60 degrees) the first guess for the reasonable fiducial volume cut is about 10-15 cm on lateral walls. If the cathode thickness is small (less than 1 cm), one can consider no cut on the cathode side to be required by the pattern recognition. On the other hand, any field distortions due to supporting structures may result in a significant cut.

Several tracks and showers may overlap in 2D projections near the vertex of neutrino events. The shower part useful for the reconstruction (hits of the shower separated from other tracks) can be displaced from the vertex according to the distributions shown in Figure 43. Significant hints from MC truth were used in order to show in the plot the expected upper limit of the reconstruction precision.

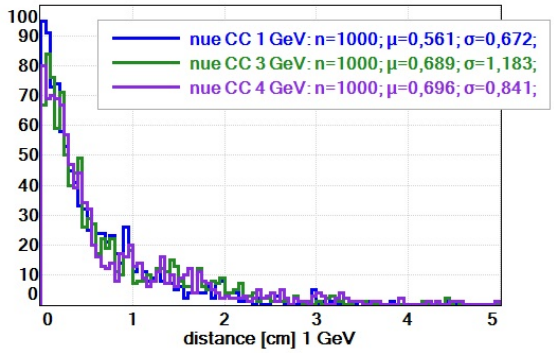

Figure 43: Distance of the visible shower starting point from neutrino interaction vertex. MC truth information (neutrino vertex position and electron direction) is used to select 2D clusters which are used to reconstruct 3D shower direction in order to approximate best possible reconstruction result (3mm wire pitch was used here).

The present method can select as long of an initial section of the shower as useful for the direction reconstruction. The selected part consists of a clean electron (pair) track and the showering part that is not yet strongly developed in the transverse directions. Requirements for this technique are similar to the identification of the shower-like object: length comparable to the radiation length is preferable, although even 2 cm sections are useful in the direction reconstruction in case of early developing showers.

Current pattern recognition algorithms are not precise enough in selection of electron candidate cascades in neutrino event topologies expected for DUNE. Especially problematic is the assignment of hits to particles near the primary vertex. The optimization study needs to evaluate the electron/gamma selection performance that is potentially possible to achieve, regardless of the present state-of-the-art in pattern recognition.

Wire pitch may have an impact on the particle identification which is based on the dE/dx calculation on small scale distances. On the contrary, particle trajectory and vertex reconstruction are based on features much larger than wire pitch and are not sensitive to the difference between wire pitch options. Wire angle between different planes can have some impact on particle identification since the plane selected for the calculations may be chosen from a more or less wide range of available orientations.

These parameters were assumed in the simulation: 3 ms electron lifetime, longitudinal and transverse diffusion, simplified E-field impulse response (signal induced on the single wire) and relatively high S/N. Both low S/N ratio and low electron lifetime affect efficiency of zero suppression, deconvolution and hit finding algorithms. All of them affect the full reconstruction chain and particle identification efficiencies.

Capabilities of pattern recognition algorithms at the present stage are not sufficient to select EM showers in the crowded region of the neutrino vertex. Reconstruction tests using full neutrino events are not yet sensitive to the difference in the detector parameters. For this reason studies were performed in the following conditions:

- Single, isolated electrons and photons were simulated with the uniform distribution in

the far detector workspace geometry, with the flat energy distribution [0.1, 5] GeV.

- Wire signal deconvolution and hit reconstruction were applied as in the standard reconstruction chain.
- Plane with the longest projection of the reconstructed initial segment of the cascade was used for dE/dx calculations.
- dE/dx along the reconstructed direction of cascade was calculated using PMA (PMAlgTrackMaker module).
- Effect of hadron tracks overlapping with the cascade in the vertex region was simulated by removing hits up to some range from the starting point according to Figure 43 and by smearing the calculated distance of hits to the starting point in photon cascades, also according to Figure 43.

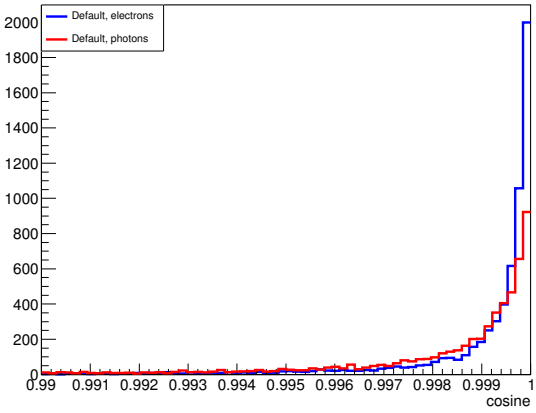

Figure 44: Reconstruction of cascade's initial direction for electrons and photons in the default configuration.

The above conditions allow us to mimic the real complexity of the vertex region and separate inefficiencies due to t the current pattern recognition status. Direction reconstruction is limited by the properties of EM showers (effects of scattering and showering of electrons, two tracks from the vertex in case of photon conversion) and orientation of the shower with respect to the readout planes. Figure 44 shows the angle of reconstructed direction with respect to the truth value. As expected resolution is worse for photons which convert to e+e- pairs. However different wire pitch/orientation configurations do not affect reconstruction as shown on Figure 45.

Studies of shower direction reconstruction show also that the upper limit of the angular resolution is about 6 degrees on average for the presented sample, mainly due to large scattering of low energy electrons and showering in higher energies. At the present stage of shower direction reconstruction the above limit is achievable at the minimal angle of 10 degrees with respect to the wire planes.

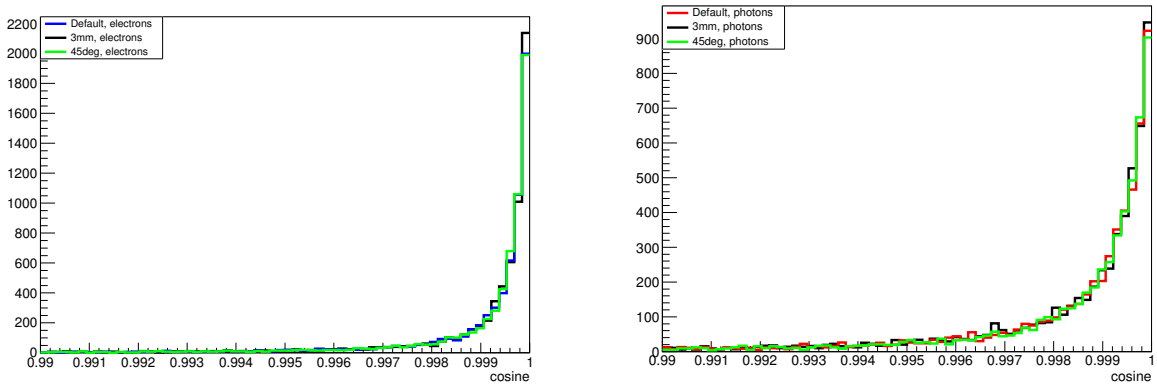

Figure 45: Reconstruction of the cascade's initial direction for electrons (left) and photons (right) for three detector configuration options.

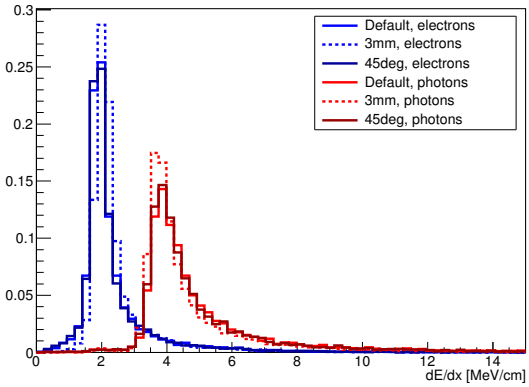

Figure 46: Averaged dE/dx from the initial part of cascade for electrons and photons, calculated for different wire configurations.

The classic method of discrimination between electron and photon induced cascades is based on dE/dx averaged over the initial, track-like section of the cascade. In the presented studies the length of the initial section was optimized to obtain best separation of simulated cascades. In addition we have found that electron selection efficiency of the method can be increased if the first part separated from other tracks in the vertex is used instead of a part up to a fixed distance from the vertex (events overlapped at a longer distances from the neutrino interaction are not lost). The best separation was obtained for a short (1.2-1.5 cm) length for the cascade section. Figure 46 shows distribution of dE/dx for various wire pitch/orientations.

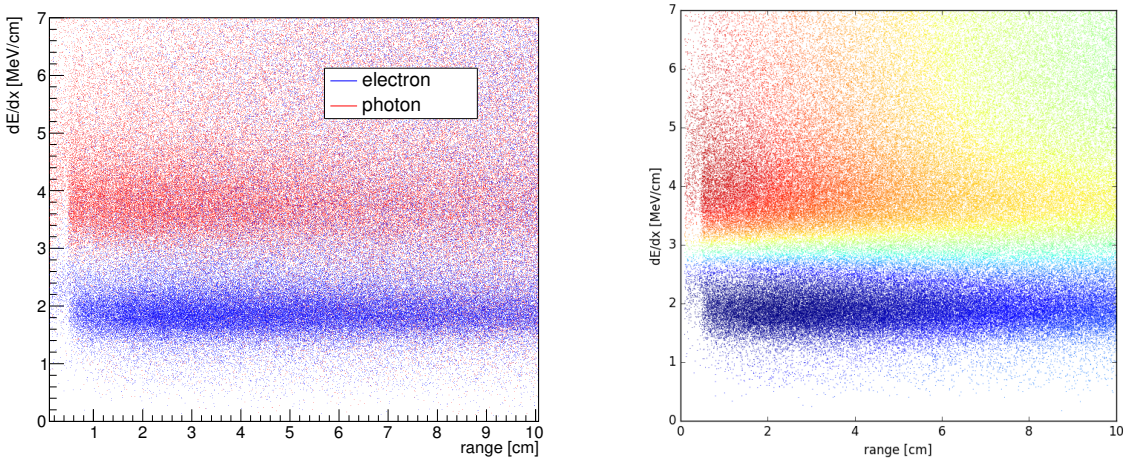

Figure 47: Left: dE/dx as a function of range for electrons (blue) and photons (red). Right: color shows the probability fit that given (range; dE/dx) point belongs to electron cascade; final probability value that a cascade is due to electron or photon conversion is calculated as a product of probabilities of (range; dE/dx) points selected in the initial section of cascade.

An alternative method for electron and photon discrimination was proposed. It allows us to exploit in more detail the statistical differences in dE/dx evolution as a function of the range from the vertex, and dE/dx fluctuations (short increase of ionization due to delta rays) are handled better. The probability that a given shower is initiated by electron or photon is computed instead of using the average dE/dx as a discriminating value; illustration for the default configuration is shown in Figure 47. Electron and photon dE/dx profile patterns were prepared for the range up to about 15 cm from the primary vertex. Similarly to the previous approach, dE/dx points in the first section separated from other tracks in the event are used (usually 2, 3 hits). A probability that the data point belongs to gamma, electron or to "none" class is computed for each point. Finally, probabilities calculated for all points are accumulated and form the discriminating value. The final signal selection efficiency plot as a function of background rejection is shown in Figure 48. For an example value of 90% electron selection efficiency, background reduction by a factor of 25% can be obtained for the 3 mm wire pitch or 45 degree wire orientation options.

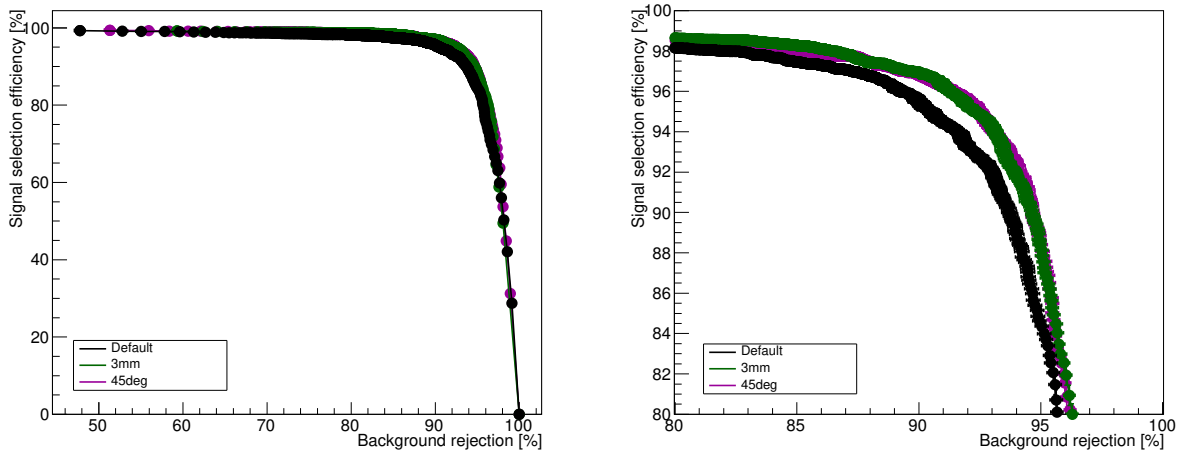

Figure 48: Electron (signal) selection efficiency as a function of photon (background) rejection for three detector configurations. Right plot shows enlarged region from the left plot to show differences in signal efficiency in the interesting range of signal selection and background rejection.

6.2 Perpendicular vs. Parallel APA Comparison

LArTPC is a new detector technology under rapid development for neutrino physics. The present challenges include i) high voltage, ii) high argon purity, iii) low electronic noise, iv) negligible "dead" channels, v) proper TPC signal processing, and vi) event reconstruction. Once the challenges regarding the instrumentation performance, quality control, and integration are overcome, LArTPC event reconstruction is likely to be one of the main remaining bottlenecks to extract physics for experiments. Therefore, it is crucial to examine hardware options which can reduce the challenges in LArTPC event reconstruction. Out of many potential detector parameters to optimize, the orientation of electric field of the TPC with respect to the neutrino beam is the most important one. We note that the drift electric field of the TPC defines the symmetry axis of the device. For isotropic events such as proton decay or astrophysical neutrinos the orientation of this axis with respect to the events cannot be specified. But for accelerator beam events, this choice has to be justified on the basis of the most important requirements of event reconstruction, vertex, and energy resolution. The TPC electric field can be either parallel (APA perpendicular) or perpendicular (APA parallel) to the beam. All other orientations are perturbations on these two fundamental choices. A technote [80] has been prepared to systematically analyze this problem based on the tools available. In this brief note, we summarize the most important observations from this study.

Table 5 summarizes the comparison of the two detector orientations. It should be recalled that there are several detailed requirements on the detector performance for beam neutrino physics. It is required that most (>80%) of the charged current electron neutrino events be reconstructed with excellent energy resolution. The reconstruction must identify the vertex of the events with $\sim$ 1 cm resolution in all dimensions. The neutral current background

to charged current electron neutrino events is to be suppressed using gap and dE/dx (e/γ separation) cuts so that the contamination is $<$ few %.

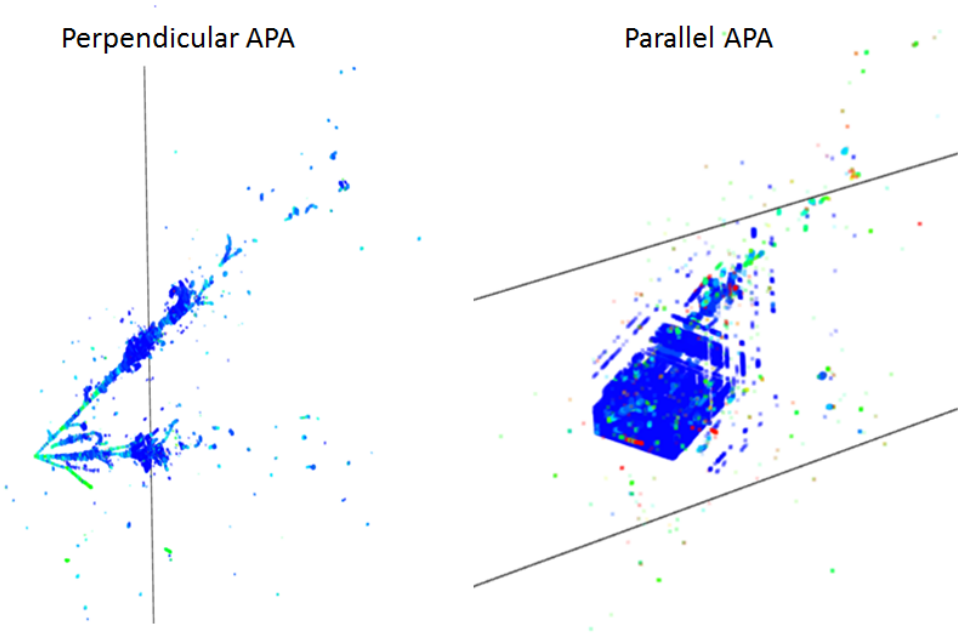

Figure 49: 3D images are reconstructed for a simulated 3-GeV ν_e charge-current interaction. The left (right) panel shows the reconstructed 3D images with the perpendicular (parallel) TPC configuration.

As shown in Fig. 49, the main advantage of a perpendicular APA design is in the event reconstruction, which would result in a higher signal selection efficiency, lower background contamination, and better angular resolution. The angular resolution is crucial for some particular event topologies, such as quasi-elastic scattering and neutrino-electron elastic scattering. We have performed studies based on fast Monte Carlo augmented with appropriate detector geometry simulations. We focus initially on the topology in which particles tracks are near parallel to the wire planes (APA) near the vertex. Such tracks cannot be reconstructed in 3D a priori because the signals from entire trajectory are at the same time due to the finite longitudinal (time) resolution. For the APA parallel geometry: we find that a large fraction ($\sim$ 30%) of the charged current events will have the lepton in the parallel configuration when the APA are parallel to the beam. These events are likely to have poor angular and energy resolutions depending on the characteristics of the events (quasi-elastics, resonance, DIS, etc.). Similar number of events will have hadronic particles or photons parallel to the APA. Furthermore, we calculate that $\sim$ 10% of the entire charged current sample will have overlaps of leptonic and hadronic particles in the parallel plane, which is likely the most difficult to be reconstructed and correctly identified. We also find that the number of neutral current π^0 background events with overlapping hadrons and converting electrons in the parallel plane is high, about 10% compared with the entire charge current signal sample. There is an additional $\sim$ 20% background where a charged pion overlaps with a π^0-decay gamma which converts to an electron further away from the vertex in the parallel plane.

Such a background could mimic a ν_e signal with a similar dE/dx distribution. The effect of these topologies on vertex, energy, and particle identification is under further evaluation. We find that these problematic topologies are considerably reduced in the APA perpendicular geometry.

Furthermore, as shown in Table. 6, the position resolution along the drift field direction (longitudinal) is better than the transverse directions parallel to the wire plane. Therefore, a better $e^{\pm}/\gamma$ separation is expected for the perpendicular APA design, which can reduce the background level. In addition, a 30% cost reduction on the electronics is expected as listed in Table. 5.

The main disadvantage of the perpendicular APA orientation is the reduction of the signal to noise ratio in the induction plane. It has been shown that this should not be a problem if the expected noise level on the cold electronics are achieved on DUNE. However, perpendicular APA orientation will suffer more if there is a sizable increase on the noise level due to excess noise. Therefore, it is important to demonstrate the expected noise level can be achieved in the future prototype detectors. [7]

Table 5: Summary of advantages and disadvantages of perpendicular APA design with respect to the default parallel APA design. The text in blue represents the major advantages. The text in red represents the main disadvantages. The text in black is expected to have negligible impacts on the physics.

	Pros	Cons
Pattern recognition	More information in imaging. [8] Better e/γ separation.	Busy regions due to wrapped wire. [9]
Charge response	Less variations in the induction field response.	Loss in induction charge resolution. [10]
Position resolution	Better angular resolution for long tracks. Less sensitive to the actual wire location.	Worse angular resolution for non-parallel short tracks. [11]
Energy resolution	Better dE/dx calculation for quenching correction. [12]	Energy resolution due to APA gaps. [13] Less capabilities in momentum determination from multiple scattering. [14]
Other considerations	Save $\sim$ 30% Channels. [15] Electronics design specification is suitable.	

[7] LARIAT has demonstrated that the expected noise level can be achieved. MicroBooNE has demonstrated that the expected noise level can be achieved after a software noise filter [81]. Hardware upgrades are on-going to achieve the expected noise level before software noise filter. More unique features in DUNE, such as the mixed analog-digital front-end and the modular design, will be tested in the protoDUNE detector.

[8] The improvements in the pattern recognition leads to improvement in almost all aspects of the later event reconstruction chain including energy and angular calculation.

Table 6: Comparison of the resolution between the longitudinal and transverse directions for LArTPC operating at 500 V/cm electric field. The resolution in the longitudinal dimension is expected to be much better than that of the transverse dimension due to better resolution and finer digitization.

Property	Longitudinal Dimension	Transverse Dimension
Digitization length	0.8 mm	5 mm [16]
Diffusion σ [17]	< 1.7 mm	< 2.4 mm
Electronics shaping σ	1.3 mm [18]	N/A
Field response function σ	$\sim$1.1 mm	5 mm [19]
Overall resolution	< 2.5 mm	> 5 mm

6.3 Considerations of implementing an additional readout wire plane in the single-phase LArTPC

In this section, we summarize the considerations of implementing an additional induction wire plane in the single-phase LArTPC to enhance its performance.

In the current design of the DUNE single-phase LArTPC, there are three readout wire planes. In front of these readout planes, there is a grid wire plane added in order to shape the impulse field response function. On the back of these readout planes, there is a wire plane to prevent the collection of ionization charge generated inside the anode plane assembly (APA). Bias voltage is applied on these (five) wire planes, so that the ionization electrons will drift at 100% transparency through the grid plane and first two readout wire planes before all collecting on the last readout plane. The first two readout wire planes are commonly referred to as the induction plane and the last readout wire plane is referred to as the collection plane. The impulse field response function has a bipolar and unipolar shape for the induction and collection planes, respectively.

There are three reasons that adding one more induction wire plane will significantly increase the performance of the single-phase LArTPC. They are:

- Ambiguities reduction,

[9]The proposal of the single-sided APA will completely solve this issue.

[10]At expected electronics level of DUNE, the impact of increment in the charge resolution from induction wire plane on the induction plane hit selection efficiency is small for the ν_e signal. Nevertheless, if there is a sizable increase of the electronic noise, perpendicular APA configuration will suffer more.

[11]For 1 GeV/c muon, the short track is defined as the traveling length shorter than 20 cm.

[12]The improvement of dE/dx is coming from improvement of the position resolution as well as pattern recognition.

[13]The leading contributor is shown to be neutrons generated in the neutrino and subsequent hadronic interactions.

[14]Due to the vast size of DUNE detector, the impact of this loss of capability on ν_μ charge-current interaction is expected to be small.

[15]There is a 3% reduction on the fiducial volume, which is changed to +0.9% gain with 3.8 meter drift distance.

[16]This length is basically the wire pitch.

[17]Maximum drift distance is assumed to be 3.6 m.

[18]The shaping time is assumed to be 2 μs.

[19]The resolution due to induction is expected to be comparable to the wire pitch.

- More resistance to dead channels,
- Increase the acceptance for the induction signal through robust ROI finding.

In the following, we will briefly describe each reason.

In single-phase LArTPC, the 1D wire-based readout is necessary due to the financial constraint on the total number of channels that can be afforded and the physical constraint on the total electronics consumption power that can be allowed in the LAr. Compared to the 2D pad-based readout, the (multiple) 1D wire-based readout significantly reduces the total number of channels at the cost of increases in ambiguities. Figure 50 shows the number of reconstructed potential hits as a function of the number of real hits in a fixed time slice. A reconstructed potential hit is defined as a hit where multiple hit wires (one from each readout plane) cross. These wires may not be necessarily originated from the same real hit. Therefore the number of reconstructed potential hits is larger than the number of real hits. The different colored solid curves represent different number of total readout wire planes from 2 to 6. It is clear that more wire planes would reduce the ambiguities. For DUNE (3 wire plane case), the number of potential hits roughly ranges from one to fifty for ν_e charged-current interactions. Therefore, increasing the number of readout wire planes from three to four represents a significant step towards reducing the ambiguities, which is crucial for clearly identifying activity near the neutrino interaction vertex (one of the busiest regions).

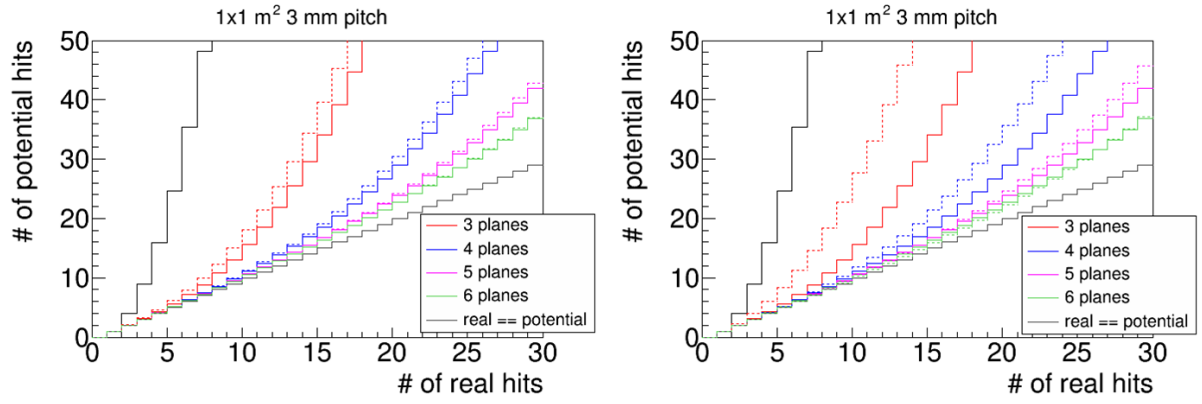

Figure 50: Illustration of ambiguities with the number of reconstructed potential hits as a function of the number of real hits in a 1D wire-based readout detector. Different colored curves represent different number of wire planes from 2 (black) to 6. The no-ambiguity situation where the number of reconstructed potential hits is exactly the same as the number of real hits is labeled as "real == potential". The solid curves represent the situation when all the channels are functioning. The dashed curves represent the situation where some of the channels are dead. The left (right) panel represents the situation where 1% (5%) of the channels are dead. See the text for more discussion.

In practice, it is unrealistic to have 100% working channels for a 10kt detector. For example, in the current-generation large LArTPC experiments, the ratio between the number of dead channels and the number of total channels is above 10%. In the next-generation large LArTPCs, we expect this ratio to be significantly reduced. Nevertheless, it is unrealistic to

assume zero dead channels. Assuming "p" is the efficiency of a single wire plane, the volume efficiency can thus be estimated as $\epsilon_n = p^n$ given "n" number of wire planes. This volume efficiency can be enhanced if fewer planes are required in the reconstruction. For example, if we require one less readout plane to be used in the reconstruction, the volume efficiency is $\epsilon_{n-1} = p^n + n \cdot (1-p) \cdot p^{n-1}$, which can be much higher than ϵ_n. However, the increase in the volume efficiency is at the cost of increasing the number of ambiguities. Assuming F_n represents the number of reconstructed potential hits given "n" number of wire planes, the number of reconstructed potential hits using one less plane in the reconstruction can be estimated as $(F_n + (1-p) \cdot n \cdot (F_{n-1} - F_n)) \cdot \epsilon_{n-1}$. Basically, when one less readout wire plane is required in the reconstruction, the number of reconstructed potential hits F_n will receive a leakage from that of the "n-1" wire plane F_{n-1}. The left (right) panel of Fig. 50 illustrates the situation for 1% (5%) dead channels. Since the ambiguity with three wire planes is much reduced compared to that of the two wire planes, the four wire planes are much more robust against the potential dead channels compared to the three wire planes case.

Besides the existence of ambiguity due to the 1D wire-based readout, another big challenge of the single-phase LArTPC is the processing of the induction wire plane signal. When the impulse field response of the collection wire plane is unipolar, the impulse field response of the induction wire plane is bipolar. The integration of the induction impulse response function over time is close to zero, as none of the ionization electron is collected by the induction plane. Depending on the original ionization electron distribution, the positive lobe of field response could cancel with the negative lobe leading to overall smaller signal heights compared to those from collection wire plane. Therefore, the induction wire plane signal is much more sensitive to noise compared to the collection wire plane signal. The implementation of the cold electronics that significantly reduces the electronic noise as shown in Ref. [81] represents a major step towards improving the induction wire plane signal. Furthermore, the implementation of the 2D deconvolution in the signal processing chain [82] represents another significant step in improving the induction wire plane signal. Despite these efforts, there is still a limitation in the induction plane signal, as the signal to noise ratio becomes smaller with the increase of the signal (time) length. In order to maximize the signal to noise ratio in the induction plane, the region-of-interest (ROI) technique is crucial. A ROI is a region that just contains the signal, so that the electronic noise, especially the low-frequency one, is minimized during the signal processing. In practice, while finding the ROI is a relative simple task for a short signal, it is much more difficult to reliably find the ROI for a long signal due to the smaller signal to noise ratio. Adding a new readout wire plane can significantly improve the ROI finding. Recall that a real ionization signal would generate currents on each wire plane simultaneously [20]. Therefore, a long ROI can be built from short ROIs from the other wire planes requiring the wires from different planes crossing at the same point. This technique works for tracks that are not traveling completely perpendicular to a wire plane. In principle, this technique can work for the sitution of three readout wire planes. In this case, the ROI has to be built from the other two wire planes. However, as shown in Fig. 50, the number of ambiguities for three wire planes is much reduced than that of two wire planes. Therefore, the aforementioned robust ROI finding technique is much less

[20] The coincidence is after taking into account the short time needed for ionization electrons traveling from one wire plane to the next.

powerful in the three readout wire planes case. Adding one more induction wire plane can significantly improve the situation.

Technically, in the current single-phase APA design, the grid plane, which is at the correct bias voltage, can be converted into the fourth induction wire plane once it is read out. Ref. [82] shows that the signal processing of the first induction wire plane in MicroBooNE (without a grid plane) is successful. Therefore, the original requirement of shaping the induction impulse field response with a grid plane can be relaxed. The angle of the grid plane wire will need to be changed so that there is no degeneracy in the wire orientation among all readout planes.

Based on these studies, we also emphasize it is important to consider three or more readout planes for the dual-phase LArTPC design. Although the dual-phase design is free of the complication from induction wire planes, the considerations of reducing ambiguities due to 1D wire-based readout still apply.

6.4 Photon Detector System Task Force

The photon detector system task force was formed in August 2016 to address two questions: do the existing photon detector (PD) requirements meet the DUNE physics goals, and do improvements to the DUNE physics program warrant the costs of increasing the performance of the PD system? In particular, the charge to the PD task force is defined as determining whether:

1. The existing PDS and TPC requirements are sufficient define a detector capable of performing scientifically relevant measurements that support the DUNE physics program, which for this charge shall be defined as both the beam physics program and non-beam physics associated with proton decay, atmospheric neutrinos, and SNB events.

2. The existing light detection response parameter of 0.1 photoelectron-per-MeV of energy deposition is sufficient to support the DUNE physics program, and how rapidly scientific benefits would increase as this light yield is increased.

3. Addition of specific mean detection efficiency requirements for various minimum visible energy depositions would significantly enhance the DUNE physics program.

4. Addition of specific uniformity of detection efficiency requirements for various minimum visible energy depositions would significantly enhance the DUNE physics program.

The highest level (L2) Requirements for the PD system can be found in the LBNF-DUNE requirements document [83].

The PD task force will provide a report addressing these charges by March 2017 in coordination with the full Far Detector Task Force. In order to achieve this goal the PD task force has begun establishing a team that includes membership from the PD working group, as well as the supernova, nucleon decay, and atmospheric neutrino physics groups. Preliminary work by the task force will involve reproducing existing PD-related physics studies using the more sophisticated tools developed by the DUNE collaboration. Following this effort, members of the task force will work to implement enhanced PD performance into

the DUNE far detector simulations in order to gauge the level of physics performance that can be achieved through such improvements.

A PD task force workshop will be held in January in order to assess the progress of the group and to prioritize the task force effort going forward. Table 7 outlines the task force timeline.

Milestone	Target Date
First task force meeting	Sep (2016)
Weekly meeting begin	Oct (2016)
Reproduction of existing studies complete	Nov (2016)
PD Task Force Workshop	Jan (2017)
Finalizing Task Force Report	Mar (2017)
Deliver Task Force Report	Mar (2017)

Table 7: Photon detector task force timeline.

7 Summary and Next Steps

Great progress has been made toward the task force goals in the past year. This section summarizes the accomplishments and next steps for each item in the charge.

FD Simulation and Reconstruction Chain: The full simulation and reconstruction chain is functioning. The simulation and reconstruction working group regularly produces large sets of MC for analysis. Simulation and reconstruction algorithms will continue to be refined, but the infrastructure is in place.

Simulation and Reconstruction for SNB and Nucleon Decay Physics: Generators for supernova neutrinos, atmospheric neutrinos, cosmic muons, and nucleon decay physics have all been successfully incorporated into LArSoft, and samples have been generated using the DUNE geometry. Reconstruction performance is being tested for nucleon decay physics, and reconstruction for low-energy neutrinos is starting to be developed. The next steps will be refining the reconstruction and examining physics performance for different detector geometries.

Long-Baseline Sensitivity Update: Event selection algorithms have been developed using beam MC, and oscillation fitters are being validated. In the near future, the first sensitivities using full simulation and reconstruction will be available. The next steps will be improving the event identification algorithms and reconstruction tools and examining physics performance for different detector geometries.

Dual-Phase TPC: Simulation and reconstruction for the dual-phase design has been incorporated into LArSoft and validated. The next steps will be refining the reconstruction algorithms and doing physics performance studies with the dual-phase geometry.

Detector Optimization Studies: Detector optimization studies have started, by first looking at the effect of wire angle and spacing on tracking efficiency and e/γ separation. The next step will be to see the effect of these choices on the physics sensitivities. The Photon Detection System Task Force, which is a sub-group of the FD Optimization Task Force, has just been formed. They will study the photon detection system requirements with regard to supernova and nucleon decay physics. Other detector designs, such as perpendicular APAs or TPCs with additional wire planes, are also actively being investigated.

References

[1] P. Huber, M. Lindner and W. Winter, Comput. Phys. Commun. **167**, 195 (2005) doi:10.1016/j.cpc.2005.01.003 [hep-ph/0407333].

[2] `http://www.mpi-hd.mpg.de/lin/globes/`

[3] `http://larsoft.org/`

[4] `https://cdcvs.fnal.gov/redmine/projects/larbatch/wiki`

[5] `http://dune-data.fnal.gov/mc/mcc6.0/index.html`

[6] `http://www-pnp.physics.ox.ac.uk/~barr/fluxfiles/0401/index.html`

[7] `http://www.icrr.u-tokyo.ac.jp/~mhonda/nflx2014/index.html`

[8] M. Bhattacharya, A. Garcia, N. I. Kaloskamis, E. G. Adelberger, H. E. Swanson, et al., Phys. Rev. C **58**, 3677 (1998) doi:10.1103/PhysRevC.58.3677.

[9] J. A. Cameron and B. Singh, Nuclear Data Sheets, **V. 102**, I. 2, 293 (2004) doi:10.1016/j.nds.2004.06.001.

[10] `http://www.phy.duke.edu/~schol/snowglobes`

[11] J. Gava, J. Kneller, C. Volpe, G. C. McLaughlin, Phys. Rev. Lett., **103**, 071101 (2009) doi:10.1103/PhysRevLett.103.071101

[12] P. Antonioli, C. Ghetti, E.V. Korolkova, V.A. Kudryavtsev, G. Sartorelli, A Three-dimensional Code for Muon Propagation Through the Rock: MUSIC, Astroparticle Physics, 7:357, 1997.

[13] V. A. Kudryavtsev, Muon Simulation Codes MUSIC and MUSUN for Underground Physics, Computer Physics Communications, 180:339, 2009.

[14] ArgoNeuT Collaboration, "A study of electron recombination using highly ionizing particles in the ArgoNeuT Liquid Argon TPC," JINST **8**, P08005 (2013).

[15] ICARUS Collaboration, "Study of electron recombination in liquid argon with the ICARUS TPC", Nucl. Instrum. Meth. Phys. Res. A 523 (2004), 275.

[16] Yichen Li, "Measurement of Longitudinal Electron Diffusion in Liquid Argon", Nucl. Instrum. Meth. A816, 160 (2016).

[17] Summary of Liquid Argon Properties `http://lar.bnl.gov/properties/`.

[18] R. Veenhof, "GARFIELD, recent developments", Nucl. Instrm. Meth. Phys. Res. A 419 (1998), 726.

[19] Laurence W. Nagel and D. O. Pederson, "SPICE (Simulation Program iwth Integrated Circuit Emphasis)", UCB/ERL M382 (1973).

[20] "A Method to Extract the Charge Distribution Arriving at the TPC Wire Planes in MicroBooNE", MicroBooNE NOTE 1017-PUB.

[21] D. Whittington, S. Mufson, J. Inst., **11(05)**, P05016 (2014) doi:10.1088/1748-0221/11/05/P05016 [arXiv:1408.1763 [physics.ins-det]]

[22] "Noise Characterization and Filtering in the MicroBooNE TPC", MicroBooNE NOTE 1016-PUB.

[23] Bruce Baller, "Liquid Argon TPC Formation, Signal Processing, and Reconstruction", under preparation.

[24] `https://cdcvs.fnal.gov/redmine/documents/727`

[25] `http://larsoft.org/single-record/?pdb=110`

[26] J. S. Marshall and M. A. Thomson, Eur. Phys. J. C **75**, no. 9, 439 (2015) doi:10.1140/epjc/s10052-015-3659-3 [arXiv:1506.05348 [physics.data-an]].

[27] M. Antonello *et al.*, Adv. High Energy Phys. **2013**, 260820 (2013) doi:10.1155/2013/260820 [arXiv:1210.5089 [physics.ins-det]].

[28] `http://larsoft.org/single-record/?pdb=113`

[29] `http://www.phy.bnl.gov/wire-cell/`

[30] R. Acciarri *et al.* [DUNE Collaboration], arXiv:1512.06148 [physics.ins-det].

[31] `http://www.phy.duke.edu/~schol/snowglobes`

[32] S. Amoruso *et al.* [ICARUS Collaboration], Eur. Phys. J. C **33**, 233 (2004) doi:10.1140/epjc/s2004-01597-7 [hep-ex/0311040].

[33] G. Sinev, Talk at LEPP-3, Moscow

[34] G. Sinev, DUNE DocDB-665

[35] Alison J. Roeth, LBNE DocDB-8825

[36] DUNE DocDB-1589

[37] G. Sinev, DUNE DocDB-1181

[38] A. Bueno, Z. Dai, Y. Ge, M. Laffranchi, A. J. Melgarejo, A. Meregaglia, S. Navas and A. Rubbia, JHEP **0704**, 041 (2007) doi:10.1088/1126-6708/2007/04/041 [hep-ph/0701101].

[39] C. Andreopoulos *et al.*, Nucl. Instrum. Meth. A **614**, 87 (2010) doi:10.1016/j.nima.2009.12.009 [arXiv:0905.2517 [hep-ph]].

[40] C. Andreopoulos, C. Barry, S. Dytman, H. Gallagher, T. Golan, R. Hatcher, G. Perdue and J. Yarba, arXiv:1510.05494 [hep-ph].

[41] K. A. Olive *et al.* [Particle Data Group Collaboration], Chin. Phys. C **38**, 090001 (2014). doi:10.1088/1674-1137/38/9/090001

[42] M. Sorel, Expanding GENIE's Nucleon Decay Tools, https://indico.fnal.gov/getFile.py/access?contribId=4&resId=0&materialId=slides&confId=12549

[43] T. Yang, Simulation of Nucleon Decays, https://indico.fnal.gov/getFile.py/access?contribId=5&resId=0&materialId=slides&confId=12549

[44] G. Santucci, Far detector simulation and reconstruction chain for non-beam events, https://indico.fnal.gov/getFile.py/access?contribId=59&sessionId=19&resId=0&materialId=slides&confId=10612

[45] A. Ferrari, P. R. Sala, A. Fasso and J. Ranft, CERN-2005-010, SLAC-R-773, INFN-TC-05-11.

[46] K. Wood, Vertex Assignment Correction in NDK Generation, https://indico.fnal.gov/getFile.py/access?contribId=5&resId=0&materialId=slides&confId=12377

[47] J. Hewes, Neutron-antineutron oscillation in DUNE", https://indico.fnal.gov/getFile.py/access?contribId=58&sessionId=31&resId=0&materialId=slides&confId=10276

[48] A. Higuera, Far detector tracking efficiencies, https://indico.fnal.gov/getFile.py/access?contribId=63&sessionId=19&resId=0&materialId=slides&confId=10612

[49] H. Mendez and N. Martinez, First look at fully reconstructed $p \to l^+\rho^0$ and $p \to \mu^+K^0$ events, https://indico.fnal.gov/getFile.py/access?contribId=3&resId=0&materialId=slides&confId=12549

[50] A. Higuera, Proton decay, $p \to \bar{\nu}K^+$, https://indico.fnal.gov/getFile.py/access?contribId=2&resId=0&materialId=slides&confId=12651

[51] R. Acciarri *et al.* [ArgoNeuT Collaboration], JINST **8**, P08005 (2013) doi:10.1088/1748-0221/8/08/P08005 [arXiv:1306.1712 [physics.ins-det]].

[52] K. Wood, Flash Finding Efficiencies for PDK events, https://indico.fnal.gov/getFile.py/access?contribId=0&resId=0&materialId=slides&confId=12651

[53] M. Goodman and L Lin, Comprehensive list of nucleon decay modes (DUNE-doc-679), http://docs.dunescience.org:8080/cgi-bin/ShowDocument?docid=679

[54] M. Sorel, ndksens, A tool for evaluating NDK sensitivities, https://indico.fnal.gov/getFile.py/access?contribId=57&sessionId=31&resId=0&materialId=slides&confId=10276

[55] G. D. Barr, T. K. Gaisser, P. Lipari, S. Robbins and T. Stanev, Phys. Rev. D **70**, 023006 (2004) doi:10.1103/PhysRevD.70.023006 [astro-ph/0403630].

[56] G. Battistoni, A. Ferrari, P. Lipari, T. Montaruli, P. R. Sala and T. Rancati, Astropart. Phys. **12**, 315 (2000) doi:10.1016/S0927-6505(99)00110-3 [hep-ph/9907408].

[57] M. Sajjad Athar, M. Honda, T. Kajita, K. Kasahara and S. Midorikawa, Phys. Lett. B **718**, 1375 (2013) doi:10.1016/j.physletb.2012.12.016 [arXiv:1210.5154 [hep-ph]].

[58] J. Losecco, Honda atmospheric flux calculation for Homestake, `https://indico.fnal.gov/materialDisplay.py?contribId=3&materialId=slides&confId=11533`

[59] M. Rafi Alam, I. Ruiz Simo, M. Sajjad Athar and M. J. Vicente Vacas, Phys. Rev. D **82**, 033001 (2010) doi:10.1103/PhysRevD.82.033001 [arXiv:1004.5484 [hep-ph]].

[60] M. Alam *et al.*, arXiv:1512.06882 [hep-ph].

[61] A. Ioannisian, Exploring the Earth with neutrinos, `https://indico.fnal.gov/materialDisplay.py?contribId=0&materialId=slides&confId=10573`

[62] L. Fantini and G. VanWinkle, Measuring the azimuthal angle distribution of atmospheric neutrinos in DUNE, `https://indico.fnal.gov/materialDisplay.py?contribId=3&materialId=slides&confId=12005`

[63] E. Richard *et al.* [Super-Kamiokande Collaboration], Phys. Rev. D **94**, no. 5, 052001 (2016) doi:10.1103/PhysRevD.94.052001 [arXiv:1510.08127 [hep-ex]].

[64] H. Gallagher, Atmospheric event generators, `https://indico.fnal.gov/materialDisplay.py?contribId=2&materialId=slides&confId=12274`

[65] V. A. Kudryavtsev, Comput. Phys. Commun. **180**, 339 (2009) doi:10.1016/j.cpc.2008.10.013 [arXiv:0810.4635 [physics.comp-ph]].

[66] V. A. Kudryavtsev, N. J. C. Spooner and J. E. McMillan, Nucl. Instrum. Meth. A **505**, 688 (2003) doi:10.1016/S0168-9002(03)00983-5 [hep-ex/0303007].

[67] P. Antonioli, C. Ghetti, E. V. Korolkova, V. A. Kudryavtsev and G. Sartorelli, Astropart. Phys. **7**, 357 (1997) doi:10.1016/S0927-6505(97)00035-2 [hep-ph/9705408].

[68] V. A. Kudryavtsev, E. V. Korolkova and N. J. C. Spooner, Phys. Lett. B **471**, 251 (1999) doi:10.1016/S0370-2693(99)01378-7 [hep-ph/9911493].

[69] D.-M. Mei, C. Zhang, K. Thomas and F. Gray, Astropart. Phys. **34**, 33 (2010) doi:10.1016/j.astropartphys.2010.04.003 [arXiv:0912.0211 [nucl-ex]].

[70] C. Zhao (USD), private communication

[71] F. E. Gray, C. Ruybal, J. Totushek, D.-M. Mei, K. Thomas and C. Zhang, Nucl. Instrum. Meth. A **638**, 63 (2011) doi:10.1016/j.nima.2011.02.032 [arXiv:1007.1921 [nucl-ex]].

[72] J. Heise, AIP Conf. Proc. **1604**, 331 (2014) doi:10.1063/1.4883449 [arXiv:1401.0861 [physics.ins-det]].

[73] Martin Richardson, Ph.D. Thesis, University of Sheffield, 2016.

[74] M. L. Cherry, M. Deakyne, K. Lande, C. K. Lee, R. I. Steinberg, B. T. Cleveland and E. J. Fenyves, Phys. Rev. D **27**, 1444 (1983). doi:10.1103/PhysRevD.27.1444

[75] N. Abgrall *et al.* [Majorana Collaboration], arXiv:1602.07742 [nucl-ex].

[76] D. Stefan and A. M. Ankowski, Acta Phys. Polon. B **40**, 671 (2009) [arXiv:0811.1892 [nucl-th]].

[77] J. Klinger, V. A. Kudryavtsev, M. Richardson and N. J. C. Spooner, Phys. Lett. B **746**, 44 (2015) doi:10.1016/j.physletb.2015.04.054 [arXiv:1504.06520 [physics.ins-det]].

[78] `https://www.overleaf.com/5565604ftcwxj#/17932618/`

[79] `https://cdcvs.fnal.gov/redmine/projects/larreco/repository/changes/larreco/TrackFinder/NeutrinoTrackingEff_module.cc`

[80] M. Bishai *et al.* "LArTPC: Perpendicular vs. Parallel Detector Optimization", DUNE DocDB-1708.

[81] "Noise Characterization and Filtering in the MicroBooNE TPC", MicroBooNE NOTE 1016-PUB, `http://www-microboone.fnal.gov/publications/publicnotes/MICROBOONE-NOTE-1016-PUB.pdf`.

[82] "A Method to Extract the Charge Distribution Arriving at the TPC Wire Planes in MicroBooNE", MicroBooNE NOTE 1017-PUB, `http://www-microboone.fnal.gov/publications/publicnotes/MICROBOONE-NOTE-1017-PUB.pdf`.

[83] J. Dolph, "LBNF-DUNE Requirements," DUNE DocDB-112-v6.